A DYNAMIC ROD MODEL
TO SIMULATE
MECHANICS OF CABLES AND DNA

by

Sachin Goyal

A dissertation submitted in partial fulfillment
of the requirements for the degree of
Doctor of Philosophy
(Mechanical Engineering and Scientific Computing)
in The University of Michigan
2006

Doctoral Committee:

    Professor Noel Perkins, Chair

    Associate Professor Edgar Meyhofer, Co-Chair

    Assistant Professor Ioan Andricioaei

    Assistant Professor Krishnakumar Garikipati

    Assistant Professor Jens-Christian Meiners

To my parents

Acknowledgements

Table of Contents

List of Figures

List of Tables

List of Appendices

Abstract

This dissertation contributes a computational 'rod' model that captures arbitrarily large dynamic bending and torsion of slender filaments including the highly nonlinear phenomenon of loop formation and intertwining. Two applications, underwater (marine) cables and DNA polymers, motivate this research.

Underwater cables tend to form loops and tangles in low tension regions that can hinder cable laying and recovery operations, attenuate signal transmission in fiber-optic cables, and can even lead to the formation of knots and kinks that damage cables. The formation of loops and tangles in long cables is topologically equivalent to the loops and supercoils that form in DNA. It is well known that the structural mechanics (i.e. deformation and stress) of DNA play a crucial role in the molecule's biological functions including gene expression. For instance, looping in DNA (often mediated by protein binding) is a crucial step in many gene regulatory mechanisms. A clear understanding of the structure-function relationships of these bio-molecules would enhance our ability to detect and to possibly control their biological functions. Functional involvement of DNA and/or proteins in several diseases is key to their diagnosis and treatment. Therefore the fundamental knowledge of the structure-function relationship may one day pave the way to new discoveries in medical research including future drug therapies.

This dissertation contributes a versatile rod model that can simulate the nonlinear dynamics of loop/tangle/supercoil formation and includes the multi-physical interactions for both large scale (cable) and small scale (DNA) systems. The dynamic rod model is validated by comparisons with published results from equilibrium rod theories which have also been benchmarked with laboratory-scale experiments. An extension that

accounts for 'self-contact' enables us to explore the dynamics of intertwining and thereby simulate cable tangling and DNA supercoiling. Finally, we focus on an example of protein-mediated looping of DNA that is also widely studied experimentally. We use the 'mechanical rod' model of DNA molecules to simulate its structural interactions with proteins/ enzymes during gene expression. Our results illustrate how the mechanical properties of DNA affect the chemical kinetics of DNA-protein interactions and thus regulate the gene expression.

Chapter 1

Introduction

This research contributes a computational 'rod' model that captures arbitrarily large dynamic bending and torsion of slender filaments including the highly nonlinear phenomenon of loop formation and intertwining. Two applications, underwater (marine) cables and DNA polymers, motivate this research. A brief introduction to the structure of DNA and its biological functions is given in Appendix 1 and also in [1] as further background to this research.

Underwater cables may form loops and tangles in regions where torsional deformations overcome the stiffening effects due to tension and bending rigidity. This loading scenario is often realized on the seabed as illustrated in Figure 1.1. In this context, loops are often termed 'hockles' and these can hinder cable laying and recovery operations, attenuate signal transmission in fiber-optic cables, and can even lead to the formation of knots and kinks that damage cables.
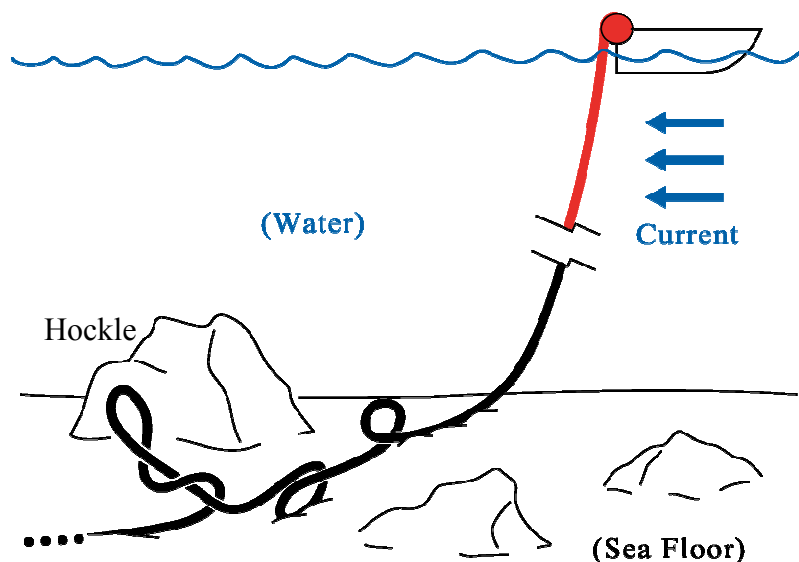
Figure 1.1 Low tension cable forming loops and tangles on the sea floor.

The formation of loops and tangles in long cables is topologically equivalent to the loops and supercoils that form in DNA. DNA, which is a long chain bio-polymer, is structurally similar to a rod with a diameter of 1.8 nanometers and lengths ranging from micrometer (viral plasmids[1], see Figure 1.2) to centimeter (human chromosomes[2]) scales. Despite its discrete structure at the atomic scale, its structure on long length scales can be effectively described by a continuum rod. The following quote from [1] serves to emphasize that DNA is indeed extremely long and slender.

> "The DNA from the longest individual human chromosome, if it were enlarged by a factor of 10^6, so that it became the width of ordinary kite string, would extend for about 100 km. Imagine sitting in a train traveling from Cambridge to London, or from Los Angeles to San Diego, and looking out of the window for the whole trip at a single DNA molecule and watching the genes go by!"
>
> <div align="right">- Calladine et al. [1]</div>
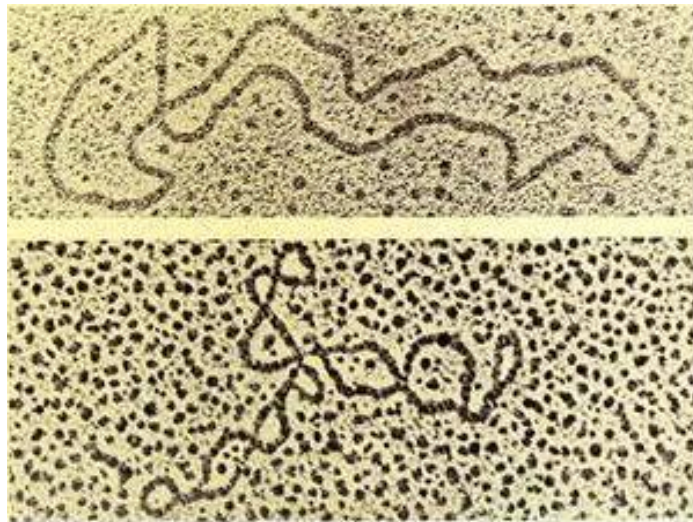
Figure 1.2 Electron micrographs of a DNA polymer in two different conformations (Courtesy: Lehninger et al. [2]). The interwound conformation (lower image) is an example of intertwining that is topologically equivalent to tangles in underwater cables.

---

[1] A "plasmid" is a closed loop DNA. It is typically found in viruses and "prokaryotes", the lower organisms (without a cell nucleus) like bacteria.
[2] A "chromosome" is a well-organized assembly of very long DNA wrapped around spool-shaped proteins called "histones". They are typically found in "eukaryotes", the higher organisms (having cell nucleus) like all animals.

Twist and curvature are the two important kinematic variables of long cables and strands of DNA that describe their topological structure. For instance, extreme twist and curvature enable DNA to pack (by a factor of up to 10,000) within the small confines of the cell nucleus or a viral capsid. In addition, twist and curvature can regulate replication and gene expression [1]. Many enzymes (proteins) can manipulate the twist and curvature of DNA to pack the molecule or to help expose the interior base pairs (chemical units that constitute the genetic code). Similarly, it is the twist and curvature of long cables that are responsible for the formation of hockles on the sea bed.

Dynamic behavior in both applications is influenced by hydrodynamic effects due to the surrounding fluid. For instance, underwater cables are subjected to substantial drag (high Reynolds number[3]), added fluid mass, and wave and current loading by the surrounding fluid environment. Likewise, DNA is subjected to substantial drag (Stokes regime, i.e. Low Reynolds number[4]) in addition to thermal fluctuations, hydrophobic interactions, as well as electrostatic screening effects.

Therefore nonlinear structural mechanics of a slender rod-like element in these applications require and understanding of the multi-physical environment and poses numerous challenges to both theoretical and computational modeling. This dissertation addresses these challenges, contributes a continuum-mechanics-based rod model that efficiently captures many of the aforementioned multi-physical behaviors, and also lays the foundation for future research in incorporating other physical behaviors in a common computational framework. The accuracy of the model has been carefully confirmed in the quasi-static limit using published results for equilibrium states and thus indirectly, by the published laboratory-scale experiments on nitinol rods that validate these equilibria [3]. This dissertation also presents new and intriguing conclusions regarding the mechanics of DNA looping and supercoiling and the looping and tangling of underwater cables. We shall now review both of these target applications in more detail as background to this dissertation.

---

[3] Inertial effects dominate viscous effects.
[4] Viscous effects dominate inertial effects..

1.1 Underwater (Marine) Cable Applications

Cables are deployed in the ocean for diverse applications including long-range signal transmission (electrical or optical), power transmission, sensor systems (e.g, hydrophone arrays), mooring lines, tow lines, and umbilicals. Depending on scales, other structural elements including pipelines and risers used for under sea oil recovery are well-described by considering them to be tensioned cable-like structures. The dynamics of cable laying operations, wave/current loading and other environmental conditions often introduce substantial dynamic cable behavior. Under extreme conditions, the dynamic behavior can be highly nonlinear and can even lead to loop and tangle formation. Looping and tangling of underwater cables severely degrade their performance and survivability in the ocean. For example, the loops (sometimes also referred to as 'hockles') may cause localized damage by kink formation. Kinks may prevent signal transmission in fiber optic cables. Loops and tangles may also promote knot formation and hinder the cable laying and recovery operations. Engineers and operators do not yet fully understand the basic mechanics of loop formation and the design/operation strategies needed to minimize their occurrence. Therefore, a major objective of this research is to explore the mechanics of loop/tangle formation and to contribute a predictive computational model for underwater cables. Observations made next offer qualitative insights on the conditions that lead to loop and tangle formation and motivate the research plan pursued in this dissertation.
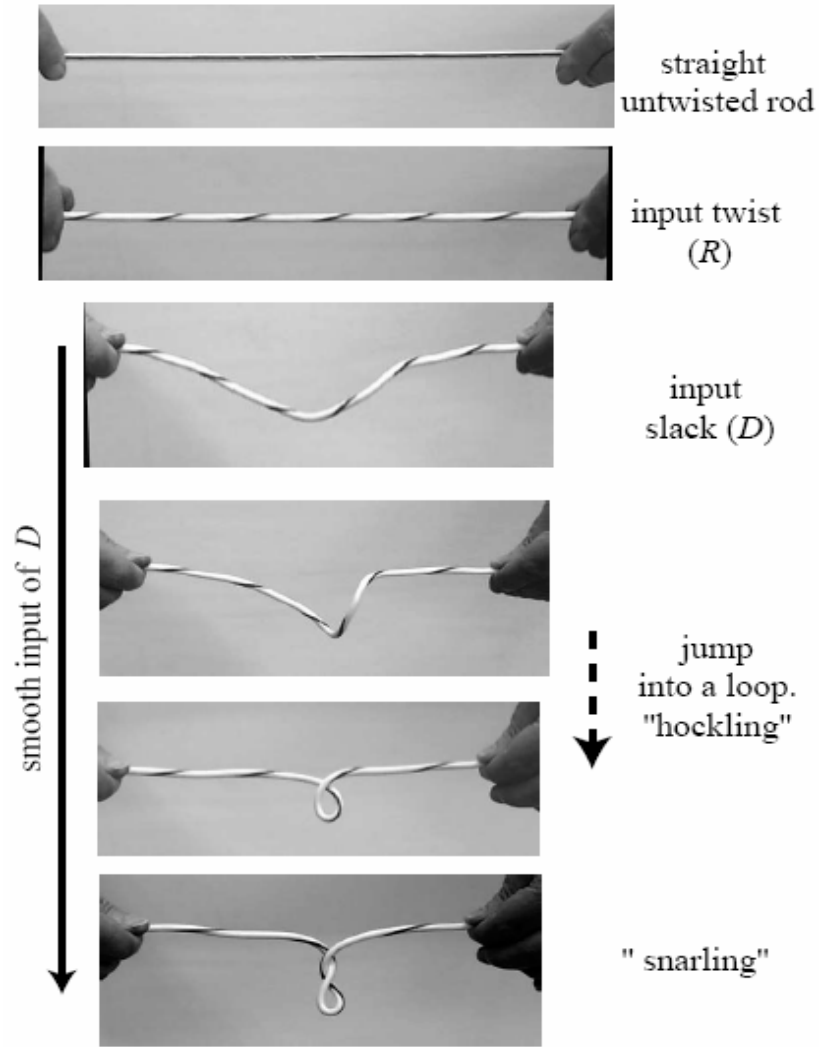
Figure 1.3 A twisted cable collapses under slack conditions and ultimately forms a loop or hockle as well as an intertwined 'snarl' (Courtesy: Goss et al. [4]).
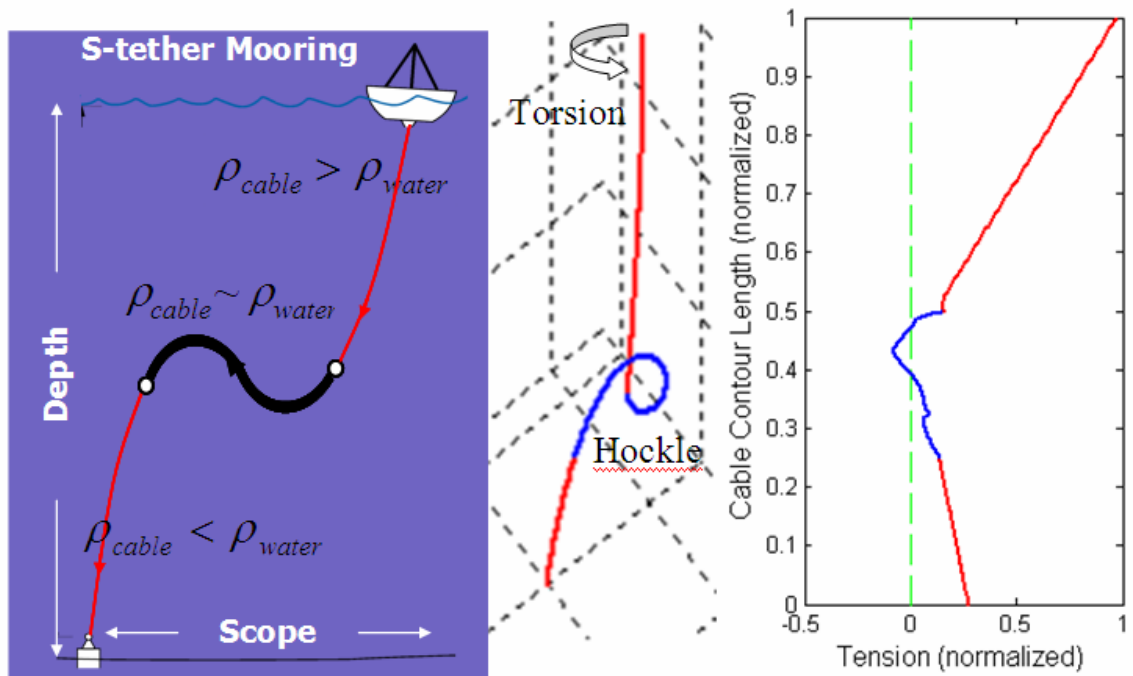
Figure 1.4 S-tether mooring collapses into a loop ('hockle') under torsion (due to yawing) in a low-tension zone. The symbol ρ represents density.

First, Figure 1.3 illustrates a simple experiment [4] wherein an initially taut but twisted cable is relaxed (slack added) so that its tension reduces. The twisted cable collapses to form loops (or 'hockles') that further intertwine (or 'snarl'). Subsequent re-tensioning of the cable may eliminate all loops. Moreover, adding greater twist in the cable requires greater tension to prevent its collapse into loops. Second, Figure 1.1 illustrates that the cables laid upon the sea floor develop *low-tension* regions (shown in black) where they preferentially form loops and tangles. Most often, cables are laid down on the seabed from a surface ship where they are originally wound on spools. The mere winding and unwinding on spools, however, may allow cable to,accumulate residual twist that renders them further susceptible to loop formation. Third, Figure 1.4 shows an example of S-tether cable that is designed to provide compliance in oceanographic moorings[5]. Frequently, this compliance serves to protect delicate instruments from ocean waves and currents. The design also prevents slack from developing on the seabed and thus minimizes cable wear and abrasion. The characteristic S-shape is achieved using

---

[5] Such compliance substantially reduces the tension developed under wave and current loading. It is typically needed in electro-optical-mechanical (EOM) cables that are very stiff in extension.

distributed weights and buoyant elements in specific regions of the cable so as to create buoyant regions. Such designs also reduce the overall cable tension (an advantage from the perspective of cable-strength and durability), but they also render the system susceptible to loop formation in the *low-tension* S-shaped regions as shown in Figure 1.4. Such loop formation could be initiated by yawing of the buoy that would add twist to the cable or could also be initiated by other kinds of wave/current loading scenarios.

From the above observations, following trends are reasonbly intuitive.

- Twist in the cable promotes loop formation while tension in the cable suppresses loop formation.
- The large deformations inherent in loop/tangle formation are dominated by flexural and torsional effects.
- Looping/tangling results in negligible changes in the overall (contour) length of the cable.

To accurately simulate the flexural and torsional behavior, one must treat the cable as a rod-like element that has stiffness due to flexure and torsion. (Flexural and torsional effects are not captured in 'string-like' models that treat the cable as perfectly flexible in flexure and torsion; refer to Triantafyllou and Howell [5] and to Burgess [6]). Due to stiffness in flexure and torsion, loop formation in a rod is initiated by structural instabilities (or buckling) under compression and/ or torsion; refer, for example, to the buckling conditions developed by Greenhill (described in Timoshenko and Gere [7]) and by Zachman [8]. In order to probe and simulate the mechanics of loop formation in underwater cables, the following challenges are identified for computational modeling:

- accounting for arbitrarily large 3-dimensional deformation (nonlinear mechanics),
- including hydrodynamic drag (Morison drag and added mass effects [9]),
- capturing dynamic self-contact, a pre-requisite to model intertwining.

These challenges are addressed in detail in this dissertation.

1.2 Mechanics of DNA: Looping and Supercoiling

Deoxyribonucleic acid (DNA) is a long chain biopolymer molecule that has been characterized [1] as "the most central substance in the workings of all life on Earth." Located within the nucleus of our cells, DNA contains the coded (genetic) information needed to synthesize all proteins and thus sustain life. Replication and segregation of DNA are used to transfer this genetic information from one cellular generation to the next. These major biological functions of DNA follow not just from its chemical make up but also from its physical 'structure'. By 'structure', we refer to the often complex shape and state of stress of this long molecule and how they ultimately affect its biological functions. A clear understanding of the structure-function relationships of these bio-molecules would enhance our ability to detect and to possibly control their biological functions. Functional involvement of DNA and/or proteins in several diseases is a target point for their diagnosis and treatment. Therefore such fundamental knowledge of the structure-function relationship may pave the way to new horizons in medical research including future drug therapies, more effective ways of pathological diagnoses, development of new vaccines, etc. This is an ambitious and scientifically-rich area of research which is perhaps best introduced by posing three fundamental questions:

- How does the structural mechanics of DNA influence gene expression?
- How does the base (monomer) sequence of DNA influence its structural mechanics?
- How do gene-regulating proteins manipulate structural changes in DNA?

A basic step towards resolving these questions is to develop a physical model of DNA that can simulate its structural mechanics. To start, we need to first describe the basic chemistry and structure of DNA, the multiple length-scales involved, and the major biological functions that DNA performs. In doing so, we will also discuss why we believe it is promising to study the long-length scale mechanics of DNA by employing methods and models from the field of cable/rod dynamics. The following description of DNA

structure and function is also briefly revisited in Appendix 1 along with some additional intriguing information/details.
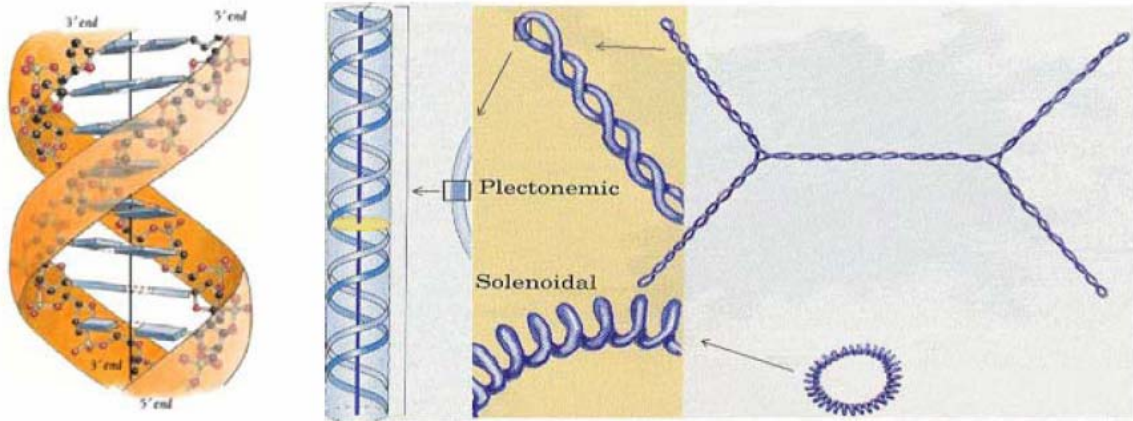
Figure 1.5 DNA shown on three length scales. Smallest scale (left) shows double-helix structure (sugar-phosphate chains and base-pairs). Intermediate scale (middle) shows how several double-helices form a continuous piece of double-stranded DNA. Largest scale (right) shows how the strand ultimately curves and twists in forming supercoils (one interwound or plectonemic, and one solenoidal). (Courtesy: Branden and Tooze [10] and Lehninger et al. [2]).

Figure 1.5 illustrates a DNA molecule on three different length scales as reproduced from several sources [1-3]. The smallest length scale (far left) shows a segment of the familiar 'double-helix' which has a diameter of approximately 2 nanometers (nm). One complete helical turn is depicted here and this extends over a length of approximately 3 nm. The double helices, which wind like the supports of a spiral staircase, are composed of two polynucleotide chains which in turn are made up of four different nucleotides. Each nucleotide is made from a five-carbon sugar to which one or more phosphate groups and a nitrogen containing base are attached. The phosphate groups render the molecule negatively charged along its backbone. There are four types of bases that include adenine (abbreviated A), guanine (abbreviated G), cytosine (abbreviated C) and thymine (abbreviated T). The four bases often bond in only two unique, complementary pairs, namely A with T and C with G. The sugar-phosphate groups of the nucleotides are covalently linked into long chains (highlighted in orange) that form the backbone of DNA. Pairing of the two polynucleotide strands is achieved by hydrogen bonding between the nucleotide bases (highlighted in blue) that fill the small voids between the single DNA strands. It is this linear sequence of base-pairs that constitute the genetic

9

code. Within the small voids between these chains lie the 'base-pairs' (highlighted in blue). This chemical structure and the rules for 'base-paring' follow from the seminal discoveries of Franklin and Gosling [11] and Watson and Crick [12, 13]. The base-pairs are hydrophobic and therefore must avoid contact with the surrounding aqueous environment within the cell. To this end, the double-helices effectively wrap around the base-pairs, thereby shielding them from the surrounding water molecules [1]. There are approximately 10.5 base-pairs in one helical turn for the common 'B' form of DNA which also forms a right-handed helix as depicted in Figure 1.5.

On an intermediate spatial scale (middle of Figure 1.5), the double helix appears as a solid 'strand' of DNA that might extend over tens to hundreds of helical turns (approximately tens to hundreds of nanometers). This is the approximate length scale of a 'gene' which is a portion of a DNA strand (i.e. a specific base-pair sequence) that controls a discrete hereditary characteristic. The base-pair sequence within a gene constitutes a chemical code for the production of a specific protein elsewhere within the cell. The major biological function of DNA is to store these chemical codes and to make them available for protein production through a process known as 'transcription'. In addition, the same chemical codes are passed from one cell generation to the next through a process known as 'replication'. Thus, transcription and replication are key biological processes essential for the functions of DNA. Transcription and replication are strongly influenced by the structure of the molecule on even longer length scales.

The human genome contains about 3.2 billion nucleotides organized into 24 different chromosomes. The total length of our DNA is about 1 m, which is about five orders of magnitude larger than a typical cell. These observations confirm that DNA is an exceedingly long (and flexible) molecule. The long-length scale structure of DNA is illustrated to the far right in Figure 1.5. Here the long DNA strand may contain thousands to millions of base-pairs and resemble a highly curved and twisted filament with lengths ranging from micron to millimeter scales. The long-length curving/twisting of this strand is called 'supercoiling' and two generic types of supercoils are illustrated to the far right of Figure 1.5. One type, referred to as an 'interwound supercoil' (or 'plectoneme'), leads

to an interwoven structure where the strand wraps upon itself with many sites of apparent 'self-contact' (referred to as 'excluded volume effects' in this context). By contrast, a 'solenoidal supercoil' possesses no self-contact and resembles a coiled spring or telephone cord. DNA must supercoil for several key reasons. First, supercoiling provides an organized means to compact these very long molecules (by as much as 10^4) enabling them to fit within the small confines of the cell nucleus. An unorganized compaction would hopelessly tangle the strand and render it useless as a medium for storing the coded information. Though the solenoidal form achieves greater compaction (as needed for packaging it inside a cell nucleus) than does the plectonemic form, it is generally not observed unless stabilized by certain proteins (e.g. spool-shaped proteins called 'histones'). For isolated DNA in solution, the plectonemic form is stable and is mostly observed in the laboratory [2]. Second, supercoiling may play an important role in the biological processes of transcription and replication. For instance, protein-mediated looping of DNA on long-length scales is a crucial step in many gene regulatory mechanisms [14-18], a phenomenon that will be studied in some detail in this dissertation.
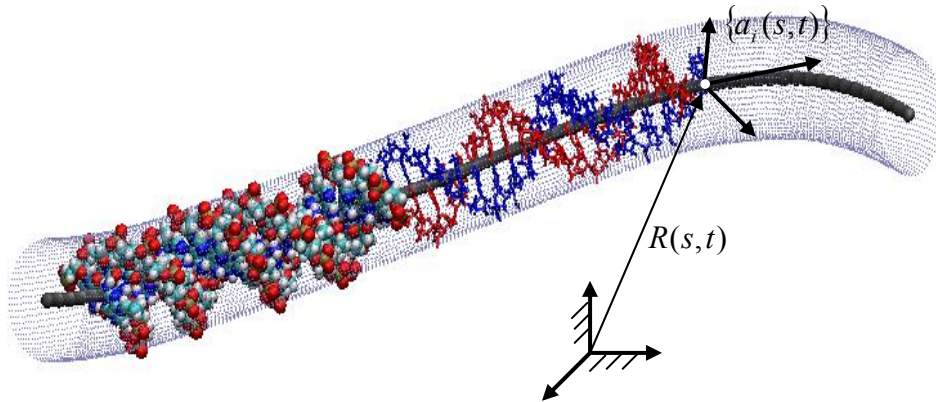
Figure 1.6 Rod model of (ds) DNA on long-length scales. Helical axis of duplex defines the rod centerline which forms a three-dimensional space curve located by $R(s,t)$.

It is on this largest length scale that DNA starts to resemble a cable or a 'rod'; refer to Figure 1.6. Consider for instance the striking similarities of DNA loops and supercoils to the loops and tangles (hockles) that form in low tension cables like those illustrated in Figure 1.1. The models and methods used to understand how loops and tangles form in

cables provide a natural means to explore the looping and supercoiling of DNA, provided one incorporates the specialized physical laws that are dominant at these length scales (refer to Appendix 3 and Howard [19]). Moreover, the curved and twisted structures that appear on long-length scales suggest the important roles played by the bending and torsion of a DNA strand. Cable models that capture bending and torsion employ 'rod' theory. Indeed, the use of rod theory is reasonably well-established in the literature on DNA modeling as reviewed by Schlick [20] and Olson [21].

DNA in live environment is often untwisted by up to 5% of its nominal (stress-free) helical twist and is compressed within the small confines of cell (or viral capsid). This combination of low-tension/ compression and torsion renders long lengths of DNA susceptible to structural instabilities (see Appendix 2) that produce loops and supercoils. The resulting structural changes on long length scales can be captured by rod models.

While rod models may be naturally suited for describing the mechanics of DNA on long-length scales that extend over tens to millions of base pairs, they cannot describe the fine-scale structure of DNA at the base-pair level. Such fine-scale models of DNA can only be resolved through atom-by-atom descriptions of the DNA duplex (and the surrounding water molecules and any bound proteins/agents). However, the resulting molecular dynamics (MD) models rapidly grow to huge proportions and this limits their utility to very short (e.g., nanosecond) time scales and to very short (e.g., nanometer) length scales. Thus, full molecular dynamics models cannot be used to simulate the long-length scale looping and supercoiling of DNA; see, for example, [22-24]. Other modeling techniques do exist (e.g., Monte Carlo or Brownian/Langevin dynamics simulations of discrete beaded-chain models and other statistical mechanics models of polymers [25]) that provide alternatives to MD simulation, see, for example studies reviewed in [20, 21, 26]. Beaded-chain models (e.g. [27, 28]) have been particularly useful in capturing the diverse physical interactions of DNA on long-length scales, such as its thermal fluctuations caused by random bombardments of water molecules, hydrodynamic interactions and electrostatic interactions of its negatively charged sugar-phosphate backbone. These physical interactions of DNA with its surrounding are discussed in Appendix 3 and

differing opinions on their importance are also cited. Discrete models however differ in their material laws from continuum rod models as explained in detail by Klapper and Qian [26] and their applicability depend on the context. In general, all these models (MD, beaded-chain and continuum rod) play important roles in building our understanding of the DNA mechanics as they involve multiple length/time scales and multi-physical effects.

In order to simulate the structural mechanics of DNA as a continuum rod, some or all of the following challenges may need to be addressed:

- arbitrarily large 3-dimensional deformation (nonlinear mechanics)
- hydrodynamic drag (Stokes regime) and interactions (coupling)[6]
- excluded volume effects (self-contact)
- sequence-dependent material laws (constitutive laws)
- thermal kinetics
- electrostatics

In the case of DNA, the modeling challenges are amplified by the fact that the material laws and parameters for other physical interactions are not well-characterized. Hence the computational model needs to be general enough to accommodate future knowledge of these functions (material laws) and parameters. We also further note that any inclusion of thermal kinetics and hydrodynamics must respect the 'fluctuation-dissipation theorem', refer to [19], and that the modeling of excluded volume effects is not isolated from the modeling of electrostatics.

1.3 Research Objective

The overall objective of this dissertation is to develop a versatile computational rod model that describes the nonlinear dynamics of highly contorted cables and DNA strands

---

[6] With hydrodynamic interactions, a segment of DNA transmits a disturbance to another segment not only through the structural path but also through the fluid path. In contrast, hydrodynamic drag captures only the dissipation of the fluid and not any possible disturbances of the structure to the fluid.

including looping and intertwining. The major challenge is to identify and include only the dominant structural properties and physical interactions that have strong influence on the resulting dynamics while ignoring those responsible for only weak influences. The following lists summarize the candidate structural properties and physical interactions which are included (indicated with a ✓) or currently neglected (indicated with a ×) :

Structural Properties:

- Arbitrarily large deformations due to bending and torsion ✓
- Dynamics due to inertia and/ or dissipation ✓
- Self-contact (or excluded volume effects) ✓
- Ability to accommodate wide range of material laws ✓
- Non-homogeneity (discrete or continuous) ✓

Physical Interactions:

- Hydrodynamic drag (at both high and low Reynolds numbers) ✓
- Hydrodynamic interactions (fluid path coupling) ×
- Thermal kinetics ×
- Electrostatics ×

Our goal is to address the most important features first and leave features of debatable importance for future consideration. The computational rod model in this dissertation incorporates all the features marked with ✓ above and we also suggest strategies for including the features marked with × above. In this context, we quickly note that hydrodynamic interactions and electrostatics are of disputed importance as discussed in Appendix 3. The formulation of thermal kinetics, however, is an ongoing research effort of our research group which is beyond the scope of this dissertation.

1.4 Scope of Dissertation and Previous Rod Theories

Advancements in rod theories are comprehensively reviewed in [29]. The earliest theories focus on 'equilibrium' (*static*) mechanics and originate from the 'linear' (small deformation) theories of Timoshenko and Euler-Bernoulli (described in Timoshenko and Gere [7]). For instance, refer to the *linear* buckling analyses of rod under prescribed tension/compression and torsion by Greenhill for "pinned-pinned' boundary conditions (described in Timoshenko and Gere [7]) and by Zachman [8] for 'clamped-clamped' boundary conditions. 'Nonlinear' (large deformation) equilibrium theories have evolved from 'elastica' models that describe large rotations of the rod cross-section. Elastica theory represents a special case of Kirchhoff/Clebsch rod theory (described in Antman [29] and Love [30]) that frequently employ a 'linear elastic constitutive law' for bending and torsion.

Analyses using *nonlinear equilibrium* rod theory often appear in the context of studying cable hockling; refer to Zajac [31], Yabuta [32] and Coyne [33]. These studies employ *equilibrium* rod theory to evaluate the cable torque and tension required to initiate a "looping instability" and the converse "pop-out" instability which destabilizes the cable loop. Extensions that incorporate three-dimensional equilibrium forms, their local stability, and spatial complexity are provided by Perkins and co-workers [34-36]. A recent summary of the bifurcations responsible for looping and pop-out in twisted rods with clamped ends is presented in Heijden et al. [3] together with compelling experimental results on (macro-scale) metal-alloy (nitinol) rods.

To describe supercoiling of DNA, numerous studies have employed rod theories also under *equilibrium conditions* [3, 37-50] starting with Benham [37, 38] who uses a 'hyperelastic', isotropic rod. The use of an isotropic (circular) rod to represent the structure of the double helix is specifically addressed by Maddocks and co-workers [39, 40] who conclude that bending anisotropy at the base-pair scale quickly averages to an effective isotropic rod on longer-length scales due to the high intrinsic twist (~10.5 base-

pairs/per helical turn) of the double-helix. DNA also has non-homogeneous material properties (including stiffness[7] and stress-free shape) due its varying base-pair sequence along its length. Non-homogeneity (sequence-dependent geometry and stiffness) in 'linear elastic' rod models is addressed by Manning et al [41]. The studies [3, 37-50] have contributed a fundamental understanding of the equilibrium states that describe supercoiled geometries (solenoidal and interwound), the stability of these states, and the physical parameters that control their 'bifurcations' [42, 45-50]. Much of this understanding derives from the fact that, in the absence of body-forces, the governing equilibrium equations are integrable which greatly aids subsequent bifurcation analyses. Modeling the mechanics of interwound supercoils requires formulating "self-contact" in rod theory and this challenge has only recently been addressed [3, 43, 44] in the context of closed loops (DNA "plasmids") [43, 44] and open strands with clamped ends [3]. Schlick [20] and some of the above studies, [3, 35, 48] also noted the topological equivalence of 'supercoils' in DNA and 'hockles' in marine cables.

The studies cited above all employ *equilibrium* calculations to predict supercoiled states of DNA or hockled states of cables. It is however well-known that both planar and non-planar equilibrium states may become unstable under specific bifurcation conditions; for instance, the loop formation instabilities noted in [3, 34] and the opposite "pop-out" instabilities noted in [3, 33]. These instabilities initiate large *dynamic* responses which may also produce nonlinear transitions to more energetically favorable equilibria. Fundamental dynamical phenomena of supercoils and hockles are left unaddressed, including the existence of multiple supercoiled states in DNA and the possible nonlinear transitions between these states [1]. The need for dynamic treatments using rod theory is recognized, but not pursued in the above studies by Coleman et al. [43] and by Heijden et al. [3].

Only recently, very few studies [51-55] have developed *dynamic* rod models sufficient for describing the dynamic evolution of loops. Their features are contrasted with some

---

[7] For example, AT rich zones are believed to be softer than GC rich zones because the AT pair has only two hydrogen bonds while the GC pair has three hydrogen bonds.

important contributions of this dissertation in

Table 1.1. The only dynamic rod model in the context of DNA mechanics is one developed by Klapper [51] to study the slow (artificially damped) evolution of self-contact and intertwining in closed loop biological filaments, e.g. DNA plasmids. Dynamical rod models are more prevalent for simulating underwater cables [52-55]. All these models capture highly dynamic responses of underwater cables with more realistic hydrodynamic forces, Morison drag and added mass effects [9] but without self-contact. The model developed by Gobat et al. [53, 54] also captures dynamic tension (extensional waves) by adding a linear constitutive law in extension for a Kirchhoff rod. This however is a minor feature when considering the mechanics responsible for looping and supercoiling.

In the *dynamic* formulation, the nonlinear equations of the model are not integrable in closed form and necessitate a numerical search of the solution at each time step. Along with this necessity come many numerical challenges. Numerical recipes for solving nonlinear differential equations suffer from fundamental trade-offs between speed, accuracy and numerical stability, as stated by the Dahlquist theorem [58]. The Generalized-α method developed by Chung and Hulbert [56] and extended to cable dynamics applications by Gobat and Grosenbaugh [53] has optimal numerical properties within the constraints of Dahlquist theorem. The method is becoming increasingly popular in both industry and academia.

Table 1.1 also contrasts numerical features of all the dynamic rod models which we elaborate upon in Chapters 3.

All of the previous dynamic rod models described above [51-55] also assume the rod to be homogeneous and straight when stress-free (no intrinsic curvature or twist). We have already described that these assumptions fall short when considering the sequence-dependent mechanics of DNA. In addition, the helical construction of the DNA duplex and of synthetic and wire rope cables (described in Costello [59]) gives rise to a specific kind of anisotropy due to chirality (termed as 'hemitropy' by Healey [60]). In contrast to isotropic rods, the behavior of a hemitropic or chiral rod differs from that of its mirror image [60].

Table 1.1 Comparison of computational dynamic rod models

	Klapper [51]	Gobat et al. [53, 54]	Sun et al. [52], Gatti et al. [55]	This Dissertation
year	1995	2000	1994, 2002	2003
Modeling Features				
Self-Contact	✓	×	×	✓
Non-homogeneity and Stress-free Curvature	×	×	×	✓
Chirality	×	×	×	✓
Hydrodynamic forces	Formulation for low Reynolds number to approximate quasi-static solutions.	Buoyancy, standard Morison drag and added mass	Buoyancy, standard Morison drag and added mass	Two different formulations for low and high Reynolds number.
Numerical Features				
Numerical Scheme	RK[8] method in time, centered difference scheme in space	Generalized-α method [53, 56] in time, box method in space	Newmark-like scheme (Generalized trapezoidal method) in time, RK[8] method in space	Generalized-α method [53, 56] in both space and time.
Rotation parameterization	Unit vectors	Euler Parameters	Euler parameters	Incremental rotation [57]
Order of PDE		13th order	13th Order	12th Order

---

[8] Runge-Kutta Method.

1.5 Summary of Research Contributions

The contributions of this dissertation can be broadly divided among contributions towards a general computational rod model, and contributions towards understanding the mechanics of looping and intertwining of cable and of DNA through four 'case studies'. We begin with three contributions that extend existing computational rod models.

Computational Rod Model

- **General formulation of hydrodynamic forces and self-contact**

We formulate a computational dynamic rod model in Chapter 2 that incorporates all the capabilities of the previous dynamic models [51-55] and adds generalized body forces that can capture the effects of hydrodynamic drag (at both high and low Reynolds number), added mass, buoyancy and dynamic self-contact. The comparisons with and contributions over previous formulations are summarized in

Table 1.1.

- **Modeling non-homogenous and non-isotropic rods**

Our formulation accounts for 1) anisotropy in bending stiffness, 2) intrinsic twist and curvature, and 3) non-homogeneous stiffness and density. These effects will likely play a key role in several case studies of both cables (synthetic and wire ropes) and DNA (sequence-dependent properties). For instance, the chirality of cables and the DNA duplex leads to coupling of tension and torque as demonstrated by examples in Chapter 5.

- **Numerical enhancements**

We have improved overall computational performance in our algorithms by implementing three strategies: 1) Generalized-α method [53, 56] in both space and time, 2) a novel formulation of equations of motion that allows us to circumvent the use of Euler parameters and thereby rendering the minimum order (12th order) model, and 3) the judicious choice of field variables in terms of velocities, angular velocities and curvature/twist components (instead of displacements and Euler angles). This is further elaborated in Chapter 3 where we describe the computational formulation.

Case Studies for Cables and DNA

Arguably the most interesting contributions of this dissertation follow from the application of the computational rod model to the looping and intertwining of cables and DNA. In doing so, we also carefully benchmark our results as described next.

- **Benchmarking**

As a first example, we elected to carefully benchmark our dynamical solutions with known equilibrium solutions for limiting cases of slow (quasi-static) loading. Doing so highlights the accuracy of our formulation. We refer to Heijden et al. [3] who catalogues the equilibria and bifurcations of clamped-clamped rods which in turn have been validated by laboratory-scale experiments on nitinol rods. The dynamic rod model

summarized in Chapter 4 not only reproduces these equilibria under quasi-static loading but also captures large dynamic transitions between equilibrium paths. In addition, we discover new hysteresis effects that result from our dynamical treatment.

- **Tension-Torque Coupling**

As a second example, we study in Chapter 5 the influence of chirality by adding tension-torque coupling to the rod constitutive law. This coupling is motivated by the helically-wound construction of common wire and synthetic cables as well as the DNA duplex. The impact of this coupling is highlighted through new solutions to the benchmark problem first introduced in Chapter 4.

- **Dynamics of self-contact and intertwining**

As a third example, we model self-contact so as to capture the dynamic evolution of intertwining in response to torsional buckling. The intertwined shapes resemble hockles in underwater cables and the plectonemic supercoils of DNA. These results highlight the importance of torsion as a dominant mechanism responsible for hockles and plectonemes. This is covered in Chapter 6.

- **Protein-mediated DNA looping**

Looping in DNA is an important mechanism for gene regulation. Gene expression can be regulated by specific proteins that deform DNA into a loop. One of the most studied examples of this regulation is the Lac gene in the bacterium *E.Coli* that is mechano-chemically controlled by 'Lactose-Repressor' protein. In chapter 7, we employ the rod model to simulate DNA looping mediated by 'Lactose-Repressor' for both the 'wild-type' (naturally occurring) DNA sequence and variety of other 'designed sequences' with large intrinsic bends. The computations provide a fundamental understanding of the energetics and topology the DNA loops. They also elucidate experimentally observable trends of looping rates and stability of the designed sequences and the overall influence of sequence-dependent instrinsic curvature in the looping process.

Finally this dissertation lays out the foundation for many future/ongoing research endeavors with.some described in Chapter 8.

References:

1. Calladine, C.R., et al., *Understanding DNA, the Molecule and How It Works*. 3 ed. 2004, Amsterdam: Elsevier Academic Press.
2. Lehninger, A.L., D.L. Nelson, and M.M. Cox, *Lehninger Principles of Biochenistry*. 4 ed. 2005, New York: W. H. Freeman.
3. van der Heijden, G.H.M., et al., *Instability and self-contact phenomena in the writhing of clamped rods*. International Journal Of Mechanical Sciences, 2003. **45**(1): p. 161-196.
4. Goss, V.G.A., et al., *Experiments on snap buckling, hysteresis and loop formation in twisted rods*. Experimental Mechanics, 2005. **45**(2): p. 101-111.
5. Triantafyllou, M.S. and C.T. Howell, *Dynamic-Response of Cables under Negative Tension - an Ill-Posed Problem*. Journal of Sound and Vibration, 1994. **173**(4): p. 433-447.
6. Burgess, J.J., *Bending stiffness in a simulation of undersea cable deployment*. International Journal of Offshore and Polar Engineering, 1993. **3**(3): p. 197-204.
7. Timoshenko, S.P. and J.M. Gere, *Theory of Elastic Stability*. 2 ed. 1961, New York: McGraw-Hill.
8. Zachmann, D.W., *Non-Linear Analysis Of A Twisted Axially Loaded Elastic Rod*. Quarterly Of Applied Mathematics, 1979. **37**(1): p. 67-72.
9. Morison, J.R., et al., *The Force Exerted By Surface Waves On Piles*. Transactions Of The American Institute Of Mining And Metallurgical Engineers, 1950. **189**: p. 149-154.
10. Branden, C. and J. Tooze, *Introduction to Protein Structure*. 2 ed. 1999, New York: Garland Publishing.
11. Franklin, R.E. and R.G. Gosling, *Molecular Configuration in Sodium Thymonucleate*. Nature, 1953. **171**(4356): p. 740-741.
12. Watson, J.D. and F.H.C. Crick, *Genetical Implications of the Structure of Deoxyribonucleic Acid*. Nature, 1953. **171**(4361): p. 964-967.
13. Watson, J.D. and F.H.C. Crick, *Molecular Structure of Nucleic Acids - a Structure for Deoxyribose Nucleic Acid*. Nature, 1953. **171**(4356): p. 737-738.
14. Halford, S.E., A.J. Welsh, and M.D. Szczelkun, *Enzyme-mediated DNA looping*. Annual Review of Biophysics and Biomolecular Structure, 2004. **33**: p. 1-24.
15. Ptashne, M., *A Genetic Switch*. 2 ed. 1992, Cambridge, Mass: Cell Press : Blackwell Scientific Publications.
16. Ptashne, M. and A. Gann, *Genes and Signals*. 1 ed. 2002, Cold Spring Harbor, N.Y.: Cold Spring Harbor Laboratory Press.
17. Schleif, R., *DNA Looping*. Annual Review of Biochemistry, 1992. **61**: p. 199-223.
18. Semsey, S., K. Virnik, and S. Adhya, *A gamut of loops: meandering DNA*. Trends in Biochemical Sciences, 2005. **30**(6): p. 334-341.
19. Howard, J., *Mechanics of Motor Proteins and the Cytoskeleton*. 2001, Sunderland: Sinauer Associates.
20. Schlick, T., *Modeling Superhelical DNA - Recent Analytical And Dynamic Approaches*. Current Opinion In Structural Biology, 1995. **5**(2): p. 245-262.

21. Olson, W.K., *Simulating DNA at low resolution.* Current Opinion in Structural Biology, 1996. **6**(2): p. 242-256.

22. Kollman, P.A., et al., *Calculating structures and free energies of complex molecules: Combining molecular mechanics and continuum models.* Accounts of Chemical Research, 2000. **33**(12): p. 889-897.

23. Schlick, T., et al., *Computational challenges in simulating large DNA over long times.* Computing in Science & Engineering, 2000. **2**(6): p. 38-51.

24. Beveridge, D.L. and G. Ravishanker, *Molecular-Dynamics Studies of DNA.* Current Opinion in Structural Biology, 1994. **4**(2): p. 246-255.

25. Flory, P.J., *Statistical mechanics of chain molecules.* 1989, Munich ; New York : New York, NY :: Hanser Publishers ; Distributed in the USA by Oxford University Press.

26. Klapper, I. and H. Qian, *Remarks on discrete and continuous large-scale models of DNA dynamics.* Biophysical Journal, 1998. **74**(5): p. 2504-2514.

27. Klenin, K., H. Merlitz, and J. Langowski, *A Brownian dynamics program for the simulation of linear and circular DNA and other wormlike chain polyelectrolytes.* Biophysical Journal, 1998. **74**(2): p. 780-788.

28. Hsieh, C.C., L. Li, and R.G. Larson, *Modeling hydrodynamic interaction in Brownian dynamics: simulations of extensional flows of dilute solutions of DNA and polystyrene.* Journal Of Non-Newtonian Fluid Mechanics, 2003. **113**(2-3): p. 147-191.

29. Antman, S.S., *Nonlinear Problems in Elasticity.* 2 ed. 2004, New York: Springer-Verlag.

30. Love, A.E.H., *A Treatise on the Mathematical Theory of Elasticity.* 4 ed. 1944, New York: Dover Publications.

31. Zajac, E.E., *Stability of two planar loop elasticas.* Trans. ASME Ser. E. J. Appl. Mech., 1962. **29**: p. 136--142.

32. Yabuta, T., *Submarine Cable Kink Analysis.* Bulletin of the Jsme-Japan Society of Mechanical Engineers, 1984. **27**(231): p. 1821-1828.

33. Coyne, J., *Analysis Of The Formation And Elimination Of Loops In Twisted Cable.* Ieee Journal Of Oceanic Engineering, 1990. **15**(2): p. 72-83.

34. Lu, C.L. and N.C. Perkins, *Nonlinear Spatial Equilibria And Stability Of Cables Under Uniaxial Torque And Thrust.* Journal Of Applied Mechanics-Transactions Of The Asme, 1994. **61**(4): p. 879-886.

35. Lu, C.L. and N.C. Perkins, *Complex Spatial Equilibria Of U-Joint Supported Cables Under Torque, Thrust And Self-Weight.* International Journal Of Non-Linear Mechanics, 1995. **30**(3): p. 271-285.

36. Gottlieb, O. and N.C. Perkins, *Local and global bifurcation analyses of a spatial cable elastica.* Journal of Applied Mechanics-Transactions of the Asme, 1999. **66**(2): p. 352-360.

37. Benham, C.J., *The Role of the Stress Resultant in Determining Mechanical Equilibria of Superhelical DNA.* Biopolymers, 1987. **26**(1): p. 9-15.

38. Benham, C.J., *Onset of writing in circular elastic polymers.* Physical Review A (General Physics), 1989. **39**(5): p. 2582-2586.

39. Rey, S. and J.H. Maddocks. *Buckling of an Elastic Rod with High Intrinsic Twist.* in *16th IMACS World Congress.* 2000.

40.   Kehrbaum, S. and J.H. Maddocks. *Effective Properties of Elastic Rods with High Intrinsic Twist*. in *16th IMACS World Congress*. 2000.

41.   Manning, R.S., J.H. Maddocks, and J.D. Kahn, *A continuum rod model of sequence-dependent DNA structure*. Journal Of Chemical Physics, 1996. **105**(13): p. 5626-5646.

42.   Tobias, I., D. Swigon, and B.D. Coleman, *Elastic stability of DNA configurations. I. General theory*. Physical Review E, 2000. **61**(1): p. 747-758.

43.   Coleman, B.D., D. Swigon, and I. Tobias, *Elastic stability of DNA configurations. II. Supercoiled plasmids with self-contact*. Physical Review E, 2000. **61**(1): p. 759-770.

44.   Gonzalez, O., et al., *Global curvature and self-contact of nonlinearly elastic curves and rods*. Calculus of Variations and Partial Differential Equations, 2002. **14**(1): p. 29-68.

45.   Ramachandran, G. and T. Schlick, *Buckling transitions in superhelical DNA: Dependence on the elastic constants and DNA size*. Biopolymers, 1997. **41**(1): p. 5-25.

46.   Olson, W.K. and V.B. Zhurkin, *Modeling DNA deformations*. Current Opinion in Structural Biology, 2000. **10**(3): p. 286-297.

47.   Fain, B., J. Rudnick, and S. Ostlund, *Conformations of linear DNA*. Physical Review E, 1997. **55**(6): p. 7364-7368.

48.   Stump, D.M., W.B. Fraser, and K.E. Gates, *The writhing of circular cross-section rods: undersea cables to DNA supercoils*. Proceedings of the Royal Society of London Series a-Mathematical Physical and Engineering Sciences, 1998. **454**(1976): p. 2123-2156.

49.   Stump, D.M., P.J. Watson, and W.B. Fraser, *Mathematical modelling of interwound DNA supercoils*. Journal of Biomechanics, 2000. **33**(4): p. 407-413.

50.   Thompson, J.M.T., G.H.M. van der Heijden, and S. Neukirch, *Supercoiling of DNA plasmids: mechanics of the generalized ply*. Proceedings of the Royal Society of London Series a-Mathematical Physical and Engineering Sciences, 2002. **458**(2020): p. 959-985.

51.   Klapper, I., *Biological applications of the dynamics of twisted elastic rods*. Journal Of Computational Physics, 1996. **125**(2): p. 325-337.

52.   Sun, Y. and J.W. Leonard, *Dynamics of ocean cables with local low-tension regions*. Ocean Engineering, 1998. **25**(6): p. 443-463.

53.   Gobat, J.I. and M.A. Grosenbaugh, *Application of the generalized-alpha method to the time integration of the cable dynamics equations*. Computer Methods In Applied Mechanics And Engineering, 2001. **190**(37-38): p. 4817-4829.

54.   Gobat, J.I., M.A. Grosenbaugh, and M.S. Triantafyllou, *Generalized-alpha time integration solutions for hanging chain dynamics*. Journal Of Engineering Mechanics-Asce, 2002. **128**(6): p. 677-687.

55.   Gatti-Bono, C. and N.C. Perkins, *Dynamic analysis of loop formation in cables under compression*. International Journal Of Offshore And Polar Engineering, 2002. **12**(3): p. 217-222.

56.   Chung, J. and G.M. Hulbert, *A Time Integration Algorithm For Structural Dynamics With Improved Numerical Dissipation - The Generalized-Alpha*

Method. Journal Of Applied Mechanics-Transactions Of The Asme, 1993. **60**(2): p. 371-375.

57.   Bottasso, C.L. and M. Borri, *Integrating finite rotations.* Computer Methods In Applied Mechanics And Engineering, 1998. **164**(3-4): p. 307-331.

58.   Dahlquist, G., *A special stability problem for linear multistep methods.* BIT, 1963. **3**: p. 27-43.

59.   Costello, G.A., *Theory of Wire Rope.* 3 ed. 1997, New York: Springer-Verlag.

60.   Healey, T.J., *Material symmetry and chirality in nonlinearly elastic rods.* Mathematics And Mechanics Of Solids, 2002. **7**(4): p. 405-420.

61.   Fuller, F.B., *Writhing Number Of A Space Curve.* Proceedings Of The National Academy Of Sciences Of The United States Of America, 1971. **68**(4): p. 815-&.

62.   White, J.H., *Self-Linking And Gauss-Integral In Higher Dimensions.* American Journal Of Mathematics, 1969. **91**(3): p. 693-&.

63.   Finzi, L. and J. Gelles, *Measurement Of Lactose Repressor-Mediated Loop Formation And Breakdown In Single Dna-Molecules.* Science, 1995. **267**(5196): p. 378-380.

64.   Mehta, R.A. and J.D. Kahn, *Designed hyperstable lac repressor center dot DNA loop topologies suggest alternative loop geometries.* Journal Of Molecular Biology, 1999. **294**(1): p. 67-77.

65.   Smith, S.B., Y.J. Cui, and C. Bustamante, *Overstretching B-DNA: The elastic response of individual double-stranded and single-stranded DNA molecules.* Science, 1996. **271**(5250): p. 795-799.

66.   Yin, H., et al., *Transcription Against An Applied Force.* Science, 1995. **270**(5242): p. 1653-1657.

67.   Doi, M. and S.F. Edwards, *The theory of polymer dynamics.* The International series of monographs on physics ; 73. 1988, Oxford [Oxfordshire]

New York: Clarendon Press ;

Oxford University Press. xiii, 391.

68.   Rouse, P.E., *A Theory Of The Linear Viscoelastic Properties Of Dilute Solutions Of Coiling Polymers.* Journal Of Chemical Physics, 1953. **21**(7): p. 1272-1280.

69.   Zimm, B.H., *Dynamics Of Polymer Molecules In Dilute Solution - Viscoelasticity, Flow Birefringence And Dielectric Loss.* Journal Of Chemical Physics, 1956. **24**(2): p. 269-278.

70.   Shusterman, R., et al., *Monomer dynamics in double- and single-stranded DNA polymers.* Physical Review Letters, 2004. **92**(4).

71.   Derjaguin, B. and L. Landau, *Theory Of Stability Of Highly Charged Liophobic Sols And Adhesion Of Highly Charged Particles In Solutions Of Electrolytes.* Zhurnal Eksperimentalnoi I Teoreticheskoi Fiziki, 1945. **15**(11): p. 663-682.

72.   Larson, R.G., *The Structure and Rheology of Complex Fluids.* 1999, New York: Oxford University Press.

73.   Bhuiyan, L.B. and C.W. Outhwaite, *The Cylindrical Electric Double-Layer In The Modified Poisson-Boltzmann Theory.* Philosophical Magazine B-Physics Of Condensed Matter Statistical Mechanics Electronic Optical And Magnetic Properties, 1994. **69**(5): p. 1051-1058.

74.   Gavryushov, S. and P. Zielenkiewicz, *Electrostatic potential of B-DNA: Effect of interionic correlations.* Biophysical Journal, 1998. **75**(6): p. 2732-2742.

75.   Rybenkov, V.V., A.V. Vologodskii, and N.R. Cozzarelli, *The effect of ionic conditions on the conformations of supercoiled DNA .1. Sedimentation analysis.* Journal Of Molecular Biology, 1997. **267**(2): p. 299-311.

76.   Rybenkov, V.V., A.V. Vologodskii, and N.R. Cozzarelli, *The effect of ionic conditions on the conformations of supercoiled DNA .2. Equilibrium catenation.* Journal Of Molecular Biology, 1997. **267**(2): p. 312-323.

77.   Sottas, P.E., et al., *Brownian dynamics simulation of DNA condensation.* Biophysical Journal, 1999. **77**(4): p. 1858-1870.

Chapter 2

The Rod Model – Theoretical Formulation

2.1 Definitions and Assumptions

In the field of structural mechanics, a "rod" is a thin (1-dimensional) structural element that may undergo two-axis bending, torsion, and extension. We develop our model by employing the classical approximations of Kirchhoff/Clebsch (described in Love [1]). In particular, we assume that the cross-section of the rod remains planar and unshearable (i.e. rigid). The rigid body dynamics of each cross-section ultimately yield the dynamical theory of the rod upon proper application of the balance laws for linear and angular momentum[9]. The locus of mass centers for each cross-section constitutes the "rod centerline". For DNA, we further assume that the rod centerline coincides with the helical axis of the duplex. A comprehensive review of rational rod theories is given in the works of Antman [2].

Now consider the infinitesimal element of a Kirchhoff rod shown in Figure 2.1. The three-dimensional curve $R(s,t)$ formed by the centerline is parameterized by the arc length coordinate s and time t. The body-fixed[10] frame $\{a_i\}$ at each cross-section is employed to describe the orientation of the cross-section with respect to the inertial frame $\{e_i\}$. The angular velocity $\omega(s,t)$ of the cross-section is defined as the rotation of the body-fixed frame $\{a_i\}$ *per unit time* relative to the inertial frame $\{e_i\}$ and satisfies

---

[9] By contrast, in 'catenary' or 'string' models, we need only consider the balance of linear momentum.
[10] Attached to the rod cross-section.
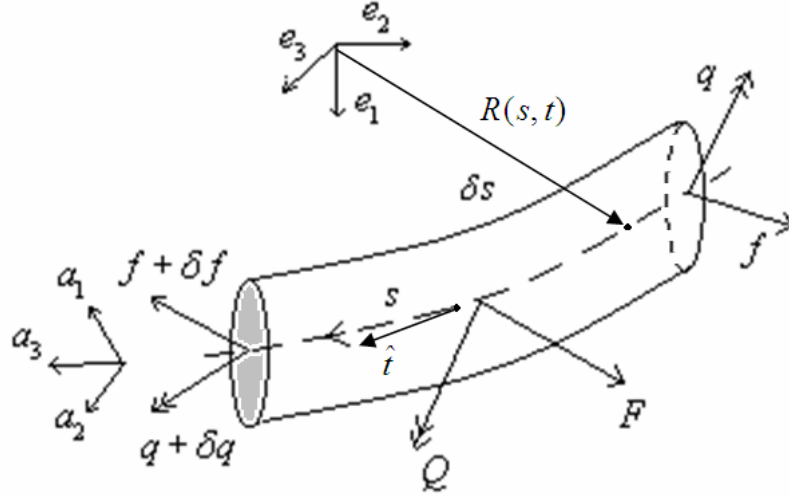
Figure 2.1 Free body diagram of an infinitesimal element of a Kirchhoff rod.

$$\left(\frac{\partial a_i}{\partial t}\right)_{\{e_i\}} = \omega \times a_i, \qquad (2.1)$$

where the subscript specifies the reference frame relative to which the derivative has been taken. We also define a 'curvature and twist vector' $\kappa(s,t)$ as the rotation of the body-fixed frame $\{a_i\}$ *per unit arc length* relative to the inertial frame $\{e_i\}$. In analogy to Eq. (2.1), the vector $\kappa(s,t)$ satisfies

$$\left(\frac{\partial a_i}{\partial s}\right)_{\{e_i\}} = \kappa \times a_i. \qquad (2.2)$$

In a stress-free state, the rod conforms to its natural geometry (with possible intrinsic curvature and twist) defined by $\kappa_0(s)$. The difference $\{\kappa(s) - \kappa_0(s)\}$ results in an (restoring) internal moment $q(s,t)$ at each cross-section of the rod. The relationship between the change in curvature/twist $\{\kappa(s) - \kappa_0(s)\}$ and the restoring moment $q(s,t)$ is governed by material properties and is called the 'constitutive law' for bending and torsion. Our rod model employs a general form of this constitutive law

$$q(s,t) = fn(\kappa(s,t) - \kappa_0(s), s, ...) .$$
(2.3)

where the function[11] *fn* is an input to the computational rod model. The rod is also assumed to be inextensible, but can sustain tension as a component of the internal force $f(s,t)$.

The deformation energy (or 'strain energy') of the rod depends on the functional form of the constitutive law *fn* and therefore we shall later specialize this for particular case studies later. The kinetic energy of the rod depends upon the centerline velocity $v(s,t)$ and the cross-section angular velocity $\omega(s,t)$. Let $m(s)$ denote the mass of the rod per unit arc length and $I(s)$ denote the tensor of principal mass moments of inertia per unit arc length. Then the kinetic energy per unit arc length is

$$K_e(s,t) = \frac{1}{2}\omega(s,t)^T I(s)\omega(s,t) + \frac{1}{2}v(s,t)^T m(s)v(s,t) .$$
(2.4)

We chose the vectors $v(s,t)$, $\omega(s,t)$, $\kappa(s,t)$ and $f(s,t)$ define four field variables. The kinematical quantities $\kappa(s,t)$, $\omega(s,t)$ and $v(s,t)$ can be integrated to compute the rod configuration, which is uniquely defined by the position vector $R(s,t)$ and the cross-section orientation given by $\{a_i(s,t)\}$. This computation will be discussed in the next Chapter along with the numerical formulation.

Depending upon the application, the rod may also interact with numerous external field forces including those produced by gravity, a surrounding fluid medium, contact with other bodies or with the rod itself, electrostatic forces, etc. (see Chapter 6 for Self-contact and Appendices 3 and 4 for other physical interactions). The resultant of these external forces and moments per unit length is denoted by $F(s,t,...)$ and $Q(s,t,...)$, respectively,

---

[11] Most of rod applications consider 'hyperelastic' behavior (pure restoring effects) for which the function *fn* is positive definite.

and these may in general be functionally-dependent on the kinematical quantities $\kappa(s,t)$, $\omega(s,t)$ and $v(s,t)$ as well as the displacement field variables.

We next derive four field equations to solve for the four vector unknowns $\{v, \omega, \kappa, f\}$. In the field equations, we will use the partial derivative of all quantities 'relative to' the body-fixed frame $\{a_i\}$. Recall that partial derivatives of any vector υ 'relative to' the body fixed frame are related to the partial derivatives 'relative to' the inertial frame through (refer to Greenwood [3])

$$\left(\frac{\partial \upsilon}{\partial t}\right)_{\{a_i\}} = \left(\frac{\partial \upsilon}{\partial t}\right)_{\{e_i\}} - \omega \times \upsilon \quad \text{and} \quad \left(\frac{\partial \upsilon}{\partial s}\right)_{\{a_i\}} = \left(\frac{\partial \upsilon}{\partial s}\right)_{\{e_i\}} - \kappa \times \upsilon, \tag{2.5}$$

where the subscript specifies the reference frame. For notational convenience, we drop the subscript for the body fixed frame from this point forward.

2.2 Equations of Motion

The balance of linear momentum of the infinitesimal element shown in Figure 2.1 becomes

$$\frac{\partial f}{\partial s} + \kappa \times f = m\left(\frac{\partial v}{\partial t} + \omega \times v\right) - F \tag{2.6}$$

and the balance of angular momentum becomes

$$\frac{\partial q}{\partial s} + \kappa \times q = I\frac{\partial \omega}{\partial t} + \omega \times I\omega + f \times \hat{t} - Q, \tag{2.7}$$

33

where $\hat{t}(s,t)$ is the unit tangent[12] vector along the centerline and the internal moment $q(s,t)$ shall be substituted by $fn\big(\kappa(s,t)-\kappa_0(s)\big)$ according to the constitutive law (2.3).

2.3 Constraints and Summary

The above formulation is completed with the addition of two constraints. The first enforces *inextensibility* and *unshearability* constraints which takes the form

$$\frac{\partial v}{\partial s}+\kappa\times v=\omega\times\hat{t}. \tag{2.8}$$

The second follows from continuity requirements for ω and κ in the form of the *compatibility* constraint

$$\frac{\partial \omega}{\partial s}+\kappa\times\omega=\frac{\partial \kappa}{\partial t}. \tag{2.9}$$

Derivations of these constraints are provided in Appendix 5.

The four vector equations (2.6-2.9) in the four vector unknowns $\{v,\omega,\kappa,f\}$ result in a 12th order system of nonlinear partial differential equations in space and time. They are compactly written as

$$M(Y,s,t)\frac{\partial Y}{\partial t}+K(Y,s,t)\frac{\partial Y}{\partial s}+\mathbb{F}(Y,s,t)=0 \tag{2.10}$$

---

[12] The tangent vector $\hat{t}$ points along the axis for torsion. Also recognize that for an unshearable rod, the tangent vector $\hat{t}$ remains constant relative to the cross-section-fixed frame $\{a_i\}$, i.e. $\left(\dfrac{\partial \hat{t}}{\partial t}\right)_{\{a_i\}}=\dfrac{\partial \hat{t}}{\partial t}=0$.

where $Y(s,t) = \{v, \omega, \kappa, f\}$. The matrices M, K and $\mathbb{F}$ are defined in Appendix 6. The equations are not integrable in closed form and necessitate a numerical search of the solution at each time step. The numerical formulation is described in the next Chapter.

References:

1. Love, A.E.H., *A Treatise on the Mathematical Theory of Elasticity*. 4 ed. 1944, New York: Dover Publications.
2. Antman, S.S., *Nonlinear Problems in Elasticity*. 2 ed. 2004, New York: Springer-Verlag.
3. Greenwood, D.T., *Principles of dynamics*. 1988, Englewood Cliffs, N.J. :: Prentice-Hall.
4. Morison, J.R., et al., *The Force Exerted By Surface Waves On Piles.* Transactions Of The American Institute Of Mining And Metallurgical Engineers, 1950. **189**: p. 149-154.
5. Howard, J., *Mechanics of Motor Proteins and the Cytoskeleton*. 2001, Sunderland: Sinauer Associates.
6. Tirado, M.M. and J. Garciadelatorre, *Translational Friction Coefficients Of Rigid, Symmetric Top Macromolecules - Application To Circular-Cylinders.* Journal Of Chemical Physics, 1979. **71**(6): p. 2581-2587.
7. Tirado, M.M. and J. Garciadelatorre, *Rotational-Dynamics Of Rigid, Symmetric Top Macromolecules - Application To Circular-Cylinders.* Journal Of Chemical Physics, 1980. **73**(4): p. 1986-1993.
8. Lamb, H., *Hydrodynamics*. 6 ed. 1945, New York: Dover Publications.
9. Nikravesh, P.E., *Computer-aided Analysis of Mechanical Systems*. 1988, Englewood cliffs: Prentice-Hall.
10. Moler, C. and C. Vanloan, *19 Dubious Ways To Compute Exponential Of A Matrix.* Siam Review, 1978. **20**(4): p. 801-836.

Chapter 3

The Rod Model – Computational Formulation

In our *dynamic* formulation, the nonlinear equations of motion are not integrable in closed form and this necessitates a numerical search of the solution at each time step. Eq. (2.10) is a 12th order system of partial differential equations in space and time. They can be solved numerically for the field variables $Y = \begin{bmatrix} v & \omega & \kappa & f \end{bmatrix}$ under specified initial and boundary conditions (six at each boundary). The generalized-α method of Chung and Hulbert [1-3] is employed for integration in both space and time, leading to a 2nd order accurate implicit finite differencing algorithm. The method is unconditionally stable and has the advantage of controllable numerical dissipation. Starting with the initial value $Y(s,0)$, the discretized equations are integrated over space at each successive time step. The boundary conditions are satisfied during spatial integration using classical shooting for boundary-value problems [4].

The deformed shape of the rod is specified by $R(s,t)$ and $\{a_i(s,t)\}$ that give the position and orientation of each cross section of the rod at any time. $R(s,t)$ and $\{a_i(s,t)\}$ can be directly integrated from the kinematical field variables $v(s,t)$, $\omega(s,t)$ and/ or $\kappa(s,t)$ at each successive time step. Standard formulations employ three Euler angles or four Euler parameters to describe the kinematics of cross-section rotation. Here, we employ 'incremental rotations' [5].

3.1 The Generalized-α Method

The accuracy and stability of a numerical method is typically evaluated for the canonical initial value problem:

$$\dot{y} = f(y,t), \ y(t_0) = y_0 \tag{3.1}$$

where $y(t)$ is function of t and $\dot{y}(t)$ is its derivative with respect to t. In the generalized-α method, the differential equation (3.1) is approximated over the integration step Δt from t_i to t_{i+1} with the difference equation

$$y^{i+1} = y^i + \Delta t\{(1-\gamma)\dot{y}^i + \gamma \dot{y}^{i+1}\} \tag{3.2}$$

where

$$\alpha \dot{y}^i + (1-\alpha)\dot{y}^{i+1} = \beta f^i + (1-\beta)f^{i+1} \tag{3.3}$$

and the superscripts i define the discretization grid point of t. The three numerical parameters α, β and γ can have different values (usually $\alpha, \beta, \gamma \in [0,1]$) to cover a wide variety of algorithms including the box method, a family of Euler's methods (including generalized trapezoidal method), HHT-α [6] and WBZ-α [7]. The generalized-α method can be optimized for stability and accuracy as summarized below.

The optimal order of accuracy for linear multiple-step methods (LMM) is two as governed by the stability restrictions according to Dahlquist's theorem [8, 9] and computational speed. The second-order accuracy for the generalized-α method requires[13]:

$$\alpha - \beta + \gamma = \frac{1}{2}. \tag{3.4}$$

The stability of any numerical algorithm can be analyzed for the linear, homogeneous and autonomous system[14]:

---

[13] To determine this condition, write Eq. (3.2) and Eq. (3.3) for two successive steps, eliminate the $\dot{y}$ terms, and expand the result in a Taylor series in Δt.

$$\dot{y} + \omega y = 0 \tag{3.5}$$

where ω is a constant in the right-half complex plane. One way of stabilizing an algorithm is to control the numerical dissipation through its "amplification matrix" A that recursively computes the solution of Eq. (3.5):

$$\begin{Bmatrix} y \\ \dot{y} \end{Bmatrix}^{i+1} = A \begin{Bmatrix} y \\ \dot{y} \end{Bmatrix}^{i} \tag{3.6}$$

For the generalized-α method,

$$A = \begin{bmatrix} 1 & -\gamma\Delta t \\ \omega(1-\beta) & 1-\alpha \end{bmatrix}^{-1} \begin{bmatrix} 1 & (1-\gamma)\Delta t \\ -\omega\beta & -\alpha \end{bmatrix} \tag{3.7}$$

The growth or decay of the numerical solution is governed by the eigenvalues $\lambda_{1,2}$ of A. An algorithm is said to be "unconditionally stable" or "A-stable" or "absolutely stable" if $\forall \omega\Delta t, |\lambda_{1,2}| \le 1$. For generalized-α method, this condition is satisfied if

$$\alpha, \beta \le \frac{1}{2} \le \gamma \tag{3.8}$$

It is further recommended in [1] to control the dissipation of high-frequency noise by letting $\max|\lambda_{1,2}|$ decrease monotonically as $|\omega\Delta t| \to \infty$. Considering only real $\omega\Delta t$, this requirement reduces the generalized-α method into a single parameter method as follows [2]. The eigenvalues start off being real at $\omega\Delta t = 0$ (the eigenvalues are $\lambda_{1,2}^0 = \left\{ \frac{\alpha}{\alpha-1}, 1 \right\}$),

---

[14] The stability of an algorithm for Eq.(A6.5) is a necessary (but not sufficient) condition for its stability for Eq. (A6.1).

become complex conjugates beyond some $\omega\Delta t$ and become real again for large $\omega\Delta t$. In the limit $\omega\Delta t \to \infty$, the eigenvalues become

$$\lambda_{1,2}^{\infty} = \left\{ \frac{\beta}{\beta-1}, \frac{\gamma-1}{\gamma} \right\} \tag{3.9}$$

The best possibility of monotonic decrease in $\max|\lambda_{1,2}|$ exists when the second bifurcation of eigenvalues (from complex conjugates to real) is prevented [2]. The second bifurcation is prevented by imposing $\lambda_1^{\infty} = \lambda_2^{\infty} = \lambda^{\infty}$ (which sets the bifurcation to occur at infinite $\omega\Delta t$). From Eq. (3.9),

$$\beta = \frac{\lambda^{\infty}}{\lambda^{\infty}-1}, \gamma = \frac{1}{1-\lambda^{\infty}} \tag{3.10}$$

Substituting (3.10) in the condition of second-order accuracy (3.4),

$$\alpha = \frac{3\lambda^{\infty}+1}{2\lambda^{\infty}-2} \tag{3.11}$$

Thus the set of equations (3.10) and (3.11) parameterizes the generalized-α method on λ^{∞} that governs the high frequency dissipation. Usually λ^{∞} is chosen to be negative ($\lambda^{\infty} \in [-1,0]$) so that $\alpha, \beta, \gamma \in [0,1]$.

3.2 Space-Time Discretization

Following the work of Gobat and Grosenbaugh [2], we discretize by finite differencing and make reference to the space-time discretization grid shown in Figure 3.1. We denote spatial derivatives by a superscript prime and temporal derivatives by a superscript dot.
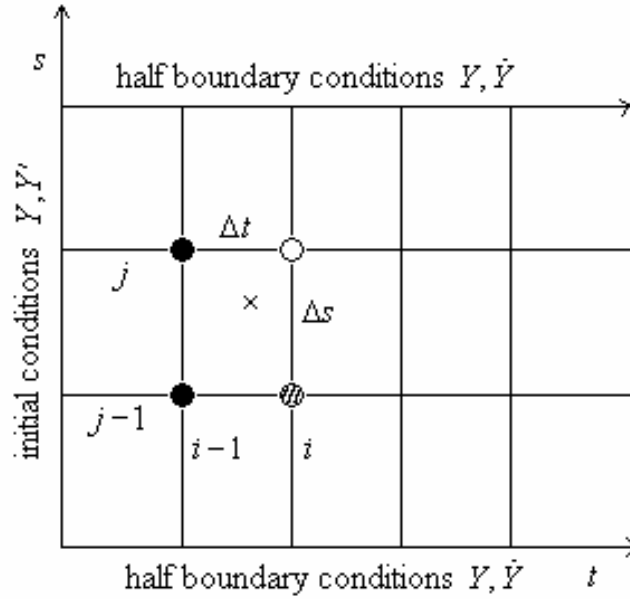
Figure 3.1 Space-time disretization grid (Method of Lines)

For a three-dimensional configuration, the dimension of Y is 12. In order to solve the set of first-order nonlinear partial differential equations Eq. (2.10), we must also specify

1. $Y(s,0)$ as the initial conditions (initial configuration of the rod and its initial velocity and angular velocity), and

2. six components of $Y(0,t)$ with six of $Y(L,t)$ as the boundary conditions. In general, the boundary conditions may be implicit and nonlinear, e.g. $\Phi(Y, \frac{\partial Y}{\partial t}, t) = 0$, which would then require numerical solution together with the partial differential equations, Eq. (2.10).

Starting with initial conditions, and for each successive time step, we integrate along s and use the shooting method to satisfy all boundary conditions at the two ends. Thus, to solve for Y at the open node (i,j) in Figure 3.1, we use the known solution Y at the two shaded nodes $(i-1,j)$ and $(i-1,j-1)$ known from the prior time step, as well as the solution Y at the partially shaded-circle node (current time step, prior spatial step, $(i,j-1)$) as described next. All (spatial and temporal) derivatives are formed using the Generalized-α method described below.

41

We begin with Y and Y' known from the initial conditions ($t=0$), and then compute the initial value of $\dot{Y}$ from the governing equations. Observe that M is always a singular matrix (no time derivative appears in the constraint equation Eq. (2.8)). K is always non-singular (but for a very flexible cable, it may become ill-conditioned). Though M is singular, to evaluate $\dot{Y}$, we simplify by choosing $\dot{f}=0$ to start with, as there is no dependence on $\dot{f}$ in the governing equations. Also, any initial condition must satisfy

$$\frac{\partial \dot{v}}{\partial s} + \dot{\kappa} \times v + \kappa \times \dot{v} = \dot{\omega} \times \hat{t} , \tag{3.12}$$

which is the time-derivative of the inextensibility and unshearability constraint Eq. (2.8).

Finite differencing of the set of governing equations Eq. (2.10) in time is achieved using the Generalized-α method, whose advantages in this application are discussed in Gobat et al. [3],

$$M^{1-\alpha_t}\dot{Y}^{1-\alpha_t} + K^{1-\beta_t}Y'^{1-\beta_t} + F^{1-\beta_t} = 0 , \tag{3.13}$$

where we followed the notation

$$()^{1-x} = (1-x)()_i + x()_{i-1} . \tag{3.14}$$

Here α_t is introduced as a "mass-averaging" numerical parameter while β_t is a "stiffness-averaging" numerical parameter. The subscript t indicate that the averaging is done with respect to time as explained in Eq. (3.14) for x = either α_t or β_t. For simplicity and succinctness, here we continue the derivation for the case of uniform and constant M and K, and thus do not account for their averaging in the difference equation.

The solution is known at the previous time step ($i-1$) (see shaded nodes in Figure 3.1) and we move these terms to the right-hand side of Eq. (3.13) in creating the known 'non-homogeneous' term[15] H. Subsequent finite differencing in space yields,

$$(1-\alpha_t)M\dot{Y}_i^{1-\alpha_s} + (1-\beta_t)(KY_i'^{1-\beta_s} + F_i^{1-\beta_s}) = H ,$$ (3.15)

where the right-hand side

$$-H = \alpha_t M\dot{Y}_{i-1}^{1-\alpha_s} + \beta_t(KY_{i-1}'^{1-\beta_s} + F_{i-1}^{1-\beta_s})$$ (3.16)

is known, and where

$$()^{1-x} = (1-x)()_j + x()_{j-1} .$$ (3.17)

For the temporal and spatial derivatives, we employ the Newmark-like formulations,

$$\dot{Y}_i = \frac{Y_i - Y_{i-1}}{\gamma_t \Delta t} - \frac{1-\gamma_t}{\gamma_t}\dot{Y}_{i-1} ,$$ (3.18)

$$Y_j' = \frac{Y_j - Y_{j-1}}{\gamma_s \Delta s} - \frac{1-\gamma_s}{\gamma_s}Y_{j-1}' .$$ (3.19)

The Newmark constants γ_t and γ_s are numerical parameters that control the averaging of time and space derivatives. A Newmark-like method for time integration was used by Sun [10] for cable dynamics simulations. In the Generalized-α method, the numerical

---

[15] The term 'non-homogeneous' shouldn't be confused with 'material non-homogeneity'. This term is used here in the context of 'linear homogeneous differential equations'.

parameters ($\{\alpha_t, \beta_t, \gamma_t\}$ or $\{\alpha_s, \beta_s, \gamma_s\}$) are selected to satisfy optimal numerical accuracy and stability in space or time as described in Section 3.1 above.

Upon substituting Eq. (3.18) and Eq. (3.19) into Eq.(3.15), and consolidating all nonhomogeneous terms into H, we arrive at the algebraic equations

$$\hat{K}Y'_{i,j-1} + A(Y_{i,j}) = B(Y_{i,j-1}) + H , \qquad (3.20)$$

that are linear in Y' and nonlinear in Y. From here forward, we drop the subscript i for notational simplicity. Starting from a guessed solution Y^*, we form $\dot{Y}^*$ from the Newmark algorithm Eq. (3.19) and then form Y'^* using the governing equations Eq. (2.10). Here, the superscript * will indicate a quantity that depends on the guessed solution and that is also updated as the algorithm proceeds. Linearizing A and B about the guessed solution Y^* leads to the approximation to Eq. (3.20)

$$\hat{K}(Y'_{j-1})^* + R^* + A_y^* Y_j = S^* + B_y^* Y_{j-1} + H , \qquad (3.21)$$

which further reduces to

$$A_y^* Y_j = B_y^* Y_{j-1} + H^* \qquad (3.22)$$

after consolidating all nonhomogeneous terms in H^*.

This linear nonhomogeneous algebraic equation is now employed to integrate over space. Starting from $s = 0$, we apply the shooting method as discussed in Gatti and Perkins [4]. In short, we assume that Y at any s belongs to an affine solution space. With the known boundary conditions at $s = 0$, we find a basis of the solution space at $s = 0$. Then, we determine how the solution space (the chosen basis) transforms through to other end according to Eq. (3.22). Finally, we fix the linear combination of the basis vectors to satisfy the terminal boundary conditions in arriving at an updated solution at all s as our

next guess. We then update the coefficient matrices in Eq. (3.22) with the next guess and iterate this cycle until convergence is achieved.

3.3 Kinematics of Cross-Section Rotation

The solution algorithm reviewed above provides the solution $Y(s,t) = \{v, \omega, \kappa, f\}$ as time marches forward. We then compute the position $R(s,t)$ and orientation $\{a_i(s,t)\}$ of each cross section of the rod at any time by subsequent integration of the kinematical field variables $v(s,t)$, $\omega(s,t)$ and $\kappa(s,t)$. For $R(s,t)$, we integrate either $\left(\dfrac{\partial R}{\partial t}\right)_{\{e_i\}} = v$ or

$\left(\dfrac{\partial R}{\partial s}\right)_{\{e_i\}} = \hat{t}$. For $\{a_i(s,t)\}$, we integrate either $\left(\dfrac{\partial a_i}{\partial t}\right)_{\{e_i\}} = \omega \times a_i$ or $\left(\dfrac{\partial a_i}{\partial s}\right)_{\{e_i\}} = \kappa \times a_i$.

For the kinematics of cross-section rotation, we will now illustrate how we integrate $\{a_i(s,t)\}$ from $\left(\dfrac{\partial a_i}{\partial t}\right)_{\{e_i\}} = \omega \times a_i$.

We begin by recognizing that $\{a_i(s,t)\}$ are represented by the rows of the transformation matrix $L(s,t)$ (refer to Appendix 5). This matrix $L(s,t)$ transforms any representation of any vector from the inertial frame $\{e_i\}$ to the body fixed frame $\{a_i\}$. We derived an equivalent from of $\left(\dfrac{\partial a_i}{\partial t}\right)_{\{e_i\}} = \omega \times a_i$ in terms of $L(s,t)$ Appendix 5:

$$\left(\frac{\partial a_i}{\partial t}\right)_{\{e_i\}} = \omega \times a_i \Leftrightarrow \frac{\partial L}{\partial t} = -\widetilde{\omega} L. \qquad (3.23)$$

Where $\widetilde{\omega}$ is the skew-symmetric form of ω as defined in Appendix 7.

45

Standard formulations employ three Euler angles or four Euler parameters to construct the nine components of $L(s,t)$ and integrate Eq. (3.23) in terms of those parameters. Here, we employ 'incremental rotations' [5] to integrate Eq. (3.23). Accordingly, we compute the small change in $L(s,t)$ through the time step Δt using the small incremental rotation $\Phi(s,t,t-\Delta t)$

$$L(s,t) = \Phi(s,t,t-\Delta t)L(s,t-\Delta t). \tag{3.24}$$

The incremental rotation can be accomplished through a single rotation (about one axis) as per Euler rotation theorem [11]. Let the vector $\theta(s,t)$ represent the infinitesimal rotation vector for $\Phi(s,t,t-\Delta t)$. Then[16]

$$\omega(s,t) = \underset{\Delta t \to 0}{Lim}\frac{\theta(s,t)}{\Delta t} \quad \text{and} \quad \Phi = \exp(-\tilde{\theta}), \tag{3.25}$$

where $\tilde{\theta}$ is the skew-symmetric form of θ defined as defined in Appendix 7. The exponential of any skew-symmetric matrix $\tilde{x}$ is expanded use the rotation formula[17]

$$\exp(\tilde{x}) = \mathrm{I} + \tilde{u}\sin(|x|) + \tilde{u}^2(1-\cos(|x|)), \tag{3.26}$$

where $|x|$ is the magnitude of x, u is the unit vector along x and I is the identity matrix. Note that this computation employs only a scalar power series and it therefore avoids the known numerical difficulties of matrix exponentiation [12].

---

[16] Eq. (3.24) and Eq. (3.25) describe the integration of Eq. (3.23). It can be derived using the Peano-Baker series which is often used to derive the 'state transition matrix' for a 'linear time-varying (LTI) system'. Eq. (3.23) has exactly the form of an LTI system and $\Phi(s,t,t-\Delta t)$ corresponds to its 'state transition matrix'.
[17] Substitute $\tilde{u}^3 = -\tilde{u}$ in Taylor expansion to verify this formula.

In short, we use (3.25) to compute $\theta(s,t)$ and $\Phi(s,t)$ and then use (3.24) to update $L(s,t)$. From the transformation matrix $L(s,t)$, we then compute the orientation of each cross section of the rod.

We can also use the computed curvature $\kappa(s,t)$ instead of angular velocity $\omega(s,t)$ to integrate $L(s,t)$ in space from $\dfrac{\partial L}{\partial s} = -\tilde{\kappa}L$ instead of in time from $\dfrac{\partial L}{\partial t} = -\tilde{\omega}L$.

3.4 Summary of Numerical Enhancements

We have improved overall computational performance in our algorithms by implementing three strategies: 1) Generalized-α method [1, 2] in both space and time, 2) a novel formulation of equations of motion that allows us to circumvent the use of Euler parameters and thereby rendering the minimum order (12th order) model, and 3) the judicious choice of field variables in terms of velocities, angular velocities and curvature/twist components (instead of displacements and Euler angles).

References:

1. Chung, J. and G.M. Hulbert, *A Time Integration Algorithm For Structural Dynamics With Improved Numerical Dissipation - The Generalized-Alpha Method.* Journal Of Applied Mechanics-Transactions Of The Asme, 1993. **60**(2): p. 371-375.

2. Gobat, J.I. and M.A. Grosenbaugh, *Application of the generalized-alpha method to the time integration of the cable dynamics equations.* Computer Methods In Applied Mechanics And Engineering, 2001. **190**(37-38): p. 4817-4829.

3. Gobat, J.I., M.A. Grosenbaugh, and M.S. Triantafyllou, *Generalized-alpha time integration solutions for hanging chain dynamics.* Journal Of Engineering Mechanics-Asce, 2002. **128**(6): p. 677-687.

4. Gatti-Bono, C. and N.C. Perkins, *Physical and numerical modelling of the dynamic behavior of a fly line.* Journal Of Sound And Vibration, 2002. **255**(3): p. 555-577.

5. Bottasso, C.L. and M. Borri, *Integrating finite rotations.* Computer Methods In Applied Mechanics And Engineering, 1998. **164**(3-4): p. 307-331.

6. Hilber, H.M., T.J.R. Hughes, and R.L. Taylor, *Improved Numerical Dissipation For Time Integration Algorithms In Structural Dynamics.* Earthquake Engineering & Structural Dynamics, 1977. **5**(3): p. 283-292.

7. Wood, W.L., M. Bossak, and O.C. Zienkiewicz, *An Alpha-Modification Of Newmark Method.* International Journal For Numerical Methods In Engineering, 1980. **15**(10): p. 1562-1566.

8. Dahlquist, G., *A special stability problem for linear multistep methods.* BIT, 1963. **3**: p. 27-43.

9. Griffith, R. and M. Nakhla. *A new high-order absolutely-stable explicit numerical integration algorithm for the time-domain simulation of nonlinear circuits.* in *Proceedings of the 1997 IEEE/ACM international conference on Computer-aided design.* 1997. San Jose, California, United States: IEEE Computer Society.

10. Sun, Y. and J.W. Leonard, *Dynamics of ocean cables with local low-tension regions.* Ocean Engineering, 1998. **25**(6): p. 443-463.

11. Nikravesh, P.E., *Computer-aided Analysis of Mechanical Systems.* 1988, Englewood cliffs: Prentice-Hall.

12. Moler, C. and C. Vanloan, *19 Dubious Ways To Compute Exponential Of A Matrix.* Siam Review, 1978. **20**(4): p. 801-836.

Chapter 4

Benchmarking and Extensions of Prior Studies: Equilibria and Dynamic Transitions

The objectives of this chapter are to

1. validate computed results from the *dynamic* rod model with published results on nonlinear rod *equilibria*,

2. highlight the advantages of the *dynamic* formulation over previous *static* (equilibrium) formulations, and

3. demonstrate the existence of dynamic transitions between coexisting nonlinear equilibria.

For the purpose of benchmarking, we refer to Heijden et al. [1] who catalogue the nonlinear equilibria and bifurcations of clamped-clamped rods under specified twist and compression as illustrated in Figure 4.1. A major strength of their work is that they have also validated their numerical computations of equilibrium rod theory with laboratory-scale experiments on a metal alloy (nitinol) rod.

We shall show that our dynamic formulation faithfully reproduces the equilibrium solutions of Heijden et al. [1] upon considering slow (i.e., quasi-static) loading. In doing so, we also discover large 'dynamic transitions' between co-existing equilibria which are, of course, impossible to capture by equilibrium rod theory alone. In our dynamic formulation, we initiate dynamic transitions by perturbing the rod with a small-amplitude

random flow field. Finally, as we simulate the same problem under faster loading, we observe hysteresis (*dynamic* lag[18]) in the neighborhood of equilibrium bifurcations.

Figure 4.1 Benchmark problem: a twisted and clamped rod. The ends have prescribed twist and separation.

4.1 Input Parameters

4.1.1 Constitutive Law

We consider a linear elastic constitutive law relating the internal moments to the curvature and twist

$$q(s,t) = B(s)(\kappa(s,t) - \kappa_0(s)) \qquad (4.1)$$

where $B(s)$ is a (positive definite) stiffness tensor. The resulting strain energy density (per unit arc length) becomes

---

[18] Dynamic lag could be dominated by inertia (as in high Reynolds number applications like underwater cables) or by viscosity (as in low Reynolds number applications like DNA in-aqueo).

$$S_e(s,t) = \frac{1}{2}(\kappa(s,t) - \kappa_0(s))^T B(s)(\kappa(s,t) - \kappa_0(s)). \tag{4.2}$$

We employ a diagonalized representation of $B(s)$ in the body fixed frame $\{a_i\}$, by choosing $\{a_i\}$ to coincide with the 'principal torsion-flexure axes' of the cross-section (defined in Love [2]). In particular, a_1 and a_2 are in the plane of the cross-section and are aligned with the principal flexure axes while a_3 is normal to the cross-section and coincides with the unit tangent $\hat{t}$ (directed towards increasing arc length). Expressed in this reference frame, both the stiffness tensor $B(s)$ and the inertia tensor $I(s)$ are diagonal. For example, $B(s)$ reduces to

$$B(s) = \begin{bmatrix} A_1(s) & 0 & 0 \\ 0 & A_2(s) & 0 \\ 0 & 0 & C(s) \end{bmatrix}, \tag{4.3}$$

where $A_1(s)$ and $A_2(s)$ are bending stiffnesses about the principal flexure axes along a_1 and a_2 respectively (possibly non-homogeneous and/or anisotropic), and $C(s)$ is the torsional stiffness (about principal torsional or 'tangent' axis' a_3).

For benchmarking with the study by Heijden et al. [1], the rod is now modeled as homogenous and isotropic ($A_1(s) = A_2(s) = A$) with no intrinsic curvature ($\kappa_0(s) = 0$). The bending to torsional stiffness ratio[19] is selected to be $A/C = 1.4$.

---

[19] The results depend on this ratio, but not independently on the bending and torsional stiffnesses. In other words, the dimensionless parameter A/C is an independent 'Π term' when Buckingham's Π theorem is applied to the rod model.

4.1.2 Distributed Loading

In Heijden et al. [1], the rod is assumed to have no distributed forces or moments ($F = 0$ and $Q = 0$). However, in our dynamic formulation, we include drag as the means to incorporate dissipation and also as a means to introduce a random disturbance through a minute random superimposed flow. The bifurcations that govern stability in these examples are triggered numerically upon the addition of these random disturbances. We add these disturbances by introducing a minute random far-field flow v_f that generates drag on the rod as per Morison's formulation [3] described in Appendix 4. The normal (form) drag and tangential (skin friction) drag coefficients are specified in

Table 4.1 along with other geometric, material and simulation parameters. The random flow velocity v_f is introduced at each temporal and spatial step through a standard random number generator in the interval $[-0.5,+0.5]\times10^{-5}$ m/s.

Table 4.1 Rod and Simulation Parameters

Quantity	Units (SI)	Value
Rod Diameter D	m	1.0×10^{-3}
Rod Length L_c	m	1.0×10^{0}
Bending Stiffness A	N-m^2	$\dfrac{1.4\pi}{64} \times 10^{-3}$
Torsional Stiffness C	N-m^2	$\dfrac{\pi}{64} \times 10^{-3}$
Rod Mass per unit length m	Kg/m	$\dfrac{\pi}{4} \times 10^{-3}$
Fluid Added Mass per unit length m_a	Kg/m	0.0×10^{0}
Bending Moments of Inertia per unit length I_1 and I_2 $\left(= \dfrac{1}{16}mD^2 \right)$	Kg-m	$\dfrac{\pi}{64} \times 10^{-9}$
Torsional Moment of Inertia per unit length I_3 $\left(= \dfrac{1}{8}mD^2 \right)$	Kg-m	$\dfrac{\pi}{32} \times 10^{-9}$
Fluid Density ρ_f	Kg/m^3	1.0×10^{0}
Normal Drag Coefficient C_n	-	1.0×10^{-1}
Tangential Drag Coefficient C_t	-	1.0×10^{-2}
Slow loading Rate $\left| \dot{d} \right|$	m/s	5.0×10^{-3}
Fast loading Rate $\left| \dot{d} \right|$	m/s	5.0×10^{-2}
Temporal Step Δt	s	1.0×10^{-1}
Spatial Step Δs	m	1.0×10^{-2}

4.1.3 Initial and Boundary Conditions

In Heijden et al. [1], the rod is clamped at both ends and is subject to specified twist and compression as illustrated in Figure 4.1. The rod of Figure 4.1 has a specified number of complete twists R when straight. This number of twists is also referred to as the 'end rotation' in Heijden et al. [1]. This equilibrium configuration is chosen as the initial condition for all subsequent simulations. Both ends are then clamped. One clamp is then

moved towards the other through a distance $d(t)$ normalized by the rod arc length L_c.

The quantity d is referred to as the 'end shortening' in Heijden et al. [1], and it increases from $d = 0$ for the initially straight rod, through $d = 1$ when the two ends meet, to the limit $d \to 2$ when the two ends cross and the rod is pulled straight (with infinite curvature at the boundaries). In the absence of self-contact, the clamped ends may pass by each other during this process.

At slow (quasi-static) loading rates, $\dot{d} \to 0$ and our solutions converge to steady-state solutions.

Table 4.1 lists the loading rate along with the other parameters that were used to obtain the following results. We compute the end tension (referred to as the 'rig force' in Heijden et al. [1]) using

$$P(t) = \frac{\left(f(0,t) \cdot \hat{t}(0,t)\right)L_c^{\;2}}{4\pi^2 A} \tag{4.4}$$

which is normalized by the fundamental Euler buckling load $\dfrac{4\pi^2 A}{L_c^{\;2}}$. As the ends very slowly approach each other, the rod initially buckles in its fundamental buckling mode as expected. The end tension and torque required to initiate buckling (of a twisted clamped rod) was first derived by Zachmann [4] as the buckling condition

$$\cos\left(\pi\sqrt{T^2 - 4P}\right) - \cos(\pi T) = \frac{2\pi P \sin\left(\pi\sqrt{T^2 - 4P}\right)}{\sqrt{T^2 - 4P}}, \tag{4.5}$$

Here, T is the (normalized) end torque that is referred to as the 'rig moment' in Heijden et al. [1]

$$T(t) = \frac{\left(q(0,t) \cdot \hat{t}(0,t)\right)L_c}{2\pi A}. \tag{4.6}$$

4.2 Equilibria Benchmarking (Slow Loading $\dot{d} \to 0$)

56

4.2.1 Case 1: $R = 0$, Planar buckling
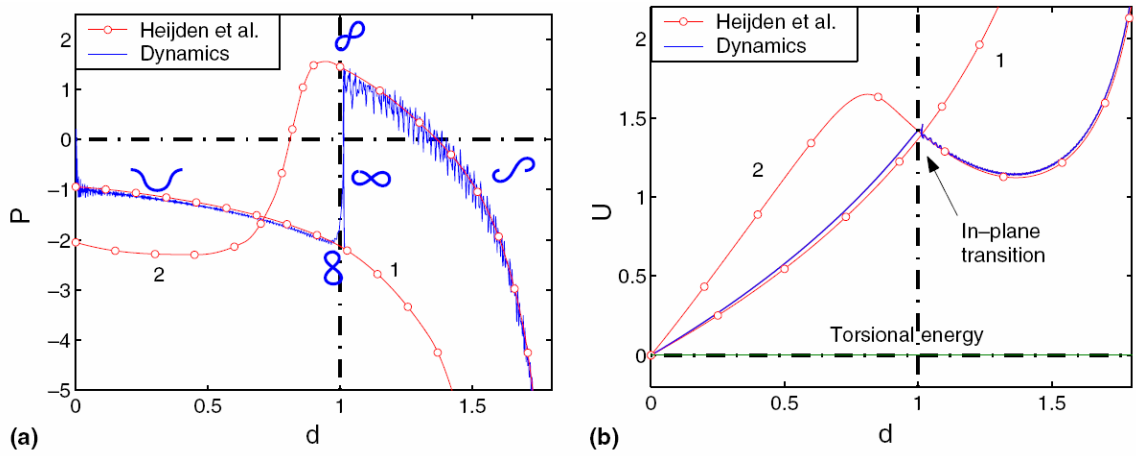
Figure 4.2 Planar buckling at quasi-static rates ($R = 0$, $\dot{d} \rightarrow 0$). The end tension (a) P and the strain energy (b) U are plotted as functions of the end shortening d. The (red) curves labeled 1 and 2 replicate solutions from Heijden et al. [1] for the first and second buckling modes, respectively. The dark gray (or blue) curve represents the (quasi-static) solution from the dynamic model.

We begin with the simplest case of a straight rod with no initial twist ($R = 0$) and evaluate its response to quasi-static compression as the end shortening increases at a very slow rate ($\dot{d} \rightarrow 0$). To initiate and to maintain buckling in one plane, we add a very small random fluid flow in the plane which loads the rod through hydrodynamic drag as detailed in Section 4.1.2 above. The computed end tension is plotted in Figure 4.2(a) as a function of the end shortening d for the dynamic formulation presented herein (blue curve). This dynamic solution converges to the equilibrium solutions reported in Heijden et al. [1] (red curves) for this quasi-static loading rate *($\dot{d} \rightarrow 0$)*. The curves labeled 1 and 2 designate equilibrium solutions for the first and second buckling modes, respectively. Starting at $d = 0$, the dynamic solution follows the equilibrium solution for the fundamental mode and at $d = 1$ undergoes a large *dynamic* transition to the solution for

57

the second mode. This transition results as the second mode becomes more energetically

favorable (lower strain energy) for $d > 1$.

This fact is illustrated in Figure 4.2(b) where the strain energy is plotted as a function of

end shortening. For these planar equilibria, the strain energy develops solely from

bending (no torsion) as computed from the strain energy density Eq. (4.2):

$$U(t) = \frac{L_c}{4\pi^2 A} \int_0^{L_c} S_e(s,t) ds .$$

(4.7)

The strain energy for the equilibrium solutions (red curves) is computed from the work

done at the boundary using the known end tension from Heijden et al. [1] and by noting

$$P = -\frac{\partial U}{\partial d} .$$

(4.8)

The dynamic solution tracks the strain energy for the fundamental buckling mode for

$d < 1$ and then for the second buckling mode for $d > 1$.
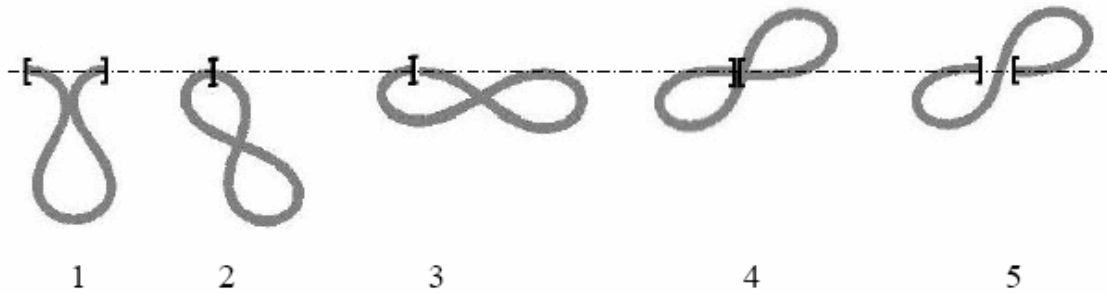
Figure 4.3 Dynamic transition from first buckling mode (snapshot 1) to second buckling mode (snapshot 5) through a series of figure eight configurations. The non-equilibrium shapes (snapshots 2-4) correspond to the dynamic transition path in Figure 4.2(a).

During this transition, the rod forms the sequence of figure eight configurations shown in Figure 4.3 as computed by the *dynamic*[20] formulation herein. This figure eight transition was first reported by Domokos [5]. Note that the clamped ends start at the apex of the figure eight (snapshot 2) and ultimately transition to the intersection of the figure eight (snapshot 4). The same transition is reproduced upon decreasing *d* without any hysteresis that becomes noticeable at faster loading rates as discussed in Section 4.3.

4.2.2 Case 2: $R = 0$, Spatial buckling

We now re-evaluate the above example upon the addition of a small three-dimensional random disturbance that initiates an out-of-plane instability; refer to Section 4.1.2. In particular, the planar equilibria now become unstable beyond a critical end shortening and bifurcate into stable spatial (three-dimensional) equilibria (Heijden et al. [1]).

---

[20] Note that the transition figure eight configurations are not *equilibrium* states, the represent a highly *dynamic* transition that cannot be captured using equilibrium theory alone.
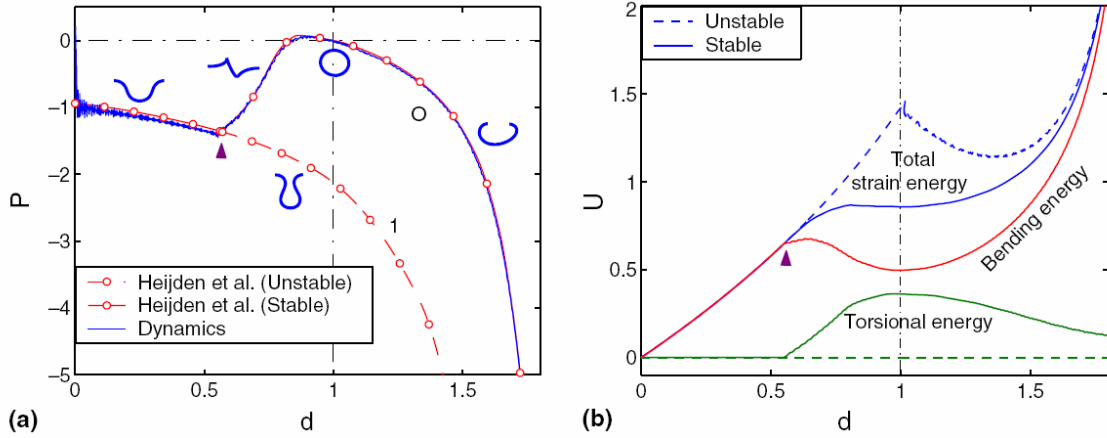
Figure 4.4 Spatial buckling at quasi-static rates ($R = 0$, $\dot{d} \to 0$). The end tension (a) P and the strain energy (b) U are plotted as functions of the end shortening d. The (red) curves labeled 1 and O replicate equilibrium solutions from Heijden et al. [1] and the solid (dashed) curve represents stable (unstable) equilibria. The out of plane bifurcation point is denoted by the triangle. The strain energy U (blue) is the sum of torsional (green) and bending (red) strain energies.

The end tension computed in Heijden et al. [1] is recovered for the quasi-static loading rates in this example as reported in Figure 4.4(a) (red curve). The rod now buckles out of plane (follow blue curve) well before reaching a figure eight configuration. This bifurcation is denoted by the triangle in Figure 4.4 which locates where the fundamental in plane mode loses stability and a stable spatial buckling mode is born. In addition, the rod deforms into a circular loop with one complete twist at $d = 1$ as bending strain energy (red curve) is exchanged for torsional strain energy (green curve) in Figure 4.4(b). In fact, there is a marked decrease in bending energy accompanied by a large increase in torsional energy just beyond the bifurcation point which initiates the out of plane deformation.

4.2.3 Case 3: $|R| = 1$ Planar and spatial buckling

60
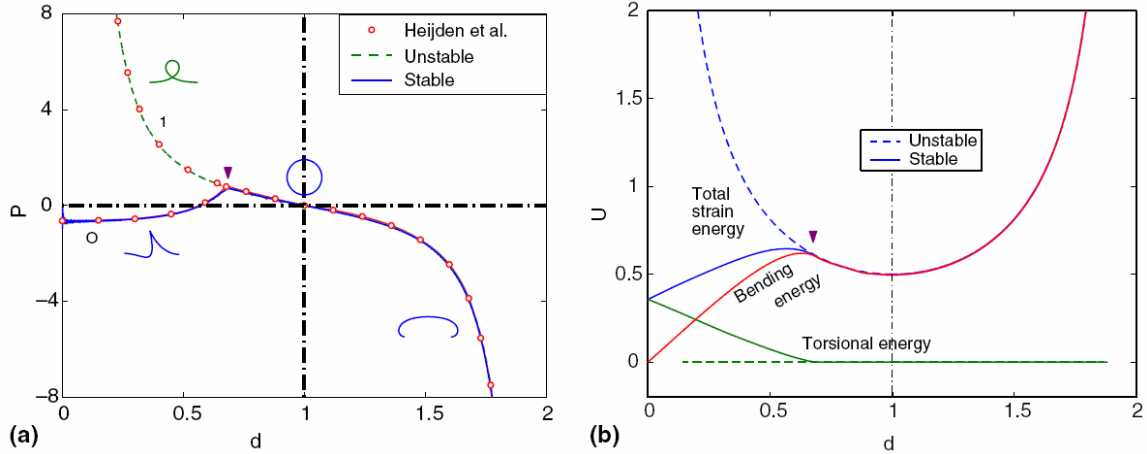
Figure 4.5 Effect of initial twist on the spatial and planar buckling at quasi-static rates ($R = 1$, $\dot{d} \to 0$). The end tension (a) P and the strain energy (b) U are plotted as functions of the end shortening d. The curves labeled 1 and O replicate equilibrium solutions from Heijden et al. [1] and the solid (dashed) curve represents stable (unstable) equilibria. The bifurcation point is denoted by the triangle. The strain energy U (blue) is the sum of torsional (green) and bending (red) strain energies.

The calculations above are now repeated after first pre-twisting the rod by introducing one complete end rotation when the rod is straight, i.e. $|R| = 1$. The end tension for both planar and spatial equilibria (Heijden et al. [1]) is recovered for the quasi-static loading rate used in this example; refer to Figure 4.5(a). Starting from $d = 0$, the rod first buckles as per Eq. (2.5) in its fundamental mode which resembles a helix with small helical diameter (Zachman [4]). The helical diameter increases with d and the spatial equilibrium ultimately becomes planar with an interior loop at the bifurcation point (denoted by the triangle). At this bifurcation, the out of plane solution branch denoted by O joins the fundamental in plane solution branch denoted by 1. As d is increased further, the now planar loop increases in diameter, and at $d = 1$, the rod conforms to a circular loop (without twist). This loop becomes flattened for $d > 1$ and remains planar as it approaches the limit $d \to 2$ at which point the rod is again straight with infinite

curvature at its extremities.   If the process is reversed (i.e., d is now slowly decreased

from 2), the planar loop becomes unstable at the bifurcation and exhibits a 'pop out'

instability (as noted by Coyne [6]) when subjected to minute three-dimensional

excitation. Figure 4.5(b) shows that the strain energy (and its decomposition into

torsional and bending components) for the solutions of Figure 4.5(a). Starting with the

straight and twisted rod ($d = 0$), the strain energy develops purely from torsion. Upon

buckling, the torsional strain energy is reduced while the bending strain energy is

increased and a net increase in strain energy results as the spatial equilibria evolve

(d increases). At the bifurcation point, the strain energy of the spatial equilibrium

achieves that of the planar equilibrium and beyond that point only the planar solution

exists.

It should also be noted in Figure 4.5(b) that the circular loop ($d = 1$) achieves the

minimum strain energy beyond the bifurcation point. This coincides with the fact all

circular loops with twist less than a critical value ($|\mathcal{R}| < \sqrt{3}\dfrac{A}{C}$) are stable (Heijden et al.

[1]). This critical value was first reported by Zajac [7] in the context of cable dynamics

and later on independently reported in the context of DNA plasmids (closed loop DNA)

by Le Bret [8] and Benham [9]. Above this critical value, the circular loop buckles into a

figure eight (with subsequent intertwining) as simulated dynamically by Klapper [10] in

the context of biological filaments.

4.3 Dynamics and Hysteresis (Fast Loading - Finite $\dot{d}$)

The results above confirm that the dynamic solutions converge to known equilibrium solutions at infinitesimal loading rates $\dot{d} \to 0$. The dynamic formulation reproduces the expected equilibrium bifurcations and dynamic transitions between equilibria are also captured. We now turn attention to cases where the loading rate is finite which introduces new dynamic effects, most notably hysteresis. In particular, as the loading rate increases, the dynamic transition from planar to spatial equilibrium forms is delayed due to *inertial* and/or *viscous* effects[21].
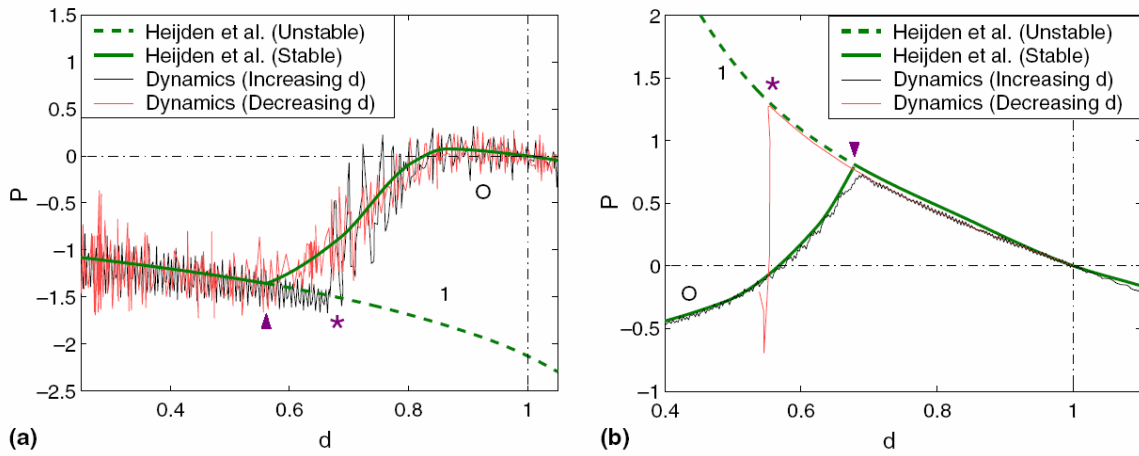
Figure 4.6 Dynamic effects of non-equilibrium loading rates ($\dot{d}$ finite). The end tension P plotted as function of end shortening d for cases of rod (a) without initial twist $R = 0$, and (b) with one complete initial twist $R = 1$. The curves labeled 1 and O replicate planar and spatial equilibrium solutions from Heijden et al. [1]. The equilibrium bifurcation point is denoted by the triangle and the delayed transition by the asterisk.

Figure 4.6(a) and Figure 4.6(b) illustrate this phenomenon for cases of an initially untwisted rod ($R = 0$) and a rod with one complete initial twist ($|R| = 1$), respectively. The loading rate $|\dot{d}| = 5 \times 10^{-2} m/s$ is sufficiently large to observe hysteresis in these

<hr>

[21] Inertial effects are predominant in high Reynolds number applications like underwater cables while viscous effects are predominant in low Reynolds number applications like DNA in-aqueo.

examples. The remaining parameters used in this example are again listed in

Table 4.1. As above, we include minute random excitation produced by a random flow field as described in Section 4.1.2.

For the initially untwisted rod, the dynamic solution closely tracks the planar equilibrium solutions as the end shortening initially increases ($\dot{d} > 0$) starting from $d = 0$; refer to black curve in Figure 4.6(a). However, near the equilibrium bifurcation point (triangle), the dynamic solutions experience a delayed jump ('pop out' instability) from the planar forms to the spatial forms as indicated by the asterisk. By contrast, when the loading rate is reversed ($\dot{d} < 0$), the dynamic solutions pass through the equilibrium bifurcation as the spatial forms transition smoothly to the planar forms; refer to light gray (or red) curve.

Figure 4.6(b) shows analogous results for the case of the pre-twisted rod previously evaluated in Figure 4.5.   As the loading rate increases ($\dot{d} > 0$), the dynamic solution closely follows the spatial form and smoothly transitions to the planar form by passing through the equilibrium bifurcation (triangle); refer to black curve. Upon reversing the loading rate ($\dot{d} < 0$), the dynamic solution experiences a significant delayed jump ('pop out' instability) from the planar to the spatial forms as indicated by the asterisk; refer to light gray (or red) curve. Increasing the loading rate increases the delay while increasing the random excitation decreases the delay, as expected.

References:

1. van der Heijden, G.H.M., et al., *Instability and self-contact phenomena in the writing of clamped rods.* International Journal Of Mechanical Sciences, 2003. **45**(1): p. 161-196.
2. Love, A.E.H., *A Treatise on the Mathematical Theory of Elasticity*. 4 ed. 1944, New York: Dover Publications.
3. Morison, J.R., et al., *The Force Exerted By Surface Waves On Piles.* Transactions Of The American Institute Of Mining And Metallurgical Engineers, 1950. **189**: p. 149-154.
4. Zachmann, D.W., *Non-Linear Analysis Of A Twisted Axially Loaded Elastic Rod.* Quarterly Of Applied Mathematics, 1979. **37**(1): p. 67-72.
5. Domokos, G., *Global Description Of Elastic Bars.* Zeitschrift Fur Angewandte Mathematik Und Mechanik, 1994. **74**(4): p. T289-T291.
6. Coyne, J., *Analysis Of The Formation And Elimination Of Loops In Twisted Cable.* Ieee Journal Of Oceanic Engineering, 1990. **15**(2): p. 72-83.
7. Zajac, E.E., *Stability of two planar loop elasticas.* Trans. ASME Ser. E. J. Appl. Mech., 1962. **29**: p. 136--142.
8. Le Bret, M., *Catastrophic variation of twist and writhing of circular DNAs with constraint?* Biopolymers, 1979. **18**(7): p. 1709-1725.
9. Benham, C.J., *Onset of writing in circular elastic polymers.* Physical Review A (General Physics), 1989. **39**(5): p. 2582-2586.
10. Klapper, I., *Biological applications of the dynamics of twisted elastic rods.* Journal Of Computational Physics, 1996. **125**(2): p. 325-337.
11. Risken, H., *The Fokker-Planck equation : methods of solution and applications.* Springer series in synergetics ; v. 18. 1989, Berlin ; New York :: Springer-Verlag.
12. Jianhua, X., W. Hongyun, and O. George, *From Continuum Fokker-Planck Models to Discrete Kinetic Models.* 2005. **89**(3): p. 1551.
13. Calladine, C.R., et al., *Understanding DNA, the Molecule and How It Works*. 3 ed. 2004, Amsterdam: Elsevier Academic Press.

Chapter 5

Tension-Torque Coupling

The helical construction of the DNA duplex and of synthetic and wire rope cables (described in Costello [1]) gives rise to a specific kind of anisotropy called 'chirality' as suggested by Healey [2]. In contrast to isotropic rods, the behavior of a chiral rod differs from that of its mirror image [2]. To distinguish it from the anisotropy in bending, Healey [2] describes chiral anisotropy as 'hemitropy'. In an isotropic rod, the torsional moment at any cross-section is proportional to twist in the rod. However, in a chiral (or 'hemitropic') rod, tension also induces a torsional moment[22] at any cross-section due to its helical construction. In terms of kinematic quantities, this is equivalent to 'twist-extension coupling' and it is this observation that is central to the paper titled "Stretching must twist DNA" by Marko [3]. Through our computations, we have discovered that this coupling also has marked influence on loop topologies and equilibrium bifurcations.

In this chapter, we add the tension-torque coupling to the linear elastic constitutive law Eq. (4.1) introduced in Chapter 4 to capture chiral effects. The impact of this coupling is highlighted through new solutions to the benchmark problem (clamped-clamped rod) illustrated in Chapter 4.

5.1 Modified Constitutive Law

From the linear elastic constitutive law Eq. (4.1) and Eq. (4.3) introduced in Chapter 4, the restoring moment along the tangent (i.e. the internal torque) is

---

[22] For marine cable applications, this motivates the need to design so-called "torque-balanced" cables by using constructions that incorporate both left-handed and right-handed helical winds.

$$q_{\hat{t}} = C\Delta\kappa_{\hat{t}}, \qquad\qquad (5.1)$$

where $\Delta\kappa_{\hat{t}} = (\kappa - \kappa_0)\cdot\hat{t}$ is change in twist and the subscript $\hat{t}$ denotes the component along the tangent $\hat{t}$, i.e. $q_{\hat{t}}$ is the internal torque. Following Costello [1], we now replace Eq. (4.1) and Eq. (4.3) with a homogenized linear constitutive law that is coupled in twist and extension

$$\begin{Bmatrix} f_{\hat{t}} \\ q_{\hat{t}} \end{Bmatrix} = \begin{bmatrix} C_1 & C_2 \\ C_3 & C_4 \end{bmatrix} \begin{Bmatrix} \varepsilon \\ \Delta\kappa_{\hat{t}} \end{Bmatrix} \qquad\qquad (5.2)$$

where $f_{\hat{t}}$ is tension. In the context of the wire rope considered in [1], ε denotes the overall extensional strain of the rope (not the individual component wires) and the constants C_i are determined by the stiffness of the component wires and the helical construction. The simple model above captures the observed fact that the component wires tend to unwind as the rope is stretched. We now translate this kinematic (twist-extension) coupling into the traction (tension-torque) coupling by eliminating ε. From the first row equation of Eq. (5.2),

$$\varepsilon = \frac{f_{\hat{t}} - C_2\Delta\kappa_{\hat{t}}}{C_1}. \qquad\qquad (5.3)$$

Substituting ε from Eq. (5.3) into the second row equation of Eq. (5.2)

$$q_{\hat{i}} = \frac{(C_1 C_4 - C_2 C_3)\Delta\kappa_{\hat{i}} + C_3 f_{\hat{i}}}{C_1}, \tag{5.4}$$

We rewrite Eq. (5.4) in compact form as

$$q_{\hat{i}} = C_6\left(\Delta\kappa_{\hat{i}} - C_5 f_{\hat{i}}\right), \tag{5.5}$$

where

$$C_5 = -\frac{C_3}{(C_1 C_4 - C_2 C_3)},$$

$$C_6 = -\frac{(C_1 C_4 - C_2 C_3)}{C_1}. \tag{5.6}$$

In contrast to the uncoupled constitutive law Eq. (5.1), the Eq. (5.5) now introduces the tension-torque coupling through the coupling factor $C_5(s)$. The coupling factor $C_5(s)$ could in general be non-homogeneous. The sign of C_5 distinguishes a right-handed ($C_5 < 0$) helical construction from a left-handed ($C_5 > 0$) helical construction.

The uncoupled constitutive law Eq. (5.1) contributes to the torsional strain energy density $\frac{1}{2}C(\Delta\kappa_{\hat{i}})^2$ (per unit length). With the coupled constitutive law Eq. (5.5), this contribution to the strain energy density is now replaced by the quadratic form of Eq. (5.2), i.e. $\frac{1}{2}\{\varepsilon \quad \Delta\kappa_{\hat{i}}\}\begin{bmatrix} C_1 & C_2 \\ C_3 & C_4 \end{bmatrix}\begin{Bmatrix} \varepsilon \\ \Delta\kappa_{\hat{i}} \end{Bmatrix}$, where ε is substituted from Eq. (5.3).

5.2 Modified Buckling Condition (Linear)

The benchmark equilibrium problem of the clamped-clamped rod described in Chapter 4 employs an isotropic constitutive law (that assumes no coupling of torsion and tension in accordance with Eq. (5.1)). Inclusion of the coupling as per Eq. (5.5) strongly influences the primary (linear) buckling condition. In order to calculate this influence, we first non-dimensionalize Eq. (5.5) and use it in a non-dimensional analysis of the benchmark problem. First, recall that $A_1(s) = A_2(s) = A$ (homogeneous and 'hemitropic' constitutive law). Comparing Eq. (5.1) with Eq. (5.5), we set $C_6 = C$. For our non-dimensionalization, a force is normalized by the Euler buckling load $\dfrac{4\pi^2 A}{L_c^2}$, torque is normalized by $\dfrac{2\pi A}{L_c}$, curvature is normalized by $\dfrac{2\pi}{L_c}$, stiffness $C_6 = C$ is normalized by A, and we denote the non-dimensional form of the coupling factor C_5 by k_c. So we re-write Eq. (5.5) in its non-dimensional form as

$$\frac{q_{\hat{i}}}{[2\pi A/L_c]} = \frac{C}{A}\left(\frac{\Delta\kappa_{\hat{i}}}{[2\pi/L_c]} - k_c\frac{f_{\hat{i}}}{[4\pi^2 A/L_c^2]}\right). \qquad (5.7)$$

To complete the non-dimensionalization, we now determine how k_c is related to C_5 by comparing Eq. (5.5) with Eq. (5.7). Note that the 2nd term $C_5 f_{\hat{i}}$ in the parentheses of Eq.

(5.5) has dimensions of curvature for which the normalization factor is $\dfrac{2\pi}{L_c}$. Therefore,

comparing it with corresponding term in Eq. (5.7),

$$\left(\frac{C_5 f_{\hat{t}}}{[2\pi/L_c]}\right) = k_c\left(\frac{f_{\hat{t}}}{\left[4\pi^2 A/L_c^{\ 2}\right]}\right). \tag{5.8}$$

Now we turn our attention to the primary buckling condition (Eq. (4.5) in Chapter 4) of a clamped-clamped rod subject to compression and torque as derived by Zachmann [4]. The clamped rod under pure compression ($R = 0$) will now immediately develop a reaction end torque $T = -k_c\dfrac{C}{A}P$. Using this result in the buckling condition Eq. (4.5) yields the critical end tension (or compression) required to initiate buckling for a chiral rod

$$\cos\left(\pi\sqrt{\left(k_c\frac{C}{A}P\right)^2 - 4P}\right) - \cos\left(\pi k_c\frac{C}{A}P\right) = \frac{2\pi P\sin\left(\pi\sqrt{\left(k_c\frac{C}{A}P\right)^2 - 4P}\right)}{\sqrt{\left(k_c\frac{C}{A}P\right)^2 - 4P}}. \tag{5.9}$$
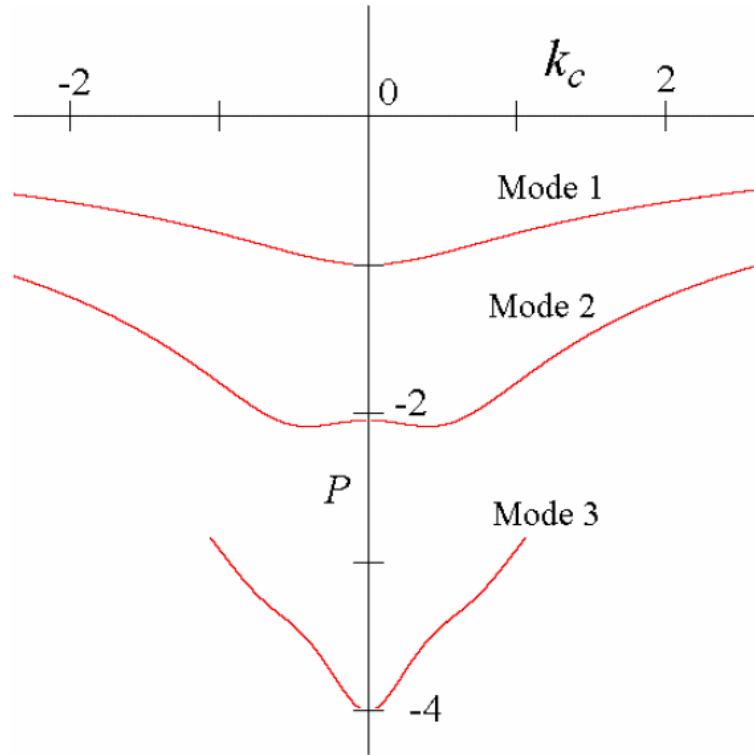
Figure 5.1 The critical end tension P **that initiates buckling as a function of the coupling factor** k_c**.**
Values for the first three modes are computed per Eq. (5.9) with $R = 0$ **and** $A/C = 1.4$ **(same ratio used in the benchmark study by Heijden et al. [5]).**

Figure 5.1 shows how this critical end tension depends upon the coupling factor k_c for the first three buckling modes. Clearly, this coupling factor has a strong influence on this bifurcation condition and the sensitivity increases with mode number.

5.3 Influence on Loop Topology and Bifurcations (Nonlinear)

Having shown the pronounced influence of the coupling on the (linear) buckling condition, we now explore its influence on post-buckling (nonlinear domain) by numerical analysis. The bifurcation diagrams for the end tension P and end torque T are shown in Figure 5.2 for various values of k_c. Without the coupling, under pure (kinematic) compression the rod initially buckles into a planar form and no torsional

72

moment develops. By contrast, with the coupling, the rod buckles in a decidedly three-dimensional from the on set of buckling due to the compression-induced torsional moment.

(a)

(b)
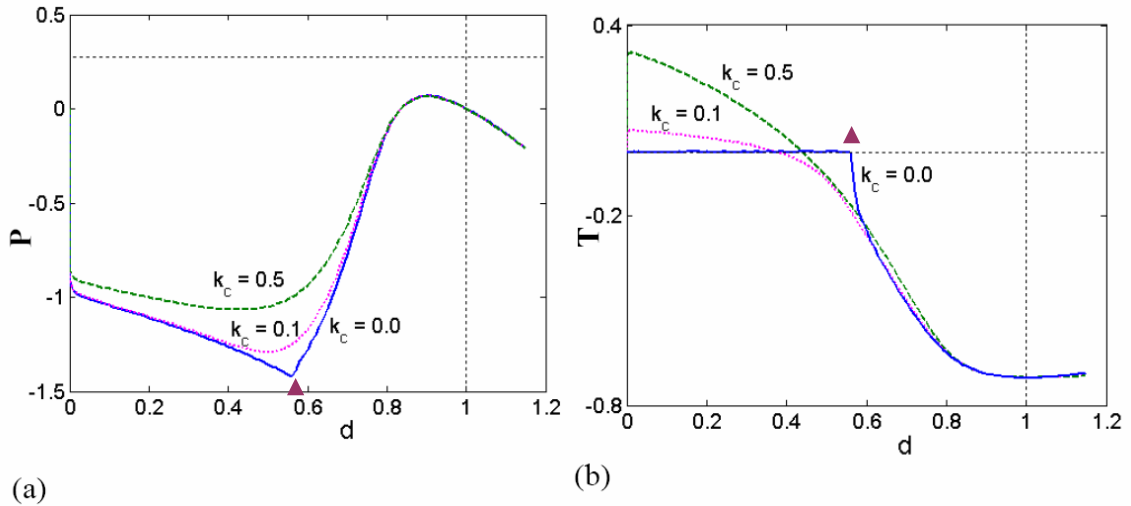
Figure 5.2 (a) End tension P and (b) end torque T plotted as the functions of end-shortening d for various values of coupling factor k_c (with $\mathbb{R} = 0$, $\dot{d} \to 0$). The blue curve ($k_c = 0$) in (a) reproduces the benchmark result of Chapter 4.

Even seemingly weak coupling has a marked influence on the shape and the stress of the rod after buckling. This sensitivity is of keen interest in DNA mechanics where long-length scale looping can regulate gene expression [6-8]. The loop orientation, twist distribution, and curvature distribution along the loop affect the availability of DNA binding sites to transcriptional proteins. The overall loop strain energy contributes to the free energy of the DNA/protein complex and thus influences the probability of loop formation. Reaction forces and torques on proteins that hold the DNA into a loop may deform the protein. All these influences may eventually affect gene regulation as will be discussed at a greater length in Chapter 7. Motivated by these issues, we will now explore

how loop properties are influenced by the coupling factor k_c for the simplest case of $R = 0$.
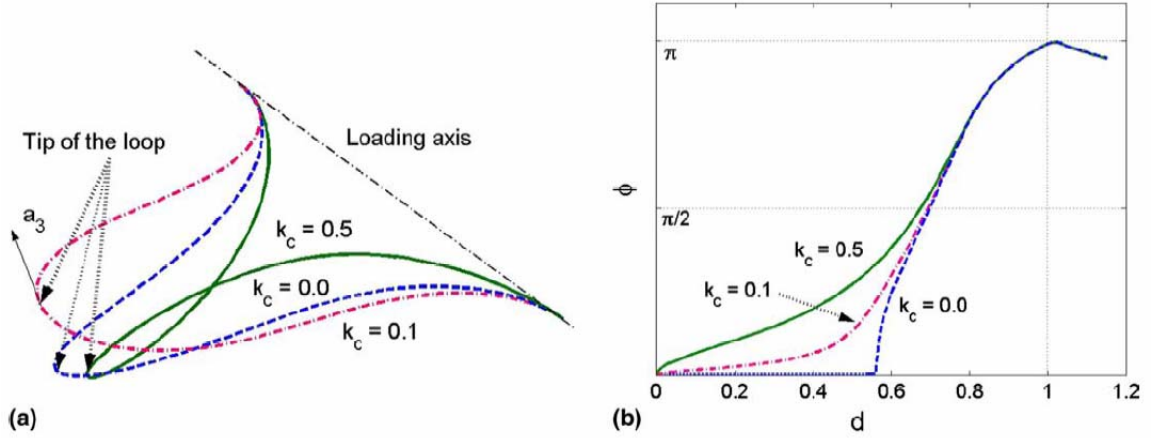
Figure 5.3 (a) Sensitivity of equilibrium loop orientations to tension-torque coupling k_c. End shortening $d = 0.5$ and initial twist $R = 0$. (b) The angle ϕ, which measures the out of plane orientation of the loop, is plotted as a function of end shortening d for three values of the coupling factor k_c.

Figure 5.3(a) shows snapshots of the loops formed both with and without tension-torque coupling for one value of end shortening $d = 0.5$ which corresponds to a state slightly before the bifurcation noted in Figure 5.2 (triangle). As the coupling factor is increased, the loop rotates significantly out of plane. To quantify this out of plane rotation, we introduce the angle ϕ between the centerline tangent $\hat{t} = a_3$ at the *tip* of the loop and the axis formed by the two ends (coincident with $a_3(0,t)$). We define the *tip* of the loop as the point farthest from the axis formed by the two ends as measured by the distance $|a_3(0,t) \times (R(s,t) - R(0,t))|$. At equilibrium, the loop will exhibit symmetry such that the tip is at the mid-span. In general, we compute the out of plane rotation at the tip using

$$\phi = \cos^{-1}\left(a_3(0,t) \cdot a_3(s_{tip}, t)\right). \tag{5.10}$$

74

Figure 5.3(b) shows the variation of ϕ as a function of end shortening d for three values of the coupling factor k_c. For the cases $k_c \neq 0$, the out of plane rotation is initiated immediately and increases rapidly with increasing end shortening, thus underscoring the sensitivity to tension-torque coupling.
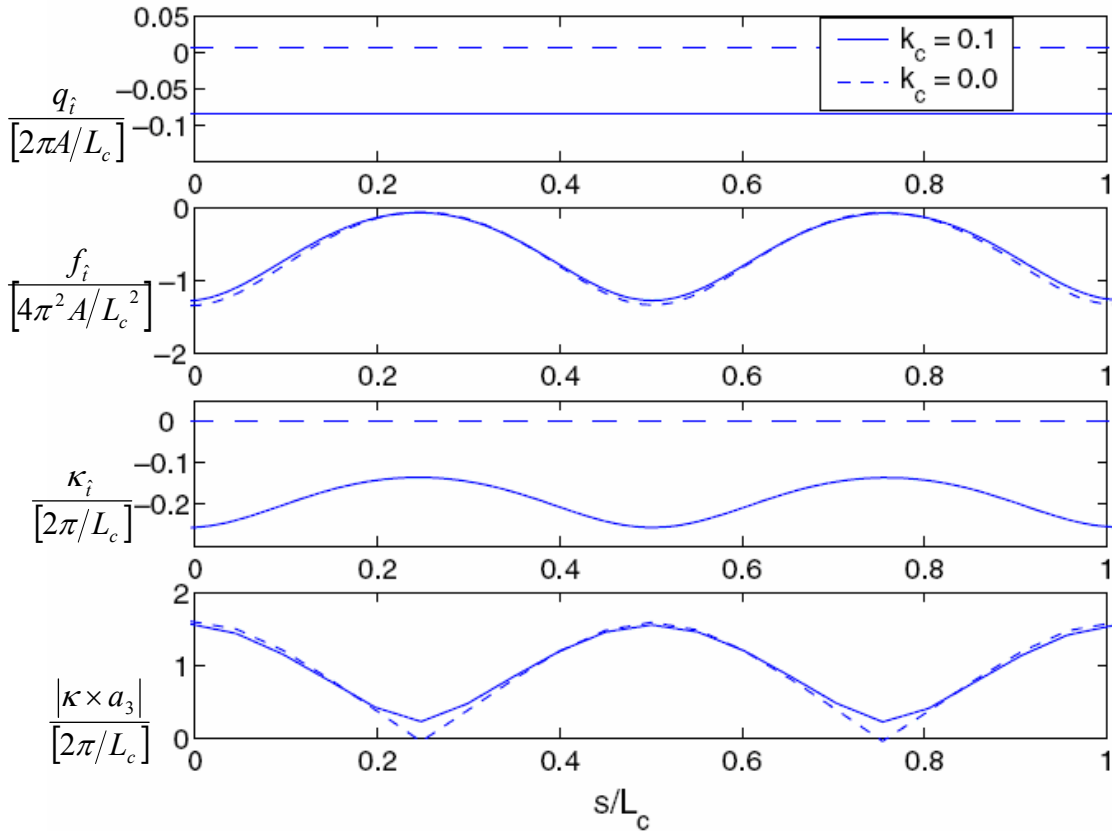
Figure 5.4 Distribution of (non-dimensional) torsional moment $q_{\hat{t}}$ **, tension** $f_{\hat{t}}$ **, twist** $\kappa_{\hat{t}}$ **and principal curvature** $|\kappa \times a_3|$ **with arc length** s **. End shortening** $d = 0.5$ **and twist** $\mathbb{R} = 0$ **.**

Figure 5.4 shows the spatial variation of the (normalized) torsional moment $q_{\hat{t}}$, tension $f_{\hat{t}}$, twist $\kappa_{\hat{t}}$, and principal curvature $|\kappa \times a_3|$ for rods with and without tension-torque coupling. In this example, the end shortening $d = 0.5$ for the two cases $k_c = 0$ and $k_c = 0.1$. The computed results for the torsional moment $q_{\hat{t}}$ confirm that this quantity remains constant (a first integral) under *equilibrium* conditions and this constant is also

non-zero when tension-torque coupling exists. The fact that the torsional moment $q_{\hat{t}}$ has to be a first integral in *equilibrium* is proven in the next paragraph. This small degree of tension-torque coupling has only a minor influence on the computed tension $f_{\hat{t}}$ and the principal curvature $|\kappa \times a_3|$, yet a pronounced influence on the computed twist $\kappa_{\hat{t}}$. The large influence on twist is responsible for the large sensitivity of loop geometry on tension-torque coupling as observed above. Moreover, the non-uniform tension results in non-uniform twist (or untwist in DNA) through the coupling effect. Non-uniform untwisting in DNA may ultimately influence the exposure of base pairs to transcriptional proteins at specific sites.

The torsional moment $q_{\hat{t}}$ has to be uniform (a first integral) in *equilibrium* for an isotropic or hemitropic rod $(A_2(s) = A_2(s))$ with no intrinsic principal curvature $(\kappa_0 \times a_3 = 0)$ and no distributed torsional moment $(Q \cdot \hat{t} = 0)$. This can be readily shown from the balance law for angular momentum Eq. (2.7) that in *equilibrium* yields

$$\frac{\partial q_3}{\partial s} + \kappa_1 q_2 - \kappa_2 q_1 = 0 . \tag{5.11}$$

where the subscripts 1, 2 and 3 denote the vector components along a_1, a_2 and a_3 respectively $(\therefore q_3 = q_{\hat{t}})$. Substituting the constitutive law for the bending moments from Eq. (4.1) and Eq. (4.2), we obtain

$$\frac{\partial q_3}{\partial s} + \left(\kappa_1 A_2(s)\kappa_2 - \kappa_2 A_1(s)\kappa_1\right) = 0 . \tag{5.12}$$

Hence, we the torsional moment $q_{\hat{t}}$ $(=q_3)$ is a first integral for an isotropic or hemitropic rod for which $A_1(s) = A_2(s)$. So the uniform torsional moment $q_{\hat{t}}$ in Figure 5.4 also corroborates the fact that our loading was 'slow enough' to enable a quasi-static solution. In an isotropic rod, uniform $q_{\hat{t}}$ also implies uniform twist (or untwist) in accordance to Eq. (5.1). However, in a hemitropic rod, the twist may become non-uniform due to non-uniform tension through the coupling effect in accordance with Eq. (5.5).

5.4 Summary of Effects of Tension-Torque Coupling

The analytical and numerical results presented in this chapter demonstrate that tension-torque coupling can have pronounced influences on the bifurcations of rod equilibria and on the mechanics of loop formation. The major influences noted in these results are that tension-torque coupling may:

1. substantially alter loop topology,
2. introduce non-uniform twist (or untwist),
3. change the stress in the rod and reaction forces and moments at the boundaries,
4. alter the equilibrium bifurcation characteristics, and
5. soften the rod due to off-diagonal coupling terms in the stiffness matrix.

References:

1. Costello, G.A., *Theory of Wire Rope*. 3 ed. 1997, New York: Springer-Verlag.
2. Healey, T.J., *Material symmetry and chirality in nonlinearly elastic rods.* Mathematics And Mechanics Of Solids, 2002. **7**(4): p. 405-420.
3. Marko, J.F., *Stretching must twist DNA*. Europhysics Letters, 1997. **38**(3): p. 183-188.
4. Zachmann, D.W., *Non-Linear Analysis Of A Twisted Axially Loaded Elastic Rod.* Quarterly Of Applied Mathematics, 1979. **37**(1): p. 67-72.
5. van der Heijden, G.H.M., et al., *Instability and self-contact phenomena in the writhing of clamped rods.* International Journal Of Mechanical Sciences, 2003. **45**(1): p. 161-196.
6. Branden, C. and J. Tooze, *Introduction to Protein Structure*. 2 ed. 1999, New York: Garland Publishing.
7. Calladine, C.R., et al., *Understanding DNA, the Molecule and How It Works*. 3 ed. 2004, Amsterdam: Elsevier Academic Press.
8. Lehninger, A.L., D.L. Nelson, and M.M. Cox, *Lehninger Principles of Biochenistry*. 4 ed. 2005, New York: W. H. Freeman.

Chapter 6

Dynamics of Self-Contact and Intertwining

Modeling self-contact in rods is a pre-requisite for the simulation of cable intertwining, hockling and knot formation; yet it has been a significant research challenges in rod theory. In this Chapter, we introduce a computational self-contact model and illustrate its ability to capture the dynamic evolution of intertwining in response to torsional buckling. The intertwined shapes resemble hockles in underwater cables and plectonemes (one type of supercoils) in DNA. Numerical solutions are presented for an example system of a rod subjected to increasing twist at one end. The solutions show the dynamic evolution of the rod from an initially straight element, through a buckled element in the approximate form of a helix, through the dynamic collapse of this helix into a loop, and subsequent intertwining of the loop with multiple sites of self-contact.

6.1 Numerical Model of Dynamic Self-Contact
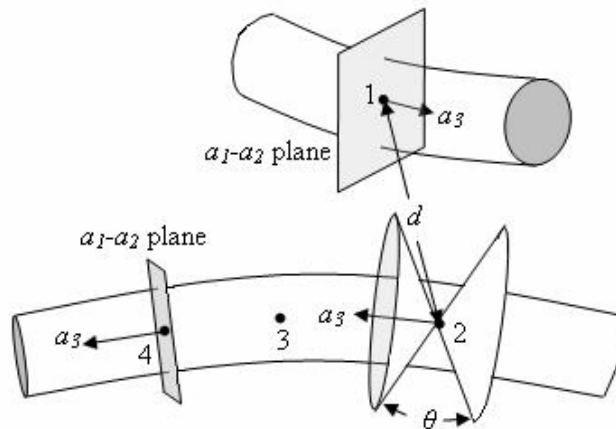
Figure 6.1 Two segment of a rod approaching contact.

A numerical formulation of self-contact must begin with first determining the likely sites where self-contact exists or will soon occur. We developed an efficient computational strategy to search for these "self-contact" sites. The contact forces are assumed normal to the rod surfaces[23] and allow for sliding contact. Figure 6.1 shows two segments of the discretized rod that are approaching contact. The upper segment contains one spatial grid point marked as 1, while the lower segment contains three grid points marked as 2, 3 and 4. At each grid point, the a_1-a_2 plane is orthogonal to the tangent[24] a_3. We introduce an *aperture angle* θ that creates a pair of conical surfaces centered at the grid point as illustrated at point 2 in Fig. 13. Note that this aperture reduces to the a_1-a_2 plane as $\theta \rightarrow$ 0°, and it expands to the entire space as $\theta \rightarrow$180°. We use this aperture to control the number of points that may potentially interact through self-contact Specifically, we wish to exclude adding non-physical 'contact' forces between nearby nodes on the same segment since the 'interactions' of these neighboring points are already captured in the rod constitutive law.

During simulation, the distance d between each pair of grid points is measured. A repulsive (contact) force is introduced between a pair if and only if two conditions are met: 1) the distance d is within a specified tolerance, and 2) the two grid points lie within each other's *conical aperture*. The interaction force can in general be a function[25] of d and $\dot{d}$ (the approach speed) and is included in the balance of linear momentum Eq. (2.6) through the distributed force term F. Example interaction laws that can be employed include (attractive-repulsive) Lennard-Jones type (refer to, for example Schlick et al. [1]), (screened repulsion) Debye-Huckle type (refer to, for example Schlick et al. [2]), general inverse-power laws (refer to, for example Klapper [3]), and idealized contact laws for two solids (refer to, for examples Coleman et al. [4] and Heijden et al. [5]).

---

[23] At the length scale of DNA, it's irrelevant to define a distinct contact surface, but we can circumscribe a fictitious cylindrical surface around the molecule to model its self-interaction.

[24] In this illustration and in the results of this Chapter, we assume that $a_3 = \hat{t}$. But this assumption does not limit the generality of the self-contact formulation presented herein.

[25] This function can also be defined suitably to account for the attractive-repulsive potential of van der Waals or, more generally, the MPB electrostatic screening (See Appendix 3).

6.2 Torsional Buckling Leading To Intertwining

The model is used to explore several possible dynamic motions that are generated by slowly twisting one end of an elastic rod. The parameters that define the example are listed in Table 6.1 and Table 6.2 and a schematic of this example is illustrated in Figure 6.2. We again employ the linear elastic constitutive law described by Eq. (4.1) and Eq. (4.3) in Chapter 4. We assume no intrinsic curvature ($\kappa_0(s) = 0$) and no chirality ($k_c(s) = 0$). The selected rod is isotropic ($A_1(s) = A_2(s) = EJ_{1,2}$) but non-homogeneous (non-uniform). Specifically the central portion of the rod (middle 25%) is necked down to a smaller diameter (reduced by 10% over the remainder of the rod); refer to Figure 6.2 (not to scale). This small 10% variation in the diameter produces significant ($\approx 35\%$) variation in torsional stiffness ($C(s) = GJ_3$) and bending stiffness ($A_1(s) = A_2(s) = EJ_{1,2}$). The (distributed) self-contact force is repulsive and is of the form:

$$F_{contact} = \rho_c A_c \left(\frac{k_1}{(d - 0.5D)^{k_2}} + \frac{k_3}{d} \frac{\partial d}{\partial t} \left| \frac{\partial d}{\partial t} \right|^{k_4} \right) \tag{6.1}$$

This form captures both contact stiffness and contact damping. For the example simulation presented below, we have chosen $k_1 = 10^{-7} \text{m}^4/\text{s}^2$, $k_2 = 3$, $k_3 = 10^{-6}$ and $k_4 = 1$.
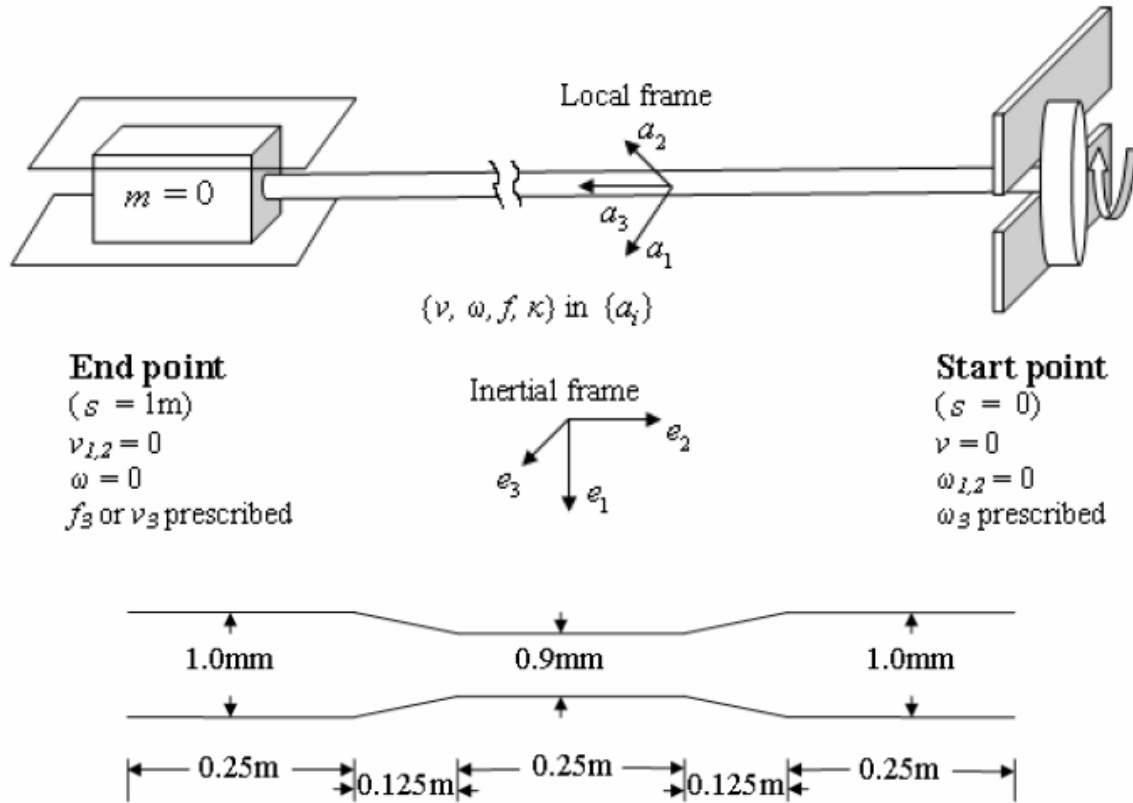
Figure 6.2 A low tension cable or rod under increasing twist created by rotating the right end. Left end is free to slide, or have prescribed sliding velocity or reaction (tension) in the simulation.

Table 6.1 Rod properties and simulation parameters.

Quantity	Units (SI)	Value
Young's Modulus, E	Pa	1.25×10^7
Shear Modulus, G	Pa	5.00×10^6
Diameter, D	m	See Figure 6.2
Length, L	m	1.00×10^0
Rod Density, ρ_c	Kg/m^3	1.50×10^3
Fluid Density, ρ_w	Kg/m^3	1.00×10^3
Temporal Step, Δt	s	1.00×10^{-1}
Spatial Step, Δs	m	1.00×10^{-3}

Table 6.2 Cross-section properties

Quantity	Formula	Units (SI)
Cross-section Area	$A_c = \dfrac{\pi D^2}{4}$	m^2
Area Moments of Inertia (bending)	$J_{1,2} = \dfrac{A_c D^2}{16}$	m^4
Area Moment of Inertia (torsion)	$J_3 = \dfrac{A_c D^2}{8}$	m^4
Mass Moment of Inertia/ length	$I = \rho_c J$	Kg-m

The integration begins with the rod initially horizontal and stress-free. It is in a fluid (with no flow) that provides added mass and drag (as modeled by a Morison formulation [6]). There is no gravity (and hence no buoyancy). However, a minute distributed force in the downward (e_1) direction is added to initiate buckling.

The right end (referred to as the "Start point", $s = 0$ in Figure 6.2) of the rod is subjected to an increasingly larger rotation about the a_3 (tangent) axis. This end cannot move and it is otherwise constrained in rotation (no rotation about the principal axes a_1 and a_2, i.e. $\omega_1 = \omega_2 = 0$). The left end (referred to as the "End point", $s = L$) of the rod is fully restrained in rotation (about all three axes) and cannot translate in the transverse (a_1-a_2) plane. This end, however, may translate along the a_3 axis.

By increasing the rotation at the right end, the internal torque eventually increases to the point to generate torsional buckling (refer to Zachmann's buckling condition [7]) and subsequent nonlinear dynamic response. In this simulation, the rotation of the right end is generated by prescribing the angular velocity component ω_3 at the right end as shown in Figure 6.3 (not to scale). The left end is allowed to translate freely during the first 30 seconds and is then held fixed to control what would otherwise be a very rapid collapse.
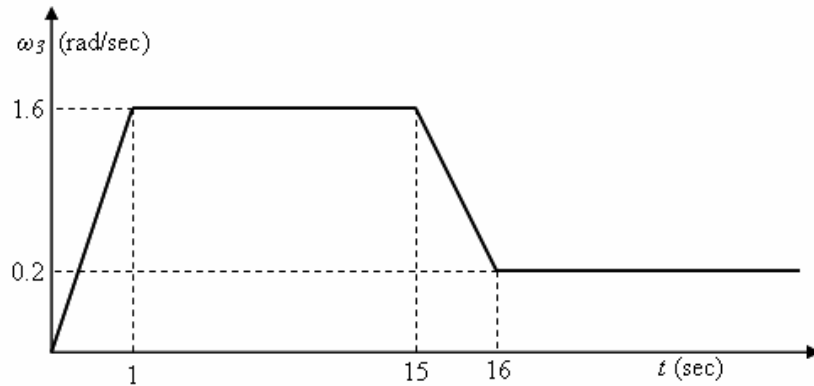
Figure 6.3 Prescribed angular velocity at the right end.

As the right end is first twisted by a modest amount, the rod remains straight. There is an abrupt change however when the twist reaches a critical value (at approximately 16 seconds) when the Zachmann buckling condition [7] is achieved and the straight (trivial) configuration becomes unstable. The model employed here captures this initial instability as well as the subsequent nonlinear motion that leads to loop formation and ultimately intertwining. Figure 6.4 shows snap-shots of the rod at four different time-steps during the buckling. The geometry just after initial buckling is approximately helical as can be observed in the snap-shot at 20 seconds. Notice that the rod appears to make a single helical turn as expected from the fundamental buckling mode of the (simpler) linearized theory [7].
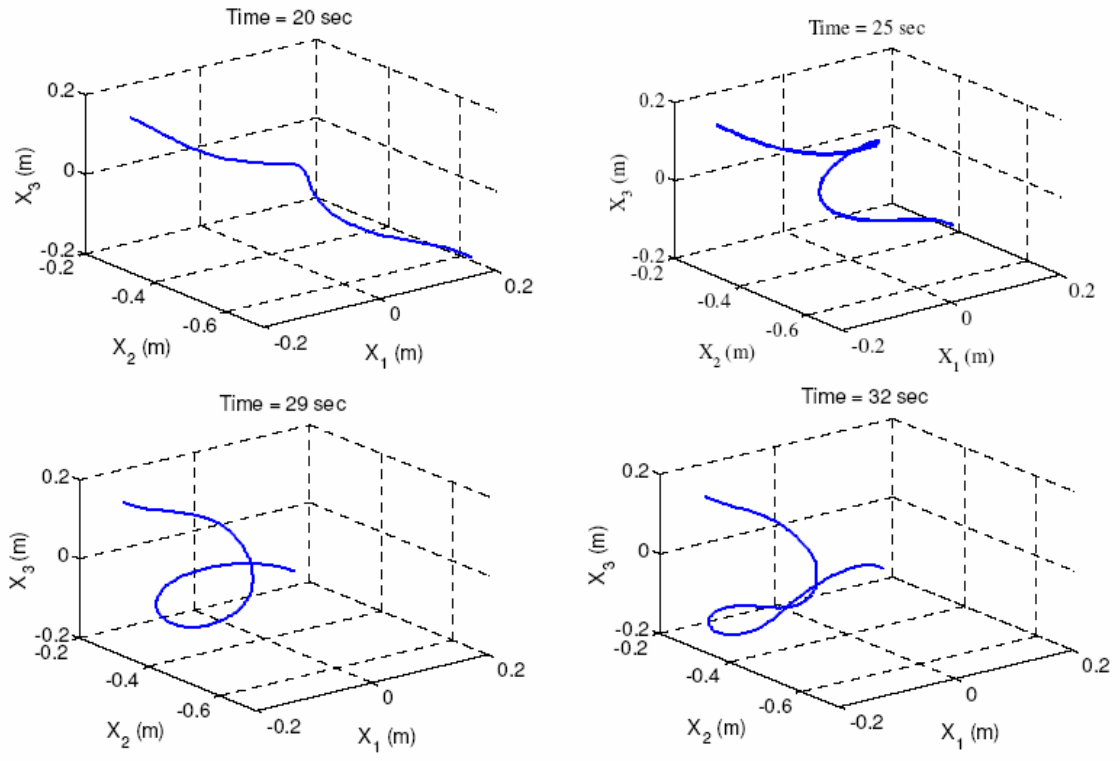
Figure 6.4 Snap-shots at various time steps during buckling.

As the left end is allowed to slide towards the right end, the helical rod undergoes a secondary buckling in which it rapidly collapses in forming a (nearly) planar loop with self-contact. This collapse occurs at approximately 29 seconds in this example. The dynamic collapse is predicted from investigations of the stability of the equilibrium forms of a rod under similar loading conditions; refer to Lu and Perkins [8] and studies cited therein.

The snap-shot at 25 seconds shows the three-dimensional shape of the rod just before dynamic collapse. The center of the rod has rotated approximately 90° about the vertical (e_1) axis so that the tangent at this (mid-span) point is now orthogonal to the loading (e_2) axis. This was a noted bifurcation condition in Lu and Perkins [8] at which the three-dimensional equilibrium form loses stability. The dynamic collapse thereafter is depicted in the snap-shot at 29 seconds. This nearly planar loop, however, is still unstable and rapidly continues to rotate leading to intertwining with two sites of contact. A snapshot of intertwined rod at 32 seconds is shown.
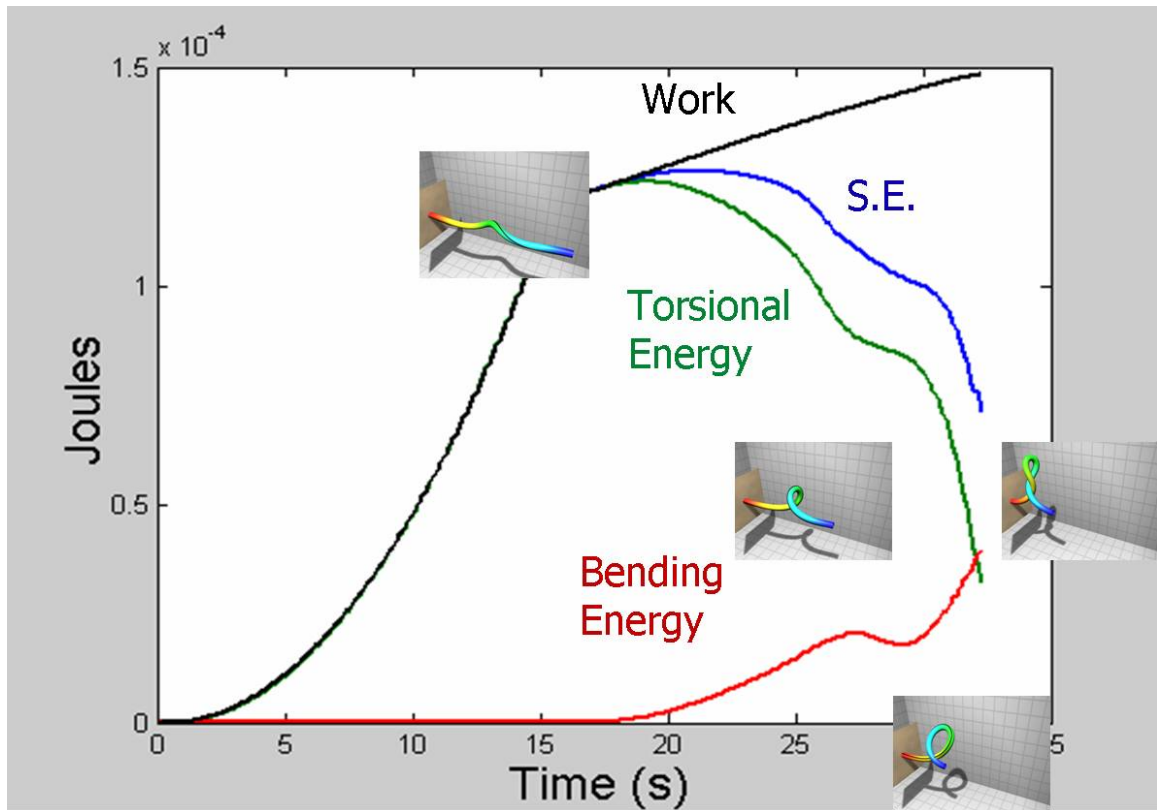
Figure 6.5 Variation in torsional and bending strain energies during the buckling process.

The entire dynamic collapse depicted in Figure 6.4 involves a conversion of torsional strain energy to bending strain energy as shown in Figure 6.5. The process begins with an increase in torsional strain energy prior to the collapse from the prescribed rotation at the right end. The maximum torsional strain energy occurs at approximately 18 seconds and follows shortly after the initial buckling (approx. 16 seconds) when bending strain energy first develops. This is followed by a rapid (dynamic) conversion of torsional strain energy to bending strain energy until around 25 seconds when it approaches the second bifurcation depicted in Figure 6.4 at 29 seconds where the loop collapses and self-contact first develops. During this secondary bifurcation, the rod loses both torsional and bending strain energies until the first self-contact and the intertwining begins.

During intertwining, the torsion in the rod is reduced rapidly with a modest increase in curvature. This results in a rapid loss of torsional strain energy and total potential energy

86

(S.E.) with a modest increase in bending strain energy. The loss in total potential energy is accompanied by an increase in kinetic energy suggesting faster dynamics during this stage. This example simulation ultimately terminated at 32 seconds due to high velocities.

6.3 Topological Changes

It is interesting to observe that the topological changes for the rod above are also exhibited by DNA during supercoiling. As discussed in Calladine et al. [9], the above conversion of torsional strain energy to bending strain energy is often described kinematically conversion of *twist* to *writhe* for DNA (see Appendix 1). We explain this conversion in the above example, starting with definitions for *twist* and *writhe*.

One definition for Writhe (Wr) is defined as the number of cross-overs of a space curve that one can see averaged over all possible views of the strand (refer to Calladine et al. [9]). For our initially straight configuration (Figure 6.2), this quantity is zero, with the first self-contact at 29 seconds (Figure 6.4), it is one, and with the subsequent intertwined configuration at 32 seconds, it is two. (Note that if we see a cross-over in three orthogonal views, we will see a cross-over in all possible views). The writhe (Wr) is purely a function of the space curve defining the rod centerline and it is positive or negative based on whether the crossing is right-handed or left-handed as illustrated in Figure A1.3 and Figure A1.4 in Appendix A1.

Twist (Tw) is a second kinematical quantity computed from:

$$Tw = \frac{1}{2\pi} \int_0^L \kappa_3 \, ds \qquad (7)$$

The sum Tw + Wr equals to the number of rotations of the right boundary in our example and this sum is called the *Linking number* Lk[26]; refer to Fuller [10] and White [11]) for

---

[26] This, in general, is not true for boundary conditions that allow rotation about principal axes ($\omega_{1,2} \neq 0$).

proof of conservation of the Linking number (Lk) and refer to Calladine et al. [9] for example discussions of Tw, Wr and Lk for DNA.
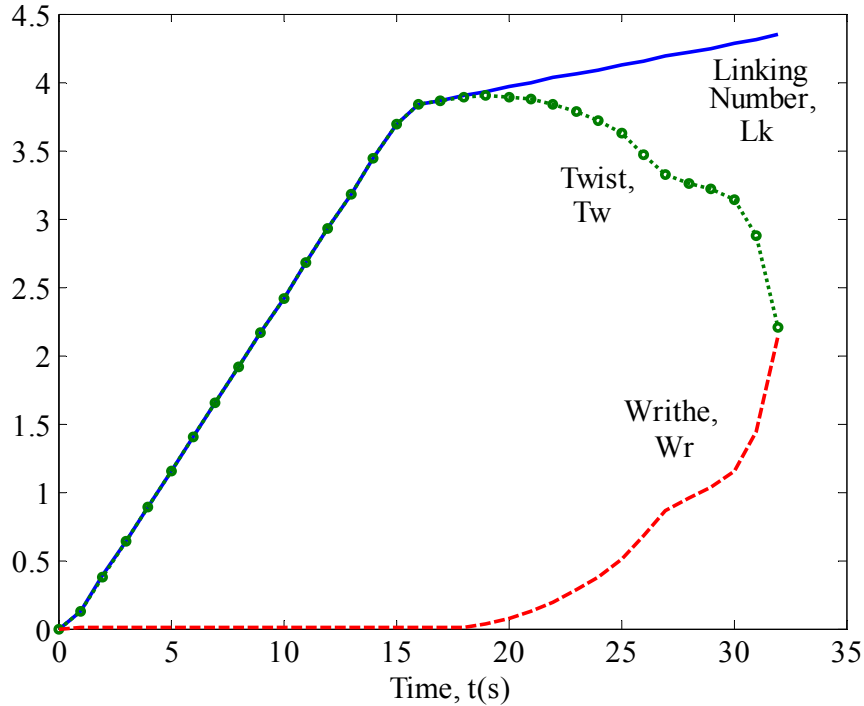
Figure 6.6 Conversion of twist (Tw) to writhe (Wr) during loop formation and intertwining . The linking number Lk = Tw + Wr.

In our example, the initial twisting phase rapidly introduces Lk from 0 to approximately 4, all in the form of twist, prior to the initial buckling as shown in Figure 6.6. The linking number is then increased slowly thereafter. During initial buckling, Wr increases from 0 to 1 when self-contact occurs at 29 seconds and Tw reduces by the same amount so that the sum Wr + Tw = Lk is unchanged. After the first self-contact, the loop continues to rotate as it intertwines. In doing so, every half rotation of the loop establishes an additional contact site thereby increasing Wr by 1.0 and reducing Tw by 1.0. At 32 seconds, Wr is slightly larger than 2.0. Thus, we observe two crossovers in any three orthogonal views of the snap-shot at 32 seconds. There is an equivalent loss in Tw as shown in Figure 6.6.

It should be noted that bending strain energy is not a measure of writhe (or the number of cross-overs), and unlike linking number, the total potential energy of the rod is not a conserved quantity. Therefore, the *kinematic* analysis in terms of twist and writhe not only validates the numerical results, but also provides a simple understanding of the topological changes of the rod under torsion.
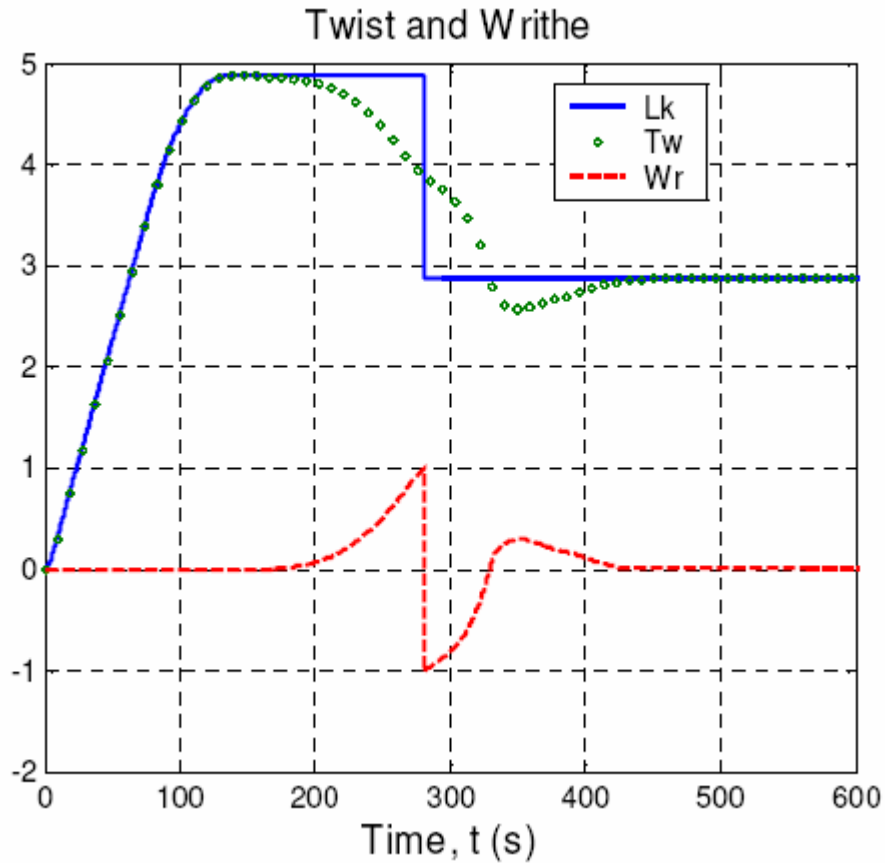
Figure 6.7 Variation of twist and writhe without modeling self-contact (refer to Goyal et al. [12]). The discontinuous reduction in the linking number and correspondingly in the writhe occurs when the rod passes through itself.

It should be also noted that when the self-contact is ignored, the rod may numerically 'cut through itself' losing Wr and Lk by 2 which is of course, non-physical. This is illustrated in Figure 6.7 from yet another example simulation of torsional buckling in a similar set up as above. For the simulation data and other results for this example, refer to Goyal et al. [12].

References:

1. Schlick, T., et al., *On Higher Buckling Transitions in Supercoiled DNA.* Biopolymers, 1994. **34**(5): p. 565-597.
2. Schlick, T., B. Li, and W.K. Olson, *The Influence of Salt on the Structure and Energetics of Supercoiled DNA.* Biophysical Journal, 1994. **67**(6): p. 2146-2166.
3. Klapper, I., *Biological applications of the dynamics of twisted elastic rods.* Journal Of Computational Physics, 1996. **125**(2): p. 325-337.
4. Coleman, B.D., D. Swigon, and I. Tobias, *Elastic stability of DNA configurations. II. Supercoiled plasmids with self-contact.* Physical Review E, 2000. **61**(1): p. 759-770.
5. van der Heijden, G.H.M., et al., *Instability and self-contact phenomena in the writhing of clamped rods.* International Journal Of Mechanical Sciences, 2003. **45**(1): p. 161-196.
6. Morison, J.R., et al., *The Force Exerted By Surface Waves On Piles.* Transactions Of The American Institute Of Mining And Metallurgical Engineers, 1950. **189**: p. 149-154.
7. Zachmann, D.W., *Non-Linear Analysis Of A Twisted Axially Loaded Elastic Rod.* Quarterly Of Applied Mathematics, 1979. **37**(1): p. 67-72.
8. Lu, C.L. and N.C. Perkins, *Complex Spatial Equilibria Of U-Joint Supported Cables Under Torque, Thrust And Self-Weight.* International Journal Of Non-Linear Mechanics, 1995. **30**(3): p. 271-285.
9. Calladine, C.R., et al., *Understanding DNA, the Molecule and How It Works*. 3 ed. 2004, Amsterdam: Elsevier Academic Press.
10. Fuller, F.B., *Writhing Number Of A Space Curve.* Proceedings Of The National Academy Of Sciences Of The United States Of America, 1971. **68**(4): p. 815-&.
11. White, J.H., *Self-Linking And Gauss-Integral In Higher Dimensions.* American Journal Of Mathematics, 1969. **91**(3): p. 693-&.
12. Goyal, S., N.C. Perkins, and C.L. Lee. *Torsional buckling and writhing dynamics of elastic cables and DNA.* in *2003 ASME Design Engineering Technical Conferences and Computers and Information in Engineering Conference*. 2003. Chicago, IL, United States: American Society of Mechanical Engineers

Chapter 7

Protein-Mediated DNA Looping

Protein-mediated looping of DNA is a key gene regulatory mechanism (for example, refer to Semsey et al. [1] and Schleif [2]). Loops occur when a protein binds to two operators on the same DNA molecule. The probability of looping is controlled, in part, by the base-pair sequence of inter-operator DNA which influences its structural properties. One structural property is the 'intrinsic' or 'stress-free' curvature. In this Chapter, we explore the influence of sequence-dependent intrinsic curvature by exercising our computational rod model for the inter-operator DNA as applied to looping of the LacR-DNA complex. Starting with known sequences for the inter-operator DNA, we first compute the intrinsic curvature of the helical axis as input to the rod model. The crystal structure of the LacR (with bound operators) then defines the requisite boundary conditions needed for our dynamic rod model that predicts the energetics and topology of the intervening DNA loop. Our simulations reveal that highly curved sequences tend to lower the energetic cost of loop formation, widen the energy distribution among stable and meta-stable looped states, and substantially alter loop topology. The inclusion of sequence-dependent intrinsic curvature also leads to non-uniform twist and necessitates consideration of eight distinct binding topologies from the known crystal structure of the LacR-DNA complex.

7.1 Introduction to LacR-DNA Modeling

DNA is often viewed as a static structure, whose primary role is to store the genetic code of the cell. In addition to this static picture, the structural flexibility and sequence-dependent mechanical properties of DNA enable the dynamic formation of complex protein-DNA assemblies responsible for gene regulation, DNA replication, and DNA

repair. It is therefore important to consider the interplay between sequence, mechanical properties, and dynamics of DNA to fully understand its biological functions.

One way in which the structure and mechanical properties of DNA can influence bio-molecular activity is by forming protein-mediated DNA loops; see, for example Semsey et al. [1] and Schleif [2]). In such instances, a protein or protein complex binds simultaneously to (at least) two non-contiguous operator sites on a DNA molecule, thereby forcing the intervening DNA into a loop. Depending on the specific proteins and sequences involved, a DNA loop can affect transcription by either repressing or promoting the binding and activity of RNA polymerase [2, 3].

In this Chapter, we employ our computational rod model of the inter-operator DNA as a means to explore sequence-dependent effects on looping. In particular, our objective is to understand how the looping energy and topology are influenced by the sequence-dependent *intrinsic curvature (or stress-free curvature)* of the substrate DNA. We also recognize the importance of sequence-dependent stiffness in this context as discussed in [7-15]. However, our objective is to explore the role of sequence-dependent intrinsic curvature which, while frequently addressed in experimental studies [16-18], has received relatively little attention from the modeling community. An overview of our goal, as well as our computational method, is illustrated in Figure 7.1. We adopt the lactose repressor protein DNA complex (LacR) found in the bacterium *E. coli* as our example. As illustrated in Figure 7.1, we begin by specifying the sequence of the substrate DNA from which we compute its zero-temperature, stress-free conformation (via consensus tri-nucleotide model [4, 5]) and, subsequently, the intrinsic curvature of the helical axis as input to the rod model. We then employ the known crystal structure of the LacR protein bound to the operators (4.80Å resolution as reported by Lewis et al. [6]) to compute the position and orientation of the rod (boundary conditions) at the operator sites. The dynamic computational rod model is then used to predict the topology and energetics of the resulting inter-operator loop.
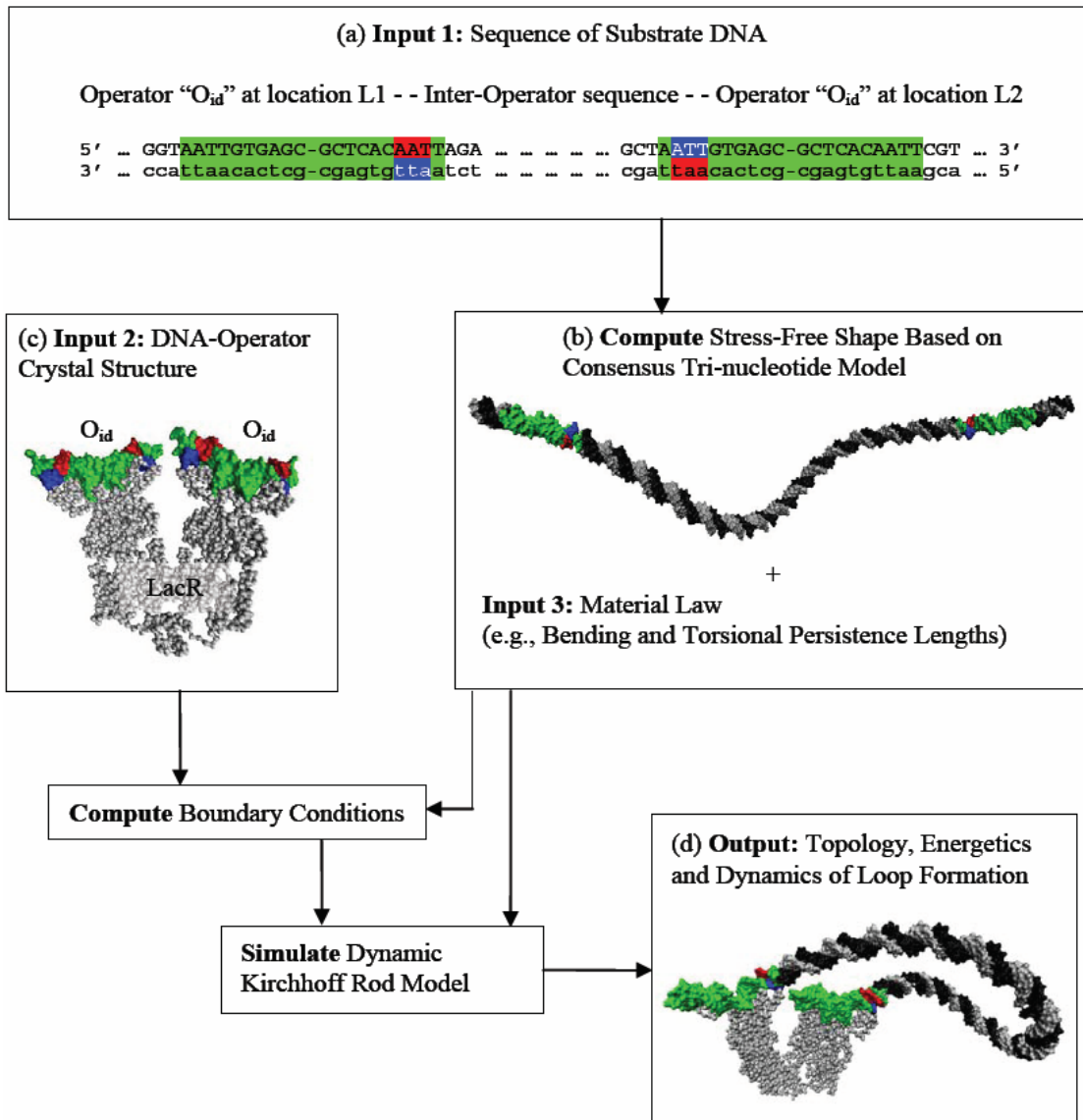
Figure 7.1 Modeling the effects of sequence-dependent, intrinsic curvature in looping of LacR-DNA. (a) Begin with specifying operator and inter-operator sequences (green denotes operators, capital case denotes the primary coding strand). (b) Construct zero-temperature, stress-free conformation using Consensus Tri-nucleotide model [4, 5] and compute intrinsic shape for rod model (twist and curvature of helical axis and inclination of the base-pair planes with respect to the helical axis). (c) Employ known crystal structure of the LacR protein bound to the operators [6] and intrinsic shape to compute boundary conditions for rod model of looped DNA. (d) Input boundary conditions, intrinsic shape and DNA material law to our rod model to compute inter-operator loop.

To explore how the energy and topology of DNA loops are sensitive to the sequence-dependent intrinsic curvature, we consider both wild-type and curved variants of the inter-operator DNA for the LacR-DNA complex. The convenience of this example is that Kahn and co-workers have already studied LacR looping with a set of designed

constructs whose highly curved inter-operator sequences contain A-tracts with known and distinct helical phases with respect to the operators [16-18]. Their studies, using gel-electrophoretic and FRET experiments, provide experimental evidence that A-tract bends increase LacR loop stability and alter loop topology. By employing their inter-operator sequences as inputs to our computational model, we can probe these and other findings. Although our present focus is on LacR-mediated looping, the methods described herein can be generally applied to other examples [1, 2] of looping behavior such as arising in GalR [19, 20], Ara [21], SfI [22, 23] and ntrC [24] in addition to other (non-looping) behavior such as plectoneme formation in supercoiled DNA as discussed in part in Chapter 6.

Our computational approach builds upon a long history of coarse-grain models for DNA dynamics that include Brownian dynamics simulations, Monte Carlo methods, and other statistical models [8, 25-27] that are also reviewed in [28, 29]. The Kirchhoff rod approach leads to detailed descriptions of loop topology and internal (elastic) energy with modest computational effort. Our inclusion of sequence-dependent intrinsic curvature also builds upon the prior work of Schulten and co-workers [30-35] who employ a homogeneous elastic rod model to analyze the mechanics of LacR looping. The sequence-dependent intrinsic curvature included herein, renders the rod model non-homogenous and leads to substantial differences (both qualitative and quantitative) in the predictions of loop topology and internal energy.

The computational model used in this study requires three major inputs; namely, 1) the sequence of substrate DNA, 2) the crystal structure of LacR-operator complex, and 3) the material law for DNA; refer to Figure 7.1. By material law, we refer to the elastic properties (that includes stiffness and intrinsic curvature) of DNA which themselves can be sequence-dependent [7-15]. We presently ignore sequence-dependence of stiffness to quantify the exclusive contribution of sequence-dependence of intrinsic curvature on looping behavior. To this end, we employ averaged stiffness constants using published values of bending and torsional persistence lengths [36-38]. The computational model, however, provides the framework for incorporating both sequence-dependent linear

elastic material laws as well as nonlinear (and inelastic) laws [13, 14, 39, 40] should they someday become well-characterized. We also treat the LacR as rigid and thereby ignore the effects of protein flexibility that has been analyzed in [35, 41, 42]. With the above assumptions duly noted, the computational model reveals the following major influences of sequence-dependent intrinsic curvature on looping in the LacR-DNA complex. First, the highly curved sequences of [18] tend to lower the energetic cost of the (lowest energy) stable loops, widen the energy distribution among stable and meta-stable loops, and substantially alter loop topology. Second, the inclusion of sequence-dependent intrinsic curvature leads to non-uniform twist (or twist deficit) as recognized in [43] and also necessitates consideration of eight distinct binding topologies from the known crystal structure of the LacR complex.

We emphasize again that intrinsic curvature is only one manifestation of sequence-dependent behavior and properly accounting for other physical behaviors in a model of the LacR-DNA complex will also influence the computed loop topology and energy. For example, including protein flexibility, twist-extension coupling in DNA, and sequence-dependent stiffness parameters would all lower the loop strain energy relative to that computed herein. We discuss the current limitations of our model and several extensions in detail after presenting our results.

7.2 Methods

In the Kirchhoff rod model, ds-DNA is approximated as a flexible rod having elastic properties as determined from single molecule experiments [44-47], MD simulations [9] and other biophysical techniques. We begin by reviewing the salient features of our computational rod model described in Chapter 2 for use in this study. We then detail how we incorporate sequence-dependent (non-homogeneous) intrinsic curvature in our formulation starting from knowledge of the inter-operator sequence.

Non-homogeneous Rod Model for DNA
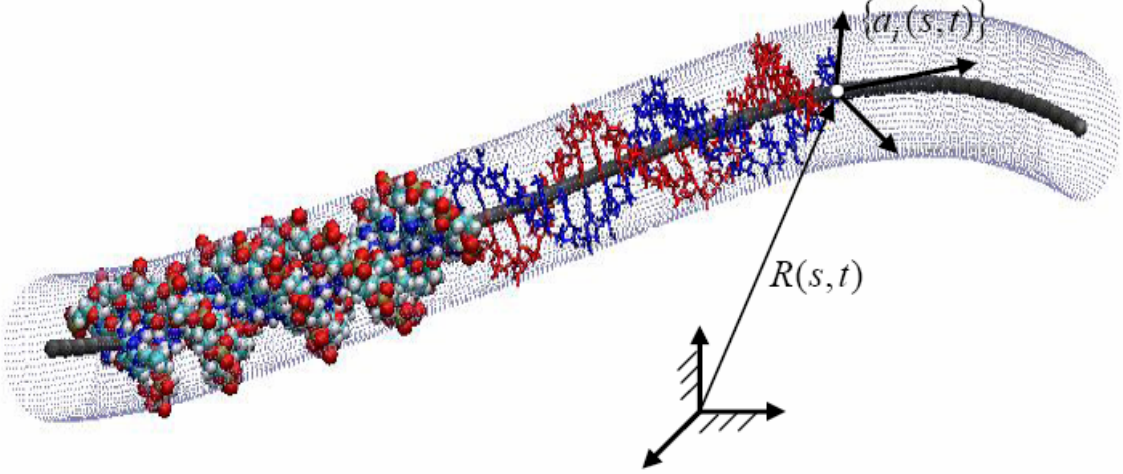
Figure 7.2 Rod model of (ds) DNA on long-length scales. Helical axis of duplex defines the rod centerline which forms a three-dimensional space curve located by $R(s,t)$.

Figure 7.2 illustrates a segment of ds-DNA with its helical axis defining the centerline of an equivalent rod. The shape of ds-DNA is parameterized by the three-dimensional centerline curve $R(s,t)$ and the cross-section fixed frame $\{a_i(s,t)\}$. This equivalent rod model can be used to study the energetics and topology of DNA looping by formulating its mechanical properties (described below) based on experimental data and/or MD simulations.

Under stress-free conditions, the helical axis is not straight but conforms to a curved/twisted space curve. This intrinsic curvature of ds-DNA is captured by $\kappa_0(s)$ and it depends on the base-pair sequence. The change in curvature/twist, $\kappa(s,t) - \kappa_0(s)$, produced by any subsequent deformation of the helical axis (e.g., by protein binding), generates an internal moment $q(s,t)$ and internal force $f(s,t)$. This response is governed by the long-length scale material law, which can be estimated from experiments or MD simulations. The inter-atomic interactions conspire to yield the long-length scale material law which is often assumed to be linearly elastic (see, for example, [5, 10, 11, 28-35, 48-50]). An exception is the nonlinear law proposed in [13, 14, 40] for highly kinked strands, which has also been questioned in subsequent studies [39]. Here, we shall adopt a linear elastic law as described in Eq. (4.1). We assume homogeneous

bending and torsional stiffness $B(s) = B$ to screen out the effects of sequence-dependent stiffness and only capture the effects of sequence-dependent curvature $\kappa_0(s)$. We also ignore bending anisotropy which averages out over a helical turn into and effective isotropic bending stiffness for long length scale effects as suggested by Maddocks and co-workers [51, 52]. We also turn off the chiral coupling $(k_c(s) = 0)$ discussed in Chapter 5 which may otherwise mask some the effects of sequence-dependent intrinsic curvature $\kappa_0(s)$ alone. (One those effects is non-uniform distribution of twist/ untwist $\Delta\kappa_i(s)$). Thus the assumed constitutive law takes the following form

$$q(s,t) = B\big(\kappa(s,t) - \kappa_0(s)\big), \tag{7.1}$$

where the stiffness tensor B includes both bending and torsion stiffness, refer to Eq. (4.1) and Eq. (4.3) in Chapter 4 Commonly used values of the bending and torsional stiffness can be found from experimental measurements of the persistence lengths for bending/torsion [36-38]. The above law renders the rod model non-homogenous, that is, sequence-dependent by capturing the effects of intrinsic curvature/twist $\kappa_0(s)$. The associated elastic strain energy density follows from

$$S_e(s,t) = \frac{1}{2}\big(\kappa(s,t) - \kappa_0(s)\big)^T B\big(\kappa(s,t) - \kappa_0(s)\big), \tag{7.2}$$

where the superscript T denotes matrix transposition. This result can be readily used to understand how the elastic energy is distributed along the looped inter-operator DNA and its decomposition into components due to bending and twisting.

The deformation of the rod is governed by a set of differential equations (refer to Eq. (2.6) – Eq. (2.9) in Chapter 2) that are integrated using specified boundary conditions. For example, the boundary conditions for the inter-operator DNA loop define the relative position and orientation of the LacR operators known from the crystal structure [6] as detailed later. We describe the kinematics of this deformation by the linear velocity $v(s,t)$ and the angular velocity $\omega(s,t)$ of the rod cross-section.

Note that the formulation used is *dynamical* in that we track the rod deformation in time from an assumed initial state (initial condition). Doing so allows the solution to relax to equilibrium ($v = \omega = 0$) under the influence of hydrodynamic dissipation and, in the process, confirms the stability of the computed equilibrium. Employing a dynamic formulation is advantageous because the solution dynamically relaxes to a stable (looped) equilibrium. The predictions of looped or supercoiled states directly from *equilibrium* rod theory (e.g. [10, 30, 31, 34, 49, 50]) require a subsequent analysis of loop stability. Furthermore, equilibrium theories cannot capture possible dynamic transitions between equilibrium states as highlighted in Chapter 4. Finally, note that while we employ a specific (linearly elastic) material law for ds-DNA, the formulation above is general in that Eq. (7.1) may be replaced with any other proposed material laws including those that capture sequence-dependent stiffness [8, 9, 12, 15] and nonlinear material behavior [40].

In this study, the dynamical formulation is used as a numerical means to converge to the final equilibrium (looped) states, and it is not used to study or represent the dynamic pathway for looping in the presence of thermal fluctuations. We accomplish this by integrating from the initial stress-free shape of the inter-operator DNA and then slowly transforming the operators from their stress-free conformation to their (final) position and orientation when bound to the LacR. The final loop topology and elastic energy are then computed. In other words, the boundary conditions for the rod are slowly varying and prescribed functions of time that begin with those of the stress-free state and end with those of the (final) looped state. We detail in Appendix 8 how we define the boundary conditions for the (final) looped state for the DNA-LacR complex. The inter-operator DNA modeled here as a rod includes three base-pairs from each operator site (see Appendix 8) as also assumed in [30-35].
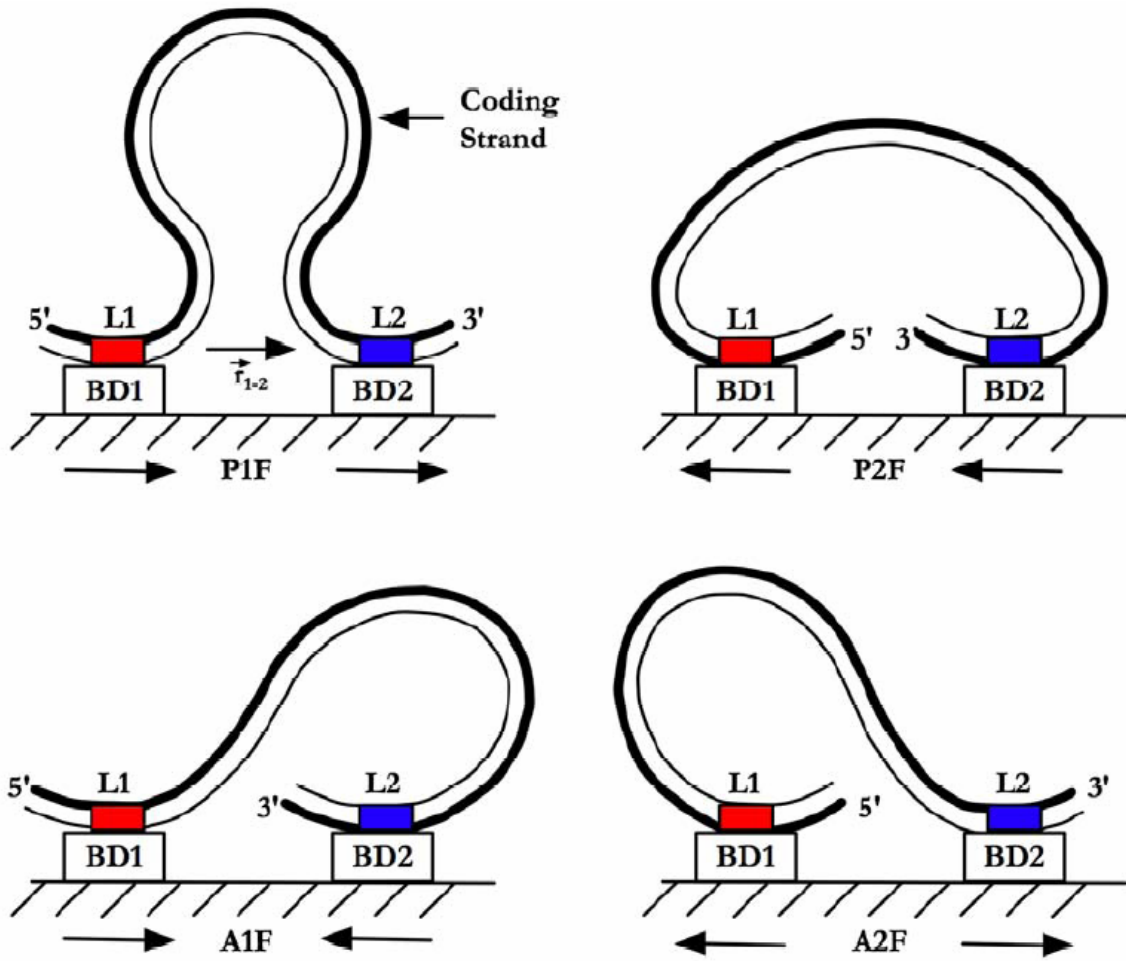
Figure 7.3 Four of eight possible binding topologies. The operator locations L1 and L2 on the substrate DNA may bind to the protein binding domains BD1 and BD2. The operators at L1 and L2 are identical and palindromic. A three-digit binary notation is used to distinguish all eight possible binding topologies and all "forward" (F) binding topologies are illustrated here.

In aligning the boundary base-pairs with the known crystal structure [6], we can consider eight possible binding topologies that distinguish how the operators bind to the binding domains. Note from Figure 7.1 that the operators are identical and palindromic. Because the operators at locations L1 and L2 are palindromes, we first consider four distinct ways to attach them to the two binding domains BD1 and BD2 as illustrated in Figure 7.3, where we also arbitrarily assumed that L1 always binds to BD1 (and L2 with BD2) (These four binding topologies were suggested to us by Prof. W. K. Olson, Department of Chemistry and Chemical Biology, Rutgers University). By then allowing L1 to bind to BD2 and L2 to BD1, we arrive at a total of eight possible binding topologies. Since the crystal structure of the LacR protein given by PDB ID: 1LBG [6, 53],

<http://www.pdb.org> appears to be asymmetric (by our calculations of data in [6, 53]) and so is the inter-operator DNA, the eight topologies are unique. For special cases (including palindromic inter-operator sequences and/or symmetry in the orientation of the boundary domains) one may arrive at fewer than eight (unique) binding topologies.

To distinguish the four binding topologies, two conventions have been proposed in the literature [19, 33]. Here, we elect to extend the original notation of Geanacopoulos et al. [19] to a three-digit binary notation to distinguish all eight binding topologies. According to [19], the first digit describes the relative orientation of the 5'-3' direction of the coding strand at the two boundary domains. If the dot product of these two directions is positive, the two directions are closer to being parallel than to being anti-parallel and the first digit is assigned the letter 'P'. If the dot product is negative, the two directions are closer to being anti-parallel than to being parallel and the first digit is 'A'. Next define the position vector $\vec{r}_{1-2}$ extending from L1 (the operator location at the 5' end of the coding strand) to L2 (the operator location at 3' end of the coding strand) as illustrated in Figure 7.3. The second digit is chosen to be 1 if the 5'-3' direction of the coding strand at L1 points towards the interior of the V-shaped protein, otherwise it is chosen to be 2. In other words, the second digit is 1 if the dot product of $\vec{r}_{1-2}$ and the 5'-3' direction at L1 is positive, or 2 if negative. Villa et al. [33] used 'O' and 'I' in their two digit binary notation resulting in 'II' = 'A1', 'OO' = 'A2', 'IO' = 'P1' and 'OI' = 'P2'. For the third digit, we define BD1 as the protein head group bound to the strands labeled H and G in the LacR crystal structure given by PDB ID: 1LBG [6, 53]. The boundary domain BD2 is then the other head group. The third digit distinguishes whether BD1 binds to L1 and BD2 binds to L2, as denoted by "F" for "Forward", or the opposite case denoted by "R" for "Reverse". All possible "Forward" binding topologies are illustrated and notated in Figure 7.3. If the inter-operator DNA is modeled as a homogeneous rod, the forward and reverse topologies are indistinguishable. Table 7.1 summarizes how the symmetry in protein and/ or DNA might reduce the number of distinct binding topologies needed to be considered.

Table 7.1 Effects of DNA/ protein symmetry on distinctness of binding topologies

Protein	Inter-Operator DNA	Distinct Binding Topologies
Asymmetric	Non –Homogeneous & Non-Palindromic	8
Asymmetric	Homogeneous or Palindromic	4
Symmetric	Non –Homogeneous & Non-Palindromic	4
Symmetric	Homogeneous or Palindromic	3

The above arguments determine the relative position and orientation of the two operators to within a single 2π rotation of one operator about any axis. In other words, the two operators achieve the same relative orientation after one is rotated about any axis by any whole number of turns. The additional turns produce an infinity of boundary conditions [54], corresponding to different topoisomers. Highly over-wound and under-wound topoisomers are expected to have high energetic cost in the LacR-DNA complex. Thus, as in prior predictions of looping for the LacR [30, 32-35], we exclude all cases of linking numbers sufficiently large to generate 'self-contact' of the inter-operator DNA. That said, computations with self-contact and even the formation of plectonemes are possible using this computational rod model upon the addition of a suitable contact law as demonstrated in Chapter 6.

Including Sequence-Dependent, Intrinsic Curvature

We now turn our attention to defining the intrinsic curvature/twist of the inter-operator DNA from knowledge of its sequence following the three steps below.

1. A web tool <http://hydra.icgeb.trieste.it/~kristian/dna/> [4, 5] is used to construct the stress-free all-atom representation (PDB file) of the entire sequence of each DNA given in Appendix 8 at zero temperature based on the consensus tri-nucleotide model [4]. This web tool outputs a protein data-bank file giving the co-ordinates of each atom.

2. A smooth (at least C^3 continuous) curve $R_0(s)$ is interpolated through the chain of atoms to approximate the helical axis averaging over base-pair origins [55] as detailed in Appendix 9.

3. We define the cross-section fixed unit vectors $a_1(s,t)$, $a_2(s,t)$ and $a_3(s,t)$ such that they align with the normal $\hat{n}(s)$, binormal $\hat{b}(s)$ and tangent $\hat{t}(s)$ unit vectors, respectively of $R_0(s)$ [56]. The intrinsic curvature and twist of the helical axis are determined by the "principal curvature" $\kappa_p(s)$ and "geometric torsion" $\tau(s)$ of $R_0(s)$ [56]. The components of the vector $\kappa_0(s)$ with respect to the triad $\{a_i(s,t)\}$ are $\{0 \quad \kappa_P(s) \quad \tau(s)\}$ and they are employed in Eq. (7.1) to capture the effects of sequence-dependent intrinsic curvature/twist on looping.

The steps above can also be reversed and doing so allows one to re-construct an approximate, all-atom representation of the deformed inter-operator DNA, from the computed helical axis of the rod model. To this end, we assume that the base-pair atoms can only undergo a rigid body motion and therefore their positions remain fixed with respect to the triad $\{a_i(s,t)\}$ attached to the helical axis. Thus, the locations of the base-pair atoms can be computed by tracking the position and orientation of the triad $\{a_i(s,t)\}$ which are known directly from the output of the computational rod model. We emphasize that this procedure leads only to an estimate of the final conformation and further refinements might also be possible via subsequent relaxation through MD simulation.

7.3 Results

The methods above are used to explore the topology and energetics of LacR-DNA loops with different inter-operator sequences. We include results from three numerical studies that in combination reveal the overall effects of sequence-dependent intrinsic curvature and corroborate three major conclusions from experimental studies [18, 57]; specifically,

- the sequence-dependent intrinsic curvature can reduce the energetic cost of looping [18],
- the sequence-dependent intrinsic curvature influences loop topology and the distribution of topoisomers [18],
- looping energy depends strongly on operator *orientation* compared to operator *separation* [57].

To this end, we first re-examine the computed loops for the wild-type sequence (see Appendix 8) and contrast our results with those in [34] where sequence-dependent intrinsic curvature was not incorporated in the computed results. We then explore looping in four other sequences (see Appendix 8) with designed A-tract bends [18]. Finally, we evaluate how the loop elastic energy depends on operator separation (length of the inter-operator sequence) as well as operator orientation.

Looping in Wild-type Sequence

Figure 7.4(a) depicts candidate stress-free, zero temperature conformations of the 77 bp inter-operator DNA (defined in Appendix A) for the wild-type sequence. The straight B-DNA (red) with 3.46Å height and 34.6° twist per base-pair step correspond to the homogeneous rod model used in [30, 32-35]. The consensus tri-nucleotide model [4] (blue/green) accounts for sequence-dependent shape modeled in our non-homogeneous rod. The helical axis of the B-DNA is straight which renders the principal curvature and geometric torsion identically zero, i.e., $\kappa_P(s) \equiv 0$ and $\tau(s) \equiv 0$. By contrast, $\kappa_P(s) \neq 0$ and $\tau(s) \neq 0$ for the consensus tri-nucleotide model [4] which yields a distinct three-

dimensional curve for the helical axis. Figure 7.4(b) illustrates the resulting principal curvature and geometric torsion computed from the consensus tri-nucleotide model (as functions of non-dimensional contour length s) which are then input to the computational rod model for studying looping.

(a)

(b)
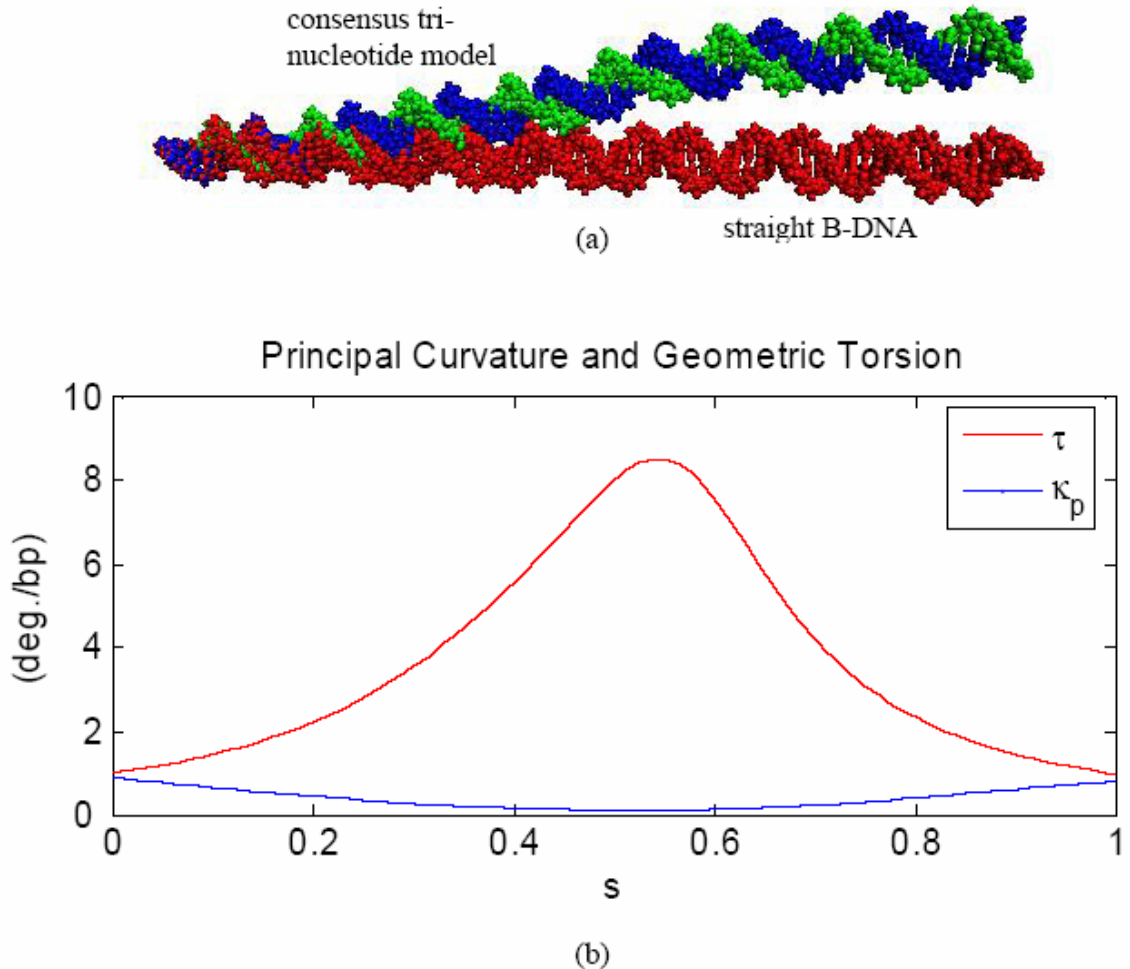
Figure 7.4 (a) Comparison of two different models of stress-free, zero-temperature, wild-type, inter-operator DNA: Red – straight B-DNA and Blue/ Green – consensus tri-nucleotide model [4]. The left boundary base-pair for the two models are aligned. (b) Principal curvature and geometric torsion of the helical axis for the consensus tri-nucleotide model [4] as a function of (non-dimensional) contour length s.

(a)   (b)

(c)   (d)
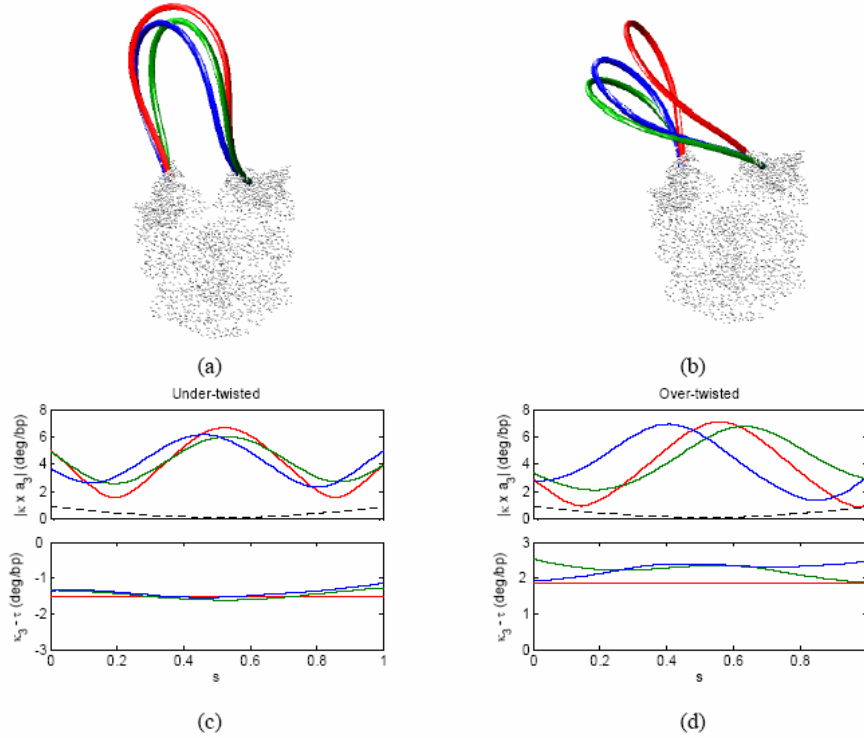
Binding Topology	Under-twisted Loop					Over-twisted Loop				
	E(kT)	ΔTw	Wr	Lk	Inter-ference	E(kT)	ΔTw	Wr	Lk	Inter-ference
Homogeneous B-DNA										
▬ P1	34.06	-0.32	-0.01	-0.33	No	37.99	0.39	0.25	0.64	No
A1	26.25	-0.27	-0.10	-0.37	No	33.86	0.36	0.23	0.59	No
A2	30.26	-0.42	-0.08	-0.50	No	29.83	0.41	0.09	0.50	No
P2	75.77	-0.66	-0.20	-0.86	No	35.57	0.06	0.07	0.13	No
Non-homogeneous consensus tri-nucleotide model (15)										
▬ P1F	35.23	-0.32	-0.03	-0.35	No	50.6	0.55	0.11	0.66	No
A1F	25.94	-0.16	-0.11	-0.27	No	41.48	0.40	0.27	0.67	No
A2F	27.14	-0.29	-0.34	-0.63	No	39.14	0.47	0.13	0.60	No
P2F	81.42	-0.30	-0.39	-0.69	Yes	52.74	0.07	0.47	0.54	No
▬ P1R	34.48	-0.29	-0.02	-0.31	No	50.24	0.52	0.14	0.66	No
A2R	25.41	-0.13	-0.08	-0.21	No	43.29	0.34	0.40	0.74	No
A1R	28.27	-0.30	-0.11	-0.41	No	37.61	0.48	0.08	0.56	No
P2R	75.9	-0.33	-0.14	-0.47	Yes	50.65	0.12	0.17	0.29	No

(e)

Figure 7.5 (a) & (b) Computed LacR loops for wild-type, inter-operator DNA for LacR. Loops accounting for intrinsic shape (binding topology P1R is shown in blue and binding topology P1F is shown in green) differ from those that ignore intrinsic shape (homogeneous B-DNA, binding topology P1 shown in red). Two solutions for the loop exist for each binding topology (ignoring self contact) - one is under-twisted (a) while the other is over-twisted (b). (c) & (d) Principal curvature and over-twist density of all loops above shown as functions of (non-dimensional) contour length coordinate *s*. The principal curvature for the (stress-free) consensus model (black) is reproduced for comparison. (e) Table summarizes the total over-twist (above the natural helical twist) ΔTw, writhe Wr, linking number Lk, and loop elastic energy E for all the binding topologies. The writhe Wr is computed using "Method 1a" described by Klenin and Langowski [58]. We form a closed loop for calculating writhe by adding a straight segment $\vec{r}_{1-2}$ that connects the two ends of the DNA bound to the protein in Figure 7.3. The stress-free B-DNA is characterized by a uniform twist of 34.6°/bp, zero principal curvature, and rise of 3.46 Å/bp. The bending and torsional persistence lengths are assumed to be 50nm and 75nm [36-38] respectively yielding a bending to torsional stiffness ratio of 2/3. The term 'Interference' is used whenever a visual check reveals DNA-protein steric interference.

105

For the two models we first examine the loops with P1 binding topologies (refer to Figure 7.3 for definition of P1 binding topology). Figure 7.5(a,b) illustrate the loops for both models – homogenous B-DNA (red) and non-homogenous consensus tri-nucleotide model (blue – P1F and green – P1R). Note that for homogeneous B-DNA, the binding topologies P1F and P1R yield identical loops and hence we designate them simply by P1. Computations reveal two loops (without self contact) of the inter-operator DNA for each binding topology, one under-twisted (Figure 7.5(a)) and the other over-twisted (Figure 7.5(b)). The principal curvature $|\kappa \times a_3|$ and over-twist density $(\kappa_3 - \tau)$ for each loop are reported in Figure 7.5(c,d) together with the intrinsic (principal) curvature of the stress-free, zero temperature state (black) for reference. For the case of vanishing intrinsic curvature (homogeneous B-DNA), the above formulation should replicate the results of [34]. Indeed, the computations shown in Figure 7.5(c,d) for homogeneous B-DNA (red) faithfully reproduce the principal curvature and over-twist density reported in [34] to within 0.2 deg/ bp. A summary of the total over-twist ΔTw, writhe Wr, link Lk, and loop elastic energy E for all binding topologies is provided in Figure 7.5(e). The lowest elastic energy (again without steric interference) is highlighted in blue font and the second lowest is in red font.

Looping in Four Sequences with Designed A-tract Bends

We now utilize the same methods with the consensus tri-nucleotide model to explore the role of intrinsic shape in the four highly curved sequences with phased A-tract bends introduced in [18]. The four sequences, denoted by control, 11C12, 7C16, and 9C14, are defined in Appendix A and their predicted stress-free, zero-temperature conformations are illustrated in Figure 7.6. The control sequence is nearly straight while the other three have similar A-tract bends with helical phase differences of approximately 70°.
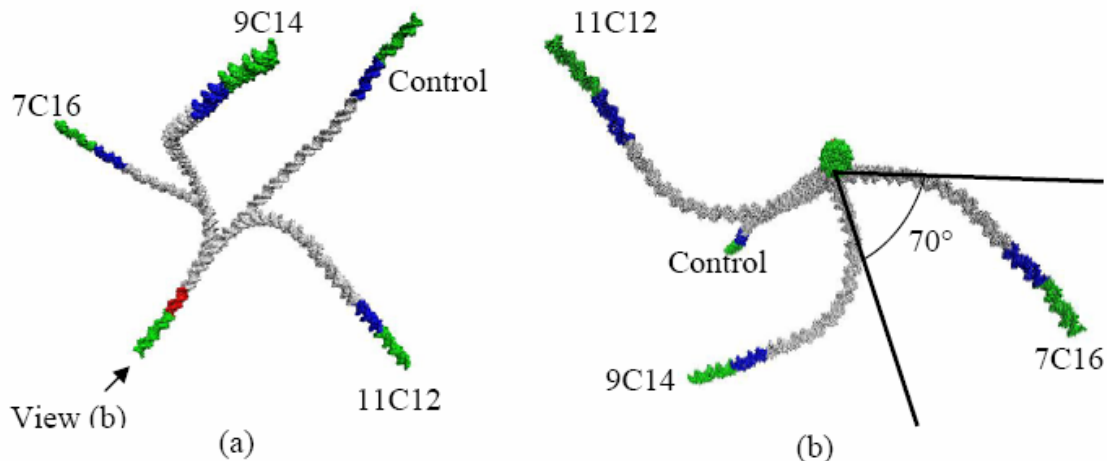
Figure 7.6 Two views of the stress-free, zero-temperature conformations of four designed inter-operator DNA sequences [18] as computed using the consensus tri-nucleotide model [4]. The first base-pair of each sequence is assigned the same position and orientation. The operator regions are shown in green, the red and blue segments are same in all the four constructs, but the silver segments are different in each of them. In the control sequence the silver segment is nearly straight, while in the others it has A-tract bends between two straight linkers of different lengths (refer Appendix 8). The control sequence is nearly straight as best observed in view (a). For the three variants, the inter-operator sequences contain a series of A-tract bends between two nearly straight linker regions of differing lengths. The different length linker regions lead to bends that are phased by approximately 70° about the helical axis of the control as best observed in view (b).

For each sequence, we used the computational rod model to compute the inter-operator loops formed by LacR binding and for all possible (eight) binding topologies; refer to Figure 7.3. As in the wild-type case, multiple (mechanically) stable loops are possible for each binding topology. Figure 7.7 illustrates the loop that achieves the *minimum* elastic energy for each sequence. In the table below we report the number of bp for the inter-operator sequence (as defined in Appendix 8), loop elastic energy, total over-twist, writhe and link for these minimum energy loops (illustrated) as well as those having the second lowest elastic energy (not illustrated). The loops with the second lowest elastic energies might correspond to the "most probable meta-stable states" of the Boltzmann distribution. If their free energies are close to those of the "stable states" (lowest energy states), the meta-stable states may co-exist with the stable states in a thermal environment with a high likelihood of inter-conversion. In fact, if one were to account for the other components of the free energy, a state having the 2nd lowest *elastic* energy may well yield

the global free energy minimum[27]. Note also that while some loops have very comparable elastic energies, their binding topologies and geometrical properties (e.g. whether over-twisted or under-twisted) can be altogether different.

(a) Control (Binding Topology: A2F)

(b) 11C12 (Binding Topology: A2R)

(c) 7C16 (Binding Topology: A2F)

(d) 9C14 (Binding Topology: P1F)
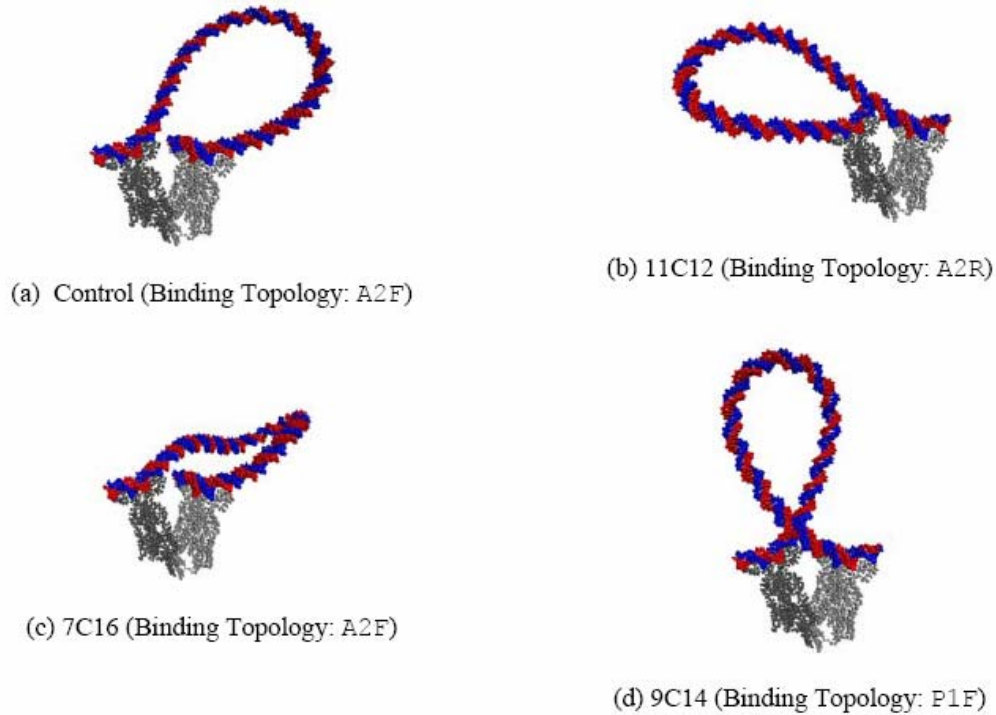
	Control (144 bp)		11C12 (141 bp)		7C16 (131 bp)		9C14 (142 bp)	
	min	2nd	min	2nd	min	2nd	min	2nd
Binding Topology	A2F	P1R	A2R	A1R	A2F	A1F	P1F	P1R
E (kT)	**11.93**	12.55	**7.38**	10.42	8.65	11.26	10.95	11.38
ΔTw	0.03	-0.07	-0.17	0.17	0.14	-0.28	0.12	0.11
Wr	-0.01	0.15	-0.21	0.18	-0.04	-0.16	0.27	0.37
Lk	0.01	0.08	-0.37	0.36	0.10	-0.44	0.39	0.48

Figure 7.7 (a)-(d) Lowest energy solutions for four designed sequences and the associated binding topology. (e) Table summarizing binding topology, loop elastic energy, over-twist, writhe and link for loops with the minimum and second smallest elastic energies. The largest of all the minimum energies is denoted in red font and the lowest in blue font. (e)

---

[27] For example, the entropic contribution to free energy is expected to be of the order of kT for a persistence length of DNA (~150 basepairs). If the 2nd lowest elastic energy loop is hardly a kT higher than the lowest elastic energy loop, we may need to account for entropy to determine the lowest free energy.

Influence of Inter-operator Length and Phase

The sequences of [18] considered above differ both in the location/phase of the A-tract bend as well as the number of base-pairs of the inter-operator DNA which range from 131 bp (7C16) to 144 bp (Control). The elastic energy of the resulting loops is certainly influenced by both factors. Therefore, the gel shift assays on the looping of the four sequences in [18] were influenced by both effects, not just the helical phasing of A-tracts with respect to the operators. In the following results, we isolate these influences on elastic loop energy.

Adding (or subtracting) a single base-pair is expected to change the loop energy by changing (a) the length of inter-operator DNA (e.g,. by 3.46 Å/base-pair), and (b) the relative orientation of the operators by one unit of base-pair twist (e.g., by 34.6°/base-pair). The first effect is negligible for the four designed sequences considered above since the relatively small differences in contour length (less than 0.7%/base-pair) generate negligibly small changes in the stiffness of the inter-operator DNA. By contrast, changes in the relative orientation of the operators may yield as much as a 50% change in elastic energy as shown in the results below.

Figure 7.8 illustrates the computed loop elastic energy for the Control sequence (modeled as straight B-DNA for the results presented in this figure) with the P1 binding topology. The solid curves represent the energy computed by simply rotating one operator about its tangent vector $\hat{t}$ in increments of the nominal base-pair twist (34.6°) while holding the number of base-pairs constant (142). The two curves distinguish two computed loops; one under-twisted (blue) and one over-twisted (red). The circles represent the energy computed by adding base-pairs and thereby simultaneously increasing the length of the inter-operator DNA as well as changing the relative orientation of the operators. The two sets of circles distinguish two computed loops; one under-twisted (blue) and one over-twisted (red).
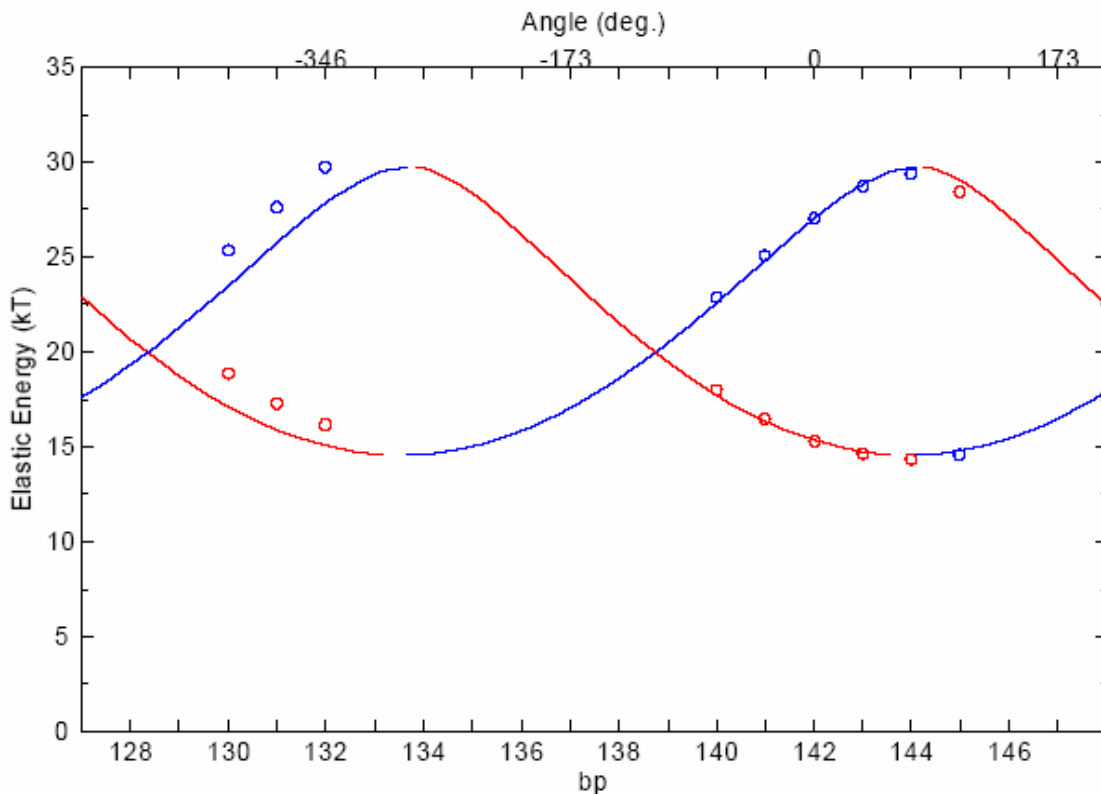
Figure 7.8 The influence of operator orientation and inter-operator length on loop elastic energy for straight B-DNA (Control) with P1F/P1R binding topology. Solid curves illustrate the periodic variation in elastic energy obtained by rotating one operator about the helical axis in increments of the base-pair twist (in this model 34.6°/base-pair) while keeping the inter-operator length constant (142 bp); refer to scale on top for relative angular orientation of operators. The circles illustrate the same variation obtained by adding base-pairs and thereby both rotating one operator as well as increasing the inter-operator length (in this model 3.46 Å/base-pair); refer to scale on bottom for bp number. Over-twisted solutions denoted by red, under-twisted solutions by blue.

7.4 Discussion and Conclusions

We open this discussion by describing the overall effects of sequence-dependent intrinsic curvature on the mechanics of looping. We then discuss how our computational results support three major conclusions drawn from experimental studies of the LacR-DNA complex [18, 57] including: 1) that sequence-dependent intrinsic curvature reduces the energetic cost of looping, 2) that sequence-dependent intrinsic curvature influences loop topology and the distribution of topoisomers, and 3) that looping energy is influenced by operator orientation and separation. Finally, we note several limitations and extensions of our computational model.

Overall Effects of Sequence-dependent Intrinsic Curvature

First, sequence-dependent intrinsic curvature necessitates the consideration of eight distinct binding topologies, four of which are illustrated in Figure 7.3. As a result of intrinsic curvature and protein asymmetry, reversing the *order* of the binding domains yields loops with distinct topologies; for example, compare the loops for P1F (green) versus P1R (blue) in Figure 7.5(a). Second, sequence-dependent intrinsic curvature may greatly alter the topology of the loop relative to that predicted for homogeneous B-DNA. For the wild-type sequence, which has modest intrinsic curvature, one might not expect significant changes in writhe between loops that include or ignore this intrinsic curvature. This, however, is not always the case as seen for example in Figure 7.5(e) where the writhe of the A2F under-twisted loop (Wr = -0.34) (tri-nucleotide) has significantly greater magnitude than that of the A2 under-twisted loop (Wr = -0.08) (homogeneous B-DNA) that ignores intrinsic curvature. For the designed sequences, we do expect to see large changes in writhe due their significant intrinsic curvature. For example, the writhe of the P1R loops for the sequence 9C14 (Wr=0.15) in Figure 7.7(e) is less than one-half that of the control sequence (Wr = 0.37). The associated impact that these topological changes have on the energetics of looping can be substantial as discussed in detail below. Third, sequence-dependent intrinsic curvature *qualitatively* alters the distribution of twist along the inter-operator DNA. While the over- or under-twist remains *uniform* for the (homogeneous) model for the straight B-DNA, it becomes *non-uniform* for (non-homogeneous) models [43] that include intrinsic curvature, refer to Figure 7.5(c,d). This general observation may open further questions about possible sequence-dependent localization of over- and under-twist and its impact in biological processes, such as facilitating or impeding promoter melting.

Sequence-dependent Intrinsic Curvature Reduces Energetic Cost of Looping
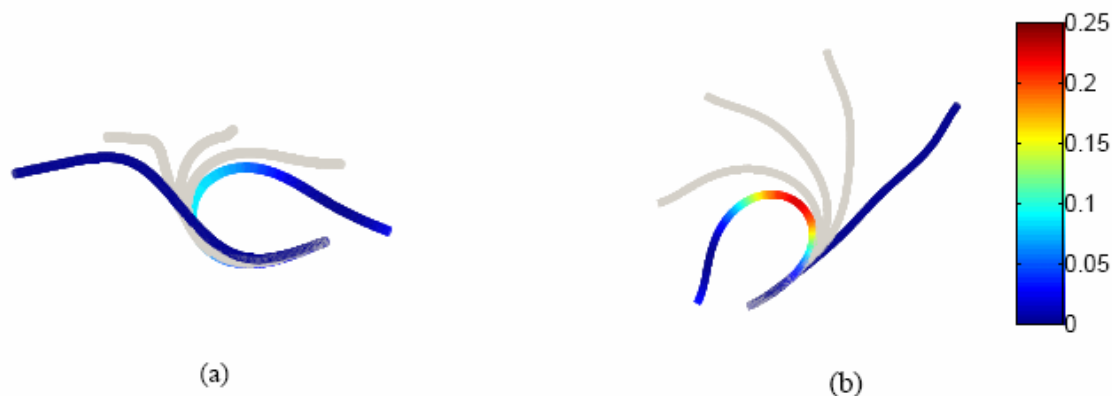
Figure 7.9 The transition from stress-free shape to looped conformation. The stress-free shapes are given in blue. The final loop geometries are shaded as a function of strain energy density (kT/bp). (a) 11C12 (b) control.

Our computations show that the addition of A-tract bends into the three designed sequences substantially reduces the loop elastic energy in comparison to that of control sequence; refer Figure 7.7(e). For example, an energy reduction of nearly 40% occurs between the minimum energy loop of the curved sequence 11C12 compared to that of the unbent control. Thus, we support the conclusion based on gel shift assays in [18], "Free energy cost can be decreased by incorporating designed DNA bends into looped complexes." Intuitively, one would expect that the sequence-dependent intrinsic curvature may conform (to some degree) to the final loop shape and particularly given the freedom afforded by eight binding topologies and the number of topoisomers occurring for each. Thus, as stated in [18], "the DNA whose initial structure most closely matches the optimum structure preferred by the LacI protein will form the most stable looped complex.". We can demonstrate this clearly by comparing the sequence 11C12 and the control sequence which exhibit the largest energy difference (11.93 kT versus 7.38 kT) as shown in Figure 7.9. Illustrated are the stress-free and (lowest energy) looped conformations for the sequence 11C12, Figure 7.9(a), and the control sequence, Figure 7.9(b), with the color scale indicating the strain energy density of the looped conformations. For the sequence 11C12, notice that modest twisting near the middle of the strand allows it to quickly conform to the looped configuration and with minimal strain energy (that is also dominated by twisting). By contrast, the nearly unbent control

requires substantial bending (largely planar) to arrive at the looped conformation and with significantly greater (bending) strain energy density in the middle portion.

The conclusion that sequence-dependent intrinsic curvature reduces loop energy is also supported by the computations for the wild-type sequence, though to a lesser degree. Observe from Figure 7.5(e) the 3% reduction in elastic energy of the minimum energy loop (highlighted in blue) that accounts for sequence-dependent intrinsic curvature from that of the minimum energy loop that ignores the intrinsic curvature (homogeneous B_DNA). The rather modest energy reduction in this example is expected given the very modest curvature of the stress-free shape compared to the straight B-DNA; refer to Figure 7.4(a)

Sequence-dependent Intrinsic Curvature Influences Loop Topology and Distribution of Topoisomers

The minimum energy loops computed for the wild-type sequence (Figure 7.5) and the designed sequences (Figure 7.7) reveal a wide range of binding and loop topologies. For example, note that the minimum energy loops for three sequences in Figure 7.7 (including the control sequence and the bent sequences 7C16, 9C14) are all *over-twisted,* while the minimum energy loops for one designed sequence 11C12 and the wild-type sequence are both *under-twisted*. These observations support findings from the gel shift assay experiments of [18] which state, "Designed DNA bends can also control the shape of a DNA loop formed by Lac repressor". Second, there are large variations in the preferred (minimum energy) binding topologies among the four designed and the wild-type sequences. This observation suggests that energetically-favorable binding topologies are in part determined by inter-operator sequence.

The sequence and associated intrinsic curvature may also strongly influence the distribution of topoisomers as suggested by the computed elastic energies reported in Figure 7.5 and Figure 7.7. For example, certain sequences exhibit only modest differences in elastic energy between the minimum and 2nd lowest energy loops. Only a 2% energy difference separates these states for the wild-type sequence when accounting

for the sequence-dependent intrinsic curvature; refer to Figure 7.5(e). Likewise, the analogous energy differences for the control and 9C14 sequences in Figure 7.7 are 5%. Thus, per the Boltzmann distribution, one may anticipate nearly equal concentrations of these topoisomers in experiments. By contrast, the 30% energy difference for the sequence 7C12 and 40% for 11C12 suggest substantially different topoisomer concentrations. Likewise a large (40%) energy difference separates the under-twisted (lower energy) from the over-twisted (higher energy) topoisomers of the wild-type sequence with P1 binding topology when the sequence-dependent intrinsic curvature is captured by the model; refer to Figure 7.5(e). However, when this sequence-dependent intrinsic curvature is ignored, the energy difference is substantially reduced (to 13%) suggesting a significantly different distribution of these topoisomers. Even for the other binding topologies, consideration of sequence-dependent intrinsic curvature, as observed in Figure 7.5(e), seems to substantially widen the gap between the energies of the two topoisomers in general.

Looping Energy: Roles of Operator Orientation and Separation

There is a considerable and expected overall reduction in the elastic energies of all of the lowest energy loops for the designed sequences relative to those of the wild-type. The four designed inter-operator sequences range from 144 bp (control) to 131 bp (7C16), and these longer inter-operator sequences relative to the wild-type (77 bp) lead to a far more flexible inter-operator DNA. For instance, elementary beam theory [59] predicts that the bending elastic energy E developed when bending an initially straight elastic beam of length L into a complete circle of radius $L/2\pi$ scales as $E \sim 1/L$. Thus, ignoring all other complications (e.g., coupled bending/torsion leading to three-dimensional deformation, non-uniform curvature, intrinsic curvature, etc.), a sequence of 77 bp requiring 34 kT to form a circular loop would then only require 17 kT to form (a larger diameter) loop if it were 154 bp long instead. This approximate 50% reduction in elastic energy is not unlike the large elastic energy reductions observed for the far more refined computations reported in Figure 7.5 and Figure 7.7.

As previously noted, adding (or subtracting) a single base-pair may alter the elastic energy through changing the length of inter-operator DNA by one unit of base-pair rise, and/or (b) the changing the relative orientation of the operators by one unit of base-pair twist. For the relatively long sequences of [18], the small differences in inter-operator lengths lead to negligible changes in elastic energy compared to the associated changes in the relative orientation of the two operators [57].

To understand this conclusion, refer again to Figure 7.8 which shows the elastic energy for the Control sequence (modeled as homogeneous B-DNA with the P1 binding topology). The energy computed by simply rotating one operator in increments of the base-pair twist (solid curves), closely approximate the energy (circles) computed when also allowing the inter-operator DNA to increase by increments of the base-pair rise. This close agreement between these two calculations provides strong support for the claim that *changes in operator orientation* brought about by adding/subtracting base-pairs have a far greater influence on loop energy than the associated *changes in length of the inter-operator DNA*. This conclusion also supports the experimental finding in [57] as discussed in [18], "The *in vivo* probability of loop formation depends strongly on the torsional phasing of the operators but relatively weakly on their separation".

Note also the obvious periodic variation in elastic energy illustrated in Figure 7.8. This computed result using rod theory supports the experimental observations that looping probability is a periodic function of the inter-operator distance [20, 21, 60]. The period of 10.5 bp corresponds to a complete helical turn of DNA and, the results of Figure 7.8 demonstrate that specific helical orientations of the operators may significantly reduce the energetic cost of loop formation by up to 50%.

Model Limitations and Extensions

The energy computations herein are solely restricted to the elastic (or 'strain') energy of the loop. To assess thermal stability, one needs to determine the free energy difference between looped and unlooped states. Major contributions to the free energy include: (1)

loop elastic energy, (2) protein deformation energy, (3) entropy, (4) DNA-protein surface binding energy, and (5) electrostatic potential between the negatively charged phosphates in the DNA backbone. Of these, we believe that entropy and the surface binding energy would remain relatively constant for variations within a class of sequences (i.e., for topoisomers of the wild-type or for topoisomers of the designed sequences considered herein). By contrast, contributions from the loop and protein deformation energies may vary significantly and, as a result of associated conformation changes, so might the electrostatic repulsion. For instance, the binding co-operativity of the two operator sites depends on their electrostatic repulsion [61] which decays exponentially with operator separation per the Debye-Hückel approximation (or other approximations discussed in Appendix 3). Some of these additional influences could, in fact, be approximated in the context of a computational rod model for DNA.

For example, the formulation herein tacitly assumes a rigid protein as determined from the crystal structure. However, the effects of protein flexibility on the loop could be captured by replacing the fixed (Dirichlet) boundary-conditions with elastic (mixed Neumann-Dirichlet) boundary conditions that model the equivalent flexibility at the DNA-protein interface. Molecular dynamics (MD) simulations have suggested that flexibility of the LacR derives primarily from the head regions [35] while the possibility of flexibility in the V-region has also been suggested in prior studies [41, 42]. Similarly, the entire Lac-R might also be approximated by a small number of rigid bodies with concentrated flexibility (stiffness) at the V-region and at the protein heads. Coupling this 'low-dimensional' protein model with elastic rod model of DNA would allow one to capture the elastic deformation of the entire protein/DNA complex in an approximate manner. This might provide initial conditions for MD simulations of the complex or possibly obviate the need for full MD simulations altogether [35].

It is recognized that any long-length scale material law for DNA will surely influence the loop topology and elastic energy computed from rod theory and that further advances in determining accurate material laws are likely to follow from single-molecule experiments and MD simulations. For instance, recent MD simulations [9, 12, 15] have begun to

reveal the sequence-dependent stiffness parameters for linear elastic behavior, while other studies [13, 14, 40] have begun to explore nonlinear (and inelastic) behavior, though this has also been questioned [39]. It is also recognized that DNA must exhibit a strong coupling between twist and extension [62] due to its chiral (helical) construction [63] and this requires a modification of the material law used herein as proposed in Chapter 5. Overall, the sequence-dependent bending and torsional stiffnesses affect computed properties of the Lac-repressor loop [7-14] and these can also be accommodated herein by accounting for spatial variations in the stiffness tensor $B(s)$ employed in Eq. (7.1); see, for example the problem set up in Chapter 6. Likewise, the sequence-dependent stress-free shape (or `intrinsic curvature') surely affects the mechanics of looping for the LacR-DNA complex and the results herein suggest its dominant role for the sequences with designed A-tract bends.

Conclusions

This chapter employs the computational rod model for the long-length scale structure of DNA as a means to explore the mechanics of protein-mediated DNA looping. Our specific objective is to understand how looping energy and topology are influenced by the sequence-dependent intrinsic curvature of the substrate DNA. We adopt the lactose repressor (LacR) protein-DNA complex as our example and consider both the wild-type sequence possessing relatively little intrinsic curvature and the highly curved sequences with designed A-tract bends introduced by Mehta and Kahn [18]. Our method uses the known sequence of the inter-operator DNA to construct the intrinsic curvature of the helical axis as input to the computational rod model. Simulations allow us to predict the elastic (strain) energy required to transform the stress-free conformation into a looped conformation that complies with the known LacR-operator crystal structure. Numerical studies of loop energetics and topology reveal the following major influences of sequence-dependent intrinsic curvature on the LacR-DNA complex. First, the highly curved sequences of [18] tend to lower the energetic cost of looping, widen the energy distribution among stable and meta-stable loops, and substantially alter loop topology. Qualitatively, the inclusion of sequence-dependent intrinsic curvature also leads to non-uniform twist (or twist deficit) [43] and necessitates consideration of eight distinct

binding topologies from the known crystal structure of the LacR complex. The generality and several extensions of the computational rod model are also discussed for other looping and non-looping behaviors of DNA.

References:

1. Semsey, S., K. Virnik, and S. Adhya, *A gamut of loops: meandering DNA.* Trends in Biochemical Sciences, 2005. **30**(6): p. 334-341.
2. Schleif, R., *DNA Looping.* Annual Review of Biochemistry, 1992. **61**: p. 199-223.
3. Ptashne, M. and A. Gann, *Genes and Signals.* 1 ed. 2002, Cold Spring Harbor, N.Y.: Cold Spring Harbor Laboratory Press.
4. Gabrielian, A. and S. Pongor, *Correlation of intrinsic DNA curvature with DNA property periodicity.* Febs Letters, 1996. **393**(1): p. 65-68.
5. Munteanu, M.G., et al., *Rod models of DNA: sequence-dependent anisotropic elastic modelling of local bending phenomena.* Trends in Biochemical Sciences, 1998. **23**(9): p. 341-347.
6. Lewis, M., et al., *Crystal structure of the lactose operon repressor and its complexes with DNA and inducer.* Science, 1996. **271**(5253): p. 1247-1254.
7. Coleman, B.D., W.K. Olson, and D. Swigon, *Theory of sequence-dependent DNA elasticity.* Journal of Chemical Physics, 2003. **118**(15): p. 7127-7140.
8. Olson, W.K., et al., *DNA sequence-dependent deformability deduced from protein-DNA crystal complexes.* Proceedings of the National Academy of Sciences of the United States of America, 1998. **95**(19): p. 11163-11168.
9. Beveridge, D.L., et al., *Molecular dynamics simulations of the 136 unique tetranucleotide sequences of DNA oligonucleotides. I. Research design and results on d(C(p)G) steps.* Biophysical Journal, 2004. **87**(6): p. 3799-3813.
10. Manning, R.S., J.H. Maddocks, and J.D. Kahn, *A continuum rod model of sequence-dependent DNA structure.* Journal Of Chemical Physics, 1996. **105**(13): p. 5626-5646.
11. Olson, W.K., D. Swigon, and B.D. Coleman, *Implications of the dependence of the elastic properties of DNA on nucleotide sequence.* Philosophical Transactions of the Royal Society of London Series A-Mathematical Physical and Engineering Sciences, 2004. **362**(1820): p. 1403-1422.
12. Lankas, F., *DNA sequence-dependent deformability - Insights from computer simulations.* Biopolymers, 2004. **73**(3): p. 327-339.
13. Cloutier, T.E. and J. Widom, *DNA twisting flexibility and the formation of sharply looped protein-DNA complexes.* Proceedings of the National Academy of Sciences of the United States of America, 2005. **102**(10): p. 3645-3650.
14. Cloutier, T.E. and J. Widom, *Spontaneous sharp bending of double-stranded DNA.* Molecular Cell, 2004. **14**(3): p. 355-362.
15. Dixit, S.B., et al., *Molecular dynamics simulations of the 136 unique tetranucleotide sequences of DNA oligonucleotides. II: Sequence context effects on the dynamical structures of the 10 unique dinucleotide steps.* Biophysical Journal, 2005. **89**(6): p. 3721-3740.
16. Edelman, L.M., R. Cheong, and J.D. Kahn, *Fluorescence resonance energy transfer over similar to 130 basepairs in hyperstable Lac repressor-DNA loops.* Biophysical Journal, 2003. **84**(2): p. 1131-1145.
17. Morgan, M.A., et al., *Single-molecule spectroscopic determination of Lac repressor-DNA loop conformation.* Biophysical Journal, 2005. **89**(4): p. 2588-2596.

18. Mehta, R.A. and J.D. Kahn, *Designed hyperstable lac repressor center dot DNA loop topologies suggest alternative loop geometries.* Journal Of Molecular Biology, 1999. **294**(1): p. 67-77.

19. Geanacopoulos, M., et al., *Gal repressosome contains an antiparallel DNA loop.* Nature Structural Biology, 2001. **8**(5): p. 432-436.

20. Lewis, D.E.A. and S. Adhya, *In Vitro Repression of the gal Promoters by GalR and HU Depends on the Proper Helical Phasing of the Two Operators.* J. Biol. Chem., 2002. **277**(4): p. 2498-2504.

21. Dunn, T.M., et al., *An Operator at -280 Base-Pairs That Is Required for Repression of Arabad Operon Promoter - Addition of DNA Helical Turns between the Operator and Promoter Cyclically Hinders Repression.* Proceedings of the National Academy of Sciences of the United States of America-Biological Sciences, 1984. **81**(16): p. 5017-5020.

22. Watson, M.A., D.M. Gowers, and S.E. Halford, *Alternative geometries of DNA looping: an analysis using the SfiI endonuclease.* Journal of Molecular Biology, 2000. **298**(3): p. 461-475.

23. Embleton, M.L., A.V. Vologodskii, and S.E. Halford, *Dynamics of DNA loop capture by the sfiI restriction endonuclease on supercoiled and relaxed DNA.* Journal of Molecular Biology, 2004. **339**(1): p. 53-66.

24. Schulz, A., J. Langowski, and K. Rippe, *The effect of the DNA conformation on the rate of NtrC activated transcription of Escherichia coli RNA polymerase.sigma(54) holoenzyme.* Journal of Molecular Biology, 2000. **300**(4): p. 709-725.

25. Zhang, Y.L. and D.M. Crothers, *Statistical mechanics of sequence-dependent circular DNA and its application for DNA cyclization.* Biophysical Journal, 2003. **84**(1): p. 136-153.

26. Merlitz, H., et al., *Looping Dynamics of Linear DNA Molecules and the Effect of DNA Curvature: A Study by Brownian Dynamics Simulation.* Biophysical Journal, 1998. **74**(2): p. 773-779.

27. Rippe, K., P.H. von Hippel, and J. Langowski, *Action at a Distance - DNA-Looping and Initiation of Transcription.* Trends in Biochemical Sciences, 1995. **20**(12): p. 500-506.

28. Olson, W.K., *Simulating DNA at low resolution.* Current Opinion in Structural Biology, 1996. **6**(2): p. 242-256.

29. Schlick, T., *Modeling Superhelical DNA - Recent Analytical And Dynamic Approaches.* Current Opinion In Structural Biology, 1995. **5**(2): p. 245-262.

30. Balaeff, A., et al., *Modelling DNA loops using continuum and statistical mechanics.* Philosophical Transactions of the Royal Society of London Series A-Mathematical Physical and Engineering Sciences, 2004. **362**(1820): p. 1355-1371.

31. Balaeff, A., L. Mahadevan, and K. Schulten, *Elastic rod model of a DNA loop in the lac operon.* Physical Review Letters, 1999. **83**(23): p. 4900-4903.

32. Balaeff, A., L. Mahadevan, and K. Schulten, *Structural Basis for Cooperative DNA Binding by CAP and Lac Repressor.* Structure, 2004. **12**(1): p. 123-132.

33. Villa, E., et al., *Multiscale method for simulating protein-DNA complexes.* Multiscale Modeling & Simulation, 2004. **2**(4): p. 527-553.

34. Balaeff, A., L. Mahadevan, and K. Schulten, *Modeling DNA loops using the theory of elasticity.* Physical Review E, Submitted 2005.

35. Villa, E., A. Balaeff, and K. Schulten, *Structural dynamics of the lac repressor-DNA complex revealed by a multiscale simulation.* Proceedings of the National Academy of Sciences of the United States of America, 2005. **102**(19): p. 6783-6788.

36. Baumann, C.G., et al., *Ionic effects on the elasticity of single DNA molecules.* Proceedings of the National Academy of Sciences of the United States of America, 1997. **94**(12): p. 6185-6190.

37. Hagerman, P.J., *Flexibility of DNA.* Annual Review of Biophysics and Biophysical Chemistry, 1988. **17**: p. 265-286.

38. Strick, T.R., et al., *The elasticity of a single supercoiled DNA molecule.* Science, 1996. **271**(5257): p. 1835-1837.

39. Du, Q., et al., *Cyclization of short DNA fragments and bending fluctuations of the double helix.* Proceedings of the National Academy of Sciences of the United States of America, 2005. **102**(15): p. 5397-5402.

40. Wiggins, P.A., R. Phillips, and P.C. Nelson, *Exact theory of kinkable elastic polymers.* Physical Review E, 2005. **71**(2).

41. Friedman, A.M., T.O. Fischmann, and T.A. Steitz, *Crystal-Structure of Lac Repressor Core Tetramer and Its Implications for DNA Looping.* Science, 1995. **268**(5218): p. 1721-1727.

42. Ruben, G.C. and T.B. Roos, *Conformation of Lac repressor tetramer in solution, bound and unbound to operator DNA.* Microscopy Research and Technique, 1997. **36**(5): p. 400-416.

43. Tobias, I. and W.K. Olson, *The Effect of Intrinsic Curvature on Supercoiling - Predictions of Elasticity Theory.* Biopolymers, 1993. **33**(4): p. 639-646.

44. Strick, T., et al., *Twisting and stretching single DNA molecules.* Progress in Biophysics & Molecular Biology, 2000. **74**(1-2): p. 115-140.

45. Bustamante, C., et al., *Entropic Elasticity of Lambda-Phage DNA.* Science, 1994. **265**(5178): p. 1599-1600.

46. Bryant, Z., et al., *Structural transitions and elasticity from torque measurements on DNA.* Nature, 2003. **424**(6946): p. 338-341.

47. Bustamante, C., Z. Bryant, and S.B. Smith, *Ten years of tension: single-molecule DNA mechanics.* Nature, 2003. **421**(6921): p. 423-427.

48. Olson, W.K. and V.B. Zhurkin, *Modeling DNA deformations.* Current Opinion in Structural Biology, 2000. **10**(3): p. 286-297.

49. Tobias, I., D. Swigon, and B.D. Coleman, *Elastic stability of DNA configurations. I. General theory.* Physical Review E (Statistical Physics, Plasmas, Fluids, and Related Interdisciplinary Topics), 2000. **61**(1): p. 747-758.

50. Coleman, B.D., D. Swigon, and I. Tobias, *Elastic stability of DNA configurations. II. Supercoiled plasmids with self-contact.* Physical Review E (Statistical Physics, Plasmas, Fluids, and Related Interdisciplinary Topics), 2000. **61**(1): p. 759-770.

51. Kehrbaum, S. and J.H. Maddocks. *Effective Properties of Elastic Rods with High Intrinsic Twist.* in *16th IMACS World Congress.* 2000.

52. Rey, S. and J.H. Maddocks. *Buckling of an Elastic Rod with High Intrinsic Twist.* in *16th IMACS World Congress.* 2000.

53. Berman, H.M., et al., *The Protein Data Bank.* Nucleic Acids Research, 2000. **28**(1): p. 235-242.

54. Alexander, J.C. and S.S. Antman, *The Ambiguous Twist of Love.* Quarterly of Applied Mathematics, 1982. **40**(1): p. 83-92.

55. Olson, W.K., et al., *A standard reference frame for the description of nucleic acid base-pair geometry.* Journal of Molecular Biology, 2001. **313**(1): p. 229-237.

56. Stoker, J.J., *Differential geometry.* 1969, New York: Wiley-Interscience.

57. Bellomy, G.R., M.C. Mossing, and M.T. Record, *Physical-Properties of DNA In-vivo as Probed by the Length Dependence of the Lac Operator Looping Process.* Biochemistry, 1988. **27**(11): p. 3900-3906.

58. Klenin, K. and J. Langowski, *Computation of writhe in modeling of supercoiled DNA.* Biopolymers, 2000. **54**(5): p. 307-317.

59. Timoshenko, S.P. and J.M. Gere, *Theory of Elastic Stability.* 2 ed. 1961, New York: McGraw-Hill.

60. Muller, J., S. Oehler, and B. Muller-Hill, *Repression of Lac-I Promoter as a Function of Distance, Phase and Quality of an Auxiliary lac Operator.* Journal of Molecular Biology, 1996. **257**(1): p. 21-29.

61. Levandoski, M.M., et al., *Cooperative and anticooperative effects in binding of the first and second plasmid O-sym operators to a Lacl tetramer: Evidence for contributions of non-operator DNA binding by wrapping and looping.* Journal of Molecular Biology, 1996. **260**(5): p. 697-717.

62. Marko, J.F., *Stretching must twist DNA.* Europhysics Letters, 1997. **38**(3): p. 183-188.

63. Healey, T.J., *Material symmetry and chirality in nonlinearly elastic rods.* Mathematics And Mechanics Of Solids, 2002. **7**(4): p. 405-420.

Chapter 8

Summary, Conclusions and Future Work

8.1 Summary and Major Conclusions

This dissertation contributes a versatile computational rod model that describes the nonlinear dynamics of highly contorted cables, DNA, and other filament-like structures, including the mechanics of looping and intertwining. Our formulation is first carefully benchmarked by comparing our dynamical solutions with known equilibrium solutions for limiting cases of slow (quasi-static) loading. We then employ our computational model in four case studies that explore the hockling and tangling of underwater cables and the supercoiling and looping of DNA. The scope and the major conclusions from each of these case studies are presently summarized.

- **Benchmarking Study and Dynamics**

As a first example, we elected to carefully benchmark our dynamical solutions with known equilibrium solutions for limiting cases of slow (quasi-static) loading. Doing so highlights the accuracy of our formulation. We refer to Heijden et al. [1] who catalogues the equilibria and bifurcations of clamped-clamped rods which in turn have been validated by laboratory-scale experiments on nitinol rods. The dynamic rod model summarized in Chapter 4 not only reproduces these equilibria under quasi-static loading but also captures large dynamic transitions between equilibrium paths. In addition, we discover new hysteresis effects that result from our dynamical treatment.

Dynamics of underwater cable is dominated by inertia (high Reynolds number), while *dynamics* of DNA it is dominated by viscous effects (low Reynolds number). The

importance of modeling *dynamics* is well recognized for underwater cable applications, but not nearly as well recognized or understood in the context of DNA mechanics. We identified at least three reasons for which one might want to formulate *dynamics* in either application. First, the inclusion of *dynamics* in the rod model formulated herein makes it possible to study nonlinear *dynamic* transitions between equilibria as illustrated by the 'figure eight transition' path in Section 4.2.1 of Chapter 4. Such transitions may help explain how small thermal fluctuations in DNA can initiate large changes in its supercoiled states. Second, in the *dynamic* rod formulation, we circumvent all *unstable* equilibria simply by perturbing the rod with a negligibly small random flow. Thus, the solutions dynamically relax only to stable equilibria. By contrast, *equilibrium* rod theory yields both stable and unstable equilibria and require a subsequent analysis of equilibrium stability. Third, the hysteresis observed near equilibria bifurcations in Section 4.3 signifies the role of *dynamic* lag. Also recognize that the first two reasons are independent from the goal of *quantitative* modeling of the *time-scales* of the nonlinear *dynamics*. In other words, even an artificial choice of inertia and drag coefficients serves the purpose of the first two reasons. However, the value of the third reason really depends on the quantitative modeling of *dynamic* effects which for DNA would mainly require the quantitative modeling of drag coefficients (low Reynolds number).

- **Tension-Torque Coupling**

As a second example, we study in Chapter 5 the influence of chirality by adding tension-torque coupling to the rod constitutive law. This coupling is motivated by the helically-wound construction of common wire and synthetic cables as well as the DNA duplex. In contrast to isotropic rods, the behavior of a chiral rod differs from that of its mirror image [2]. To distinguish it from the anisotropy in bending, Healey [2] describes chiral anisotropy as 'hemitropy'. In an isotropic rod, the torsional moment at any cross-section is proportional to twist in the rod. However, in a chiral (or 'hemitropic') rod, tension also induces a torsional moment[28] at any cross-section due to its helical construction. In terms of kinematic quantities, this is equivalent to 'twist-extension coupling' and it is this

---

[28] For marine cable applications, this motivates the need to design so-called "torque-balanced" cables by using constructions that incorporate both left-handed and right-handed helical winds.

observation that is central to the paper titled "Stretching must twist DNA" by Marko [3]. The impact of this coupling is highlighted through new solutions to the benchmark problem first introduced in Chapter 4.

The analytical and numerical results presented in this chapter demonstrate that tension-torque coupling can have pronounced influences on the bifurcations of rod equilibria and on the mechanics of loop formation. The major influences noted in these results are that tension-torque coupling may:

6. substantially alter loop topology,
7. introduce non-uniform twist (or untwist),
8. change the stress in the rod and reaction forces and moments at the boundaries,
9. alter the equilibrium bifurcation characteristics, and
10. soften the rod due to off-diagonal coupling terms in the stiffness matrix.

- **Dynamics of Self-Contact and Intertwining**

As a third example, we model in Chapter 6 the self-contact so as to capture the dynamic evolution of intertwining in response to torsional buckling. Modeling self-contact in rods is a pre-requisite for the simulation of cable intertwining, hockling and knot formation; yet it has been a significant research challenges in rod theory. The intertwined shapes resemble hockles in underwater cables and plectonemes (one type of supercoils) in DNA.

In Chapter 6, we presented numerical solutions for an example system of a rod subjected to increasing twist at one end. The solutions show the dynamic evolution of the rod from an initially straight element, through a buckled element in the approximate form of a helix, through the dynamic collapse of this helix into a loop, and subsequent intertwining of the loop with multiple sites of self-contact. These results highlight the importance of torsion as a dominant mechanism responsible for hockles and plectonemes.

- **Protein-Mediated DNA Looping**

Looping in DNA is an important mechanism for gene regulation. Gene expression can be regulated by specific proteins that deform DNA into a loop. One of the most studied examples of this regulation is the Lac gene in the bacterium *E.Coli* that is mechano-chemically controlled by 'Lactose-Repressor' protein. In chapter 7, we employ the rod model to simulate DNA looping mediated by 'Lactose-Repressor' for both the 'wild-type' (naturally occurring) DNA sequence and variety of other 'designed sequences' with large intrinsic bends.

The computations provide a fundamental understanding of the energetics and topology the DNA loops. They also elucidate experimentally observable trends of looping rates and stability of the designed sequences and the overall influence of sequence-dependent instrinsic curvature in the looping process. Numerical studies of loop energetics and topology reveal the following major influences of sequence-dependent intrinsic curvature on the LacR-DNA complex. First, the highly curved sequences tend to lower the energetic cost of looping, widen the energy distribution among stable and meta-stable loops, and substantially alter loop topology. Qualitatively, the inclusion of sequence-dependent intrinsic curvature also leads to non-uniform twist (or twist deficit) and necessitates consideration of eight distinct binding topologies from the known crystal structure of the LacR complex.

This dissertation is an important, yet modest step towards the goal of understanding DNA-protein interactions. Many scientific challenges remain in both experimental and computational research to accomplish this ambitious goal. Understanding these challenges, we conclude by laying out some future research directions based upon the computational framework contributed by this dissertation.

8.2 Future Work on DNA

8.2.1 Structural Characterization of DNA

The structural properties of DNA (e.g., sequence-dependent stiffness, intrinsic curvature, tension-torque coupling, etc.) are not yet well-characterized by experimental measurments due to many experimental challenges at the single molecule level. Therefore the structural parameters that are inputs to our computational framework are subject to debate. But the simulation results from our computational framework also offer insights into the design of experiments that could test the validity of mechanical models of DNA. Ideally, one seeks to design experiments guided by model simulations that dovetail well with current experimental capabilities.

An example[29] of such a simulation study is illustrated in Figure 8.1 in the context of LacR-DNA complex described in Chapter 7. This work builds upon the known influence of the inter-operator phasing, now extending to operator-A-tract phasing. By conducting a parametric study of the effect of the two helical phases, our model can deduce the phase-loop energy relationship and thus ultimately predict the probability distributions of various loop topologies. By comparing our theoretical predictions with published experimental results we expect to better characterize the structural parameters for our model.

---

[29] This is an ongoing work in collaboration with Todd Lillian. See acknowledgements.
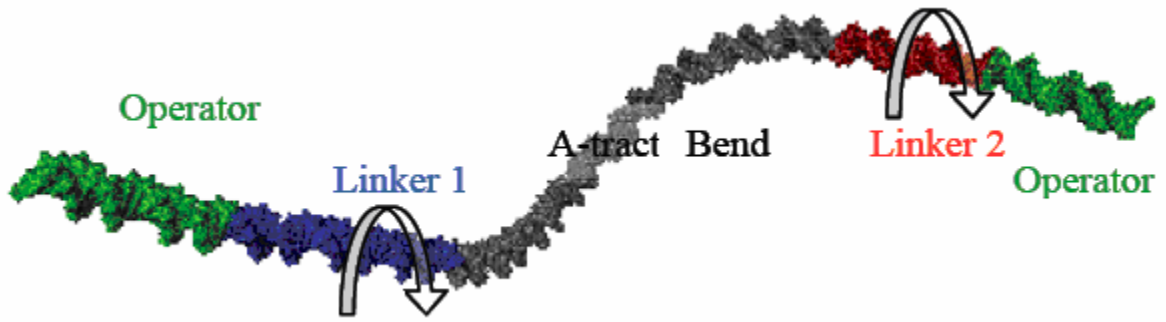
(a)
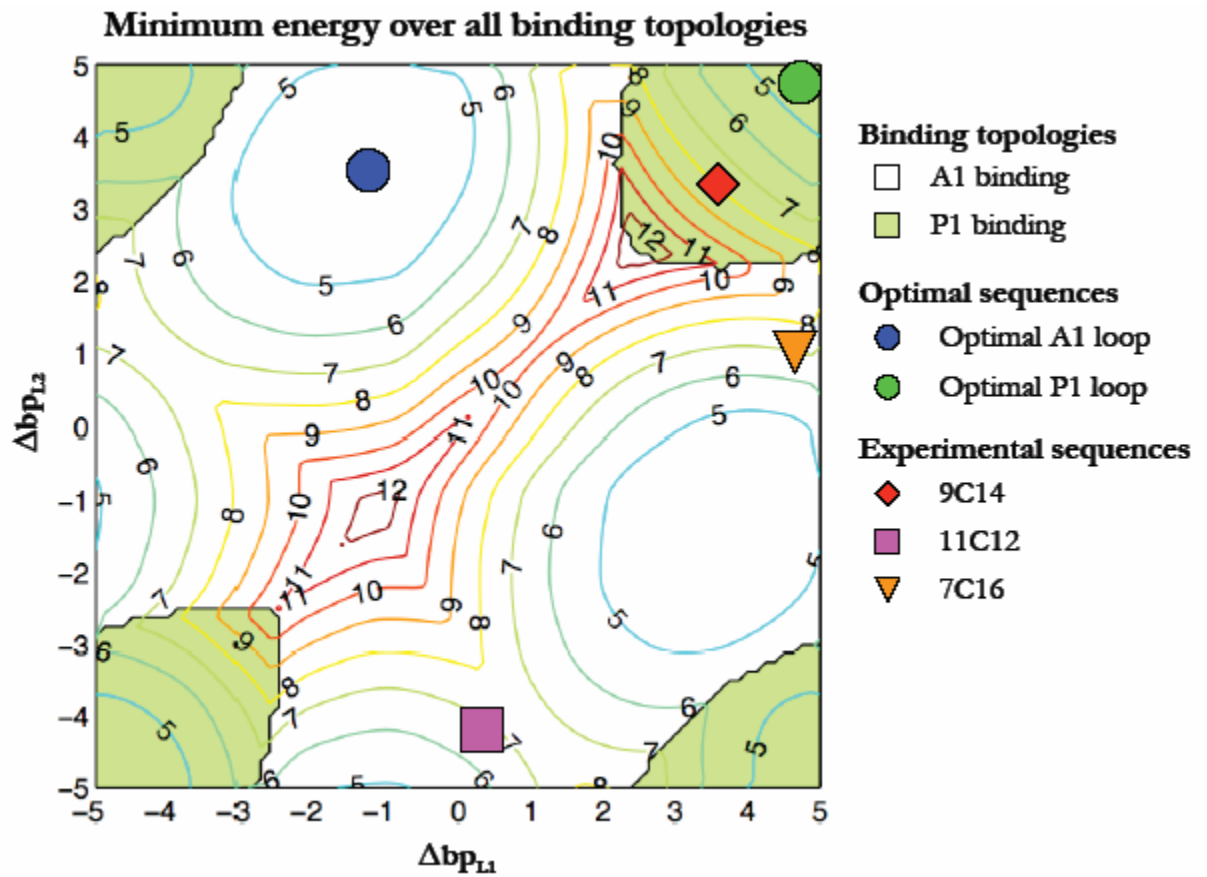
(b)

Figure 8.1 (a) Adding/ subtracting basepairs in straight 'Linker' regions changes helical phasing between operator and A-tract bend. (b) Contour maps of DNA loop energy in LacR complex parameterized over the helical phasings (in Δbp) introduced at the two linkers.

8.2.2 Modeling Entropic Effects

Figure 8.2 First two normal modes of a LacR-DNA loop.

It was argued in Chapter 7 that the free energy cost of DNA looping might have a noticeable contribution from entropy (due to thermal fluctuations of DNA). We can extend the rod model to capture thermal fluctuations (entropy) of DNA strands and DNA-protein complexes by using normal modes. An example[30] of a normal mode analysis is illustrated in Figure 8.2 for a LacR loop. The equilibrium shape of inter-operator DNA loop is first computed from our computational rod model. We then calculate linear fluctuations of the DNA loop about its equilibrium shape from the Hamiltonian of the system. The entropy ultimately depends on the stiffness (matrix) of the looped DNA. We may further extend this concept to evaluate the entropy of the entire DNA-protein complex by using standard techniques of 'flexible multi-body dynamics' (FMBD) such as 'component mode synthesis' perhaps in combination by an initial MD analysis of the protein.

---

[30] This is an ongoing work in collaboration with David Wilson. See acknowledgements.

8.2.3 Coupling of Protein Flexibility/ Dynamics

As noted in Chapter 7, very little is understood about the deformability of the proteins that control structural changes in DNA. The current Molecular Dynamics (MD) software remains computationally inefficient (if not unusable) when applied to the long time and length scale simulations of DNA-protein interactions. Interestingly, computational tools from mechanical engineering and belonging to the fast-developing research area of flexible multi-body dynamics (FMBD) could be adapted to model proteins. MD tools could be interfaced with FMBD tools using multi-scale modeling techniques to yield potentially dramatic improvements in both computational speed and accuracy.

8.2.4 Histone Unwrapping
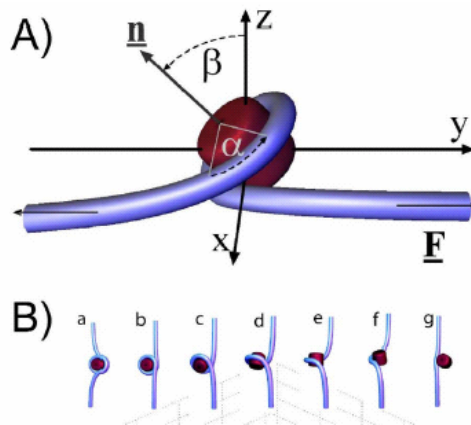
Figure 8.3 DNA (blue) unwrapping from histone (red) (Courtesy: Kulic and Schiessel [4])

Long DNA in "eukaryotes" (higher organisms) are packed inside the cell nucleus by wrapping around spool-shaped proteins called "histones" [5]. The unwrapping of DNA under tension is known to be a quantized phenomenon [6-8] and this can be explained by considering the energy barriers during unwrapping [4]. To some extent, this requires overcoming a DNA-histone adsorption potential, and to a much greater extent the bending energy barrier as the wrapped loop tends to rotate out of plane (i.e., tends to unwrap) as shown in Figure 8.3. The wrapping and unwrapping of DNA on histone spools may be an excellent problem to address using our computational rod model due to

130

the relatively large strain energy involved in this process compared to thermal energy. Moreover, through our prior case study of intertwining, we already have formalized a similar "contact" problem that can now be modified for this type of study.

References:

1. van der Heijden, G.H.M., et al., *Instability and self-contact phenomena in the writhing of clamped rods.* International Journal Of Mechanical Sciences, 2003. **45**(1): p. 161-196.

2. Healey, T.J., *Material symmetry and chirality in nonlinearly elastic rods.* Mathematics And Mechanics Of Solids, 2002. **7**(4): p. 405-420.

3. Marko, J.F., *Stretching must twist DNA.* Europhysics Letters, 1997. **38**(3): p. 183-188.

4. Kulic, I.M. and H. Schiessel, *DNA spools under tension.* Physical Review Letters, 2004. **92**(22).

5. Richmond, T.J. and C.A. Davey, *The structure of DNA in the nucleosome core.* Nature, 2003. **423**(6936): p. 145-150.

6. Baumann, C.G., et al., *Stretching of single collapsed DNA molecules.* Biophysical Journal, 2000. **78**(4): p. 1965-1978.

7. Brower-Toland, B.D., et al., *Mechanical disruption of individual nucleosomes reveals a reversible multistage release of DNA.* Proceedings Of The National Academy Of Sciences Of The United States Of America, 2002. **99**(4): p. 1960-1965.

8. Murayama, Y., Y. Sakamaki, and M. Sano, *Elastic response of single DNA molecules exhibits a reentrant collapsing transition.* Physical Review Letters, 2003. **90**(1).

Appendices

Appendix 1: Further Comments on DNA Structure and Function
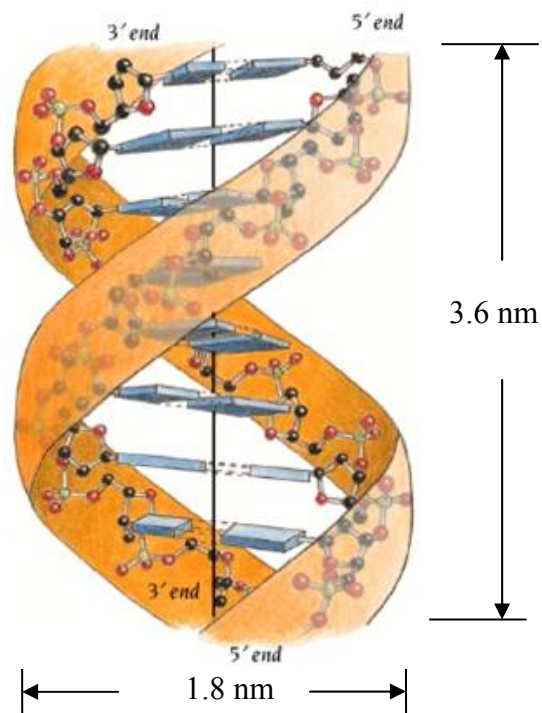
Figure A 1.1 DNA shown as a helical coil of two strands. Each strand is made up of sugar-phosphate backbone (orange ribbons) and bases (blue planks) enclosed inside the helix. (Courtesy: Brandem and Tooze [1]).

A schematic of a DNA polymer is shown in Figure A 1.1. It consists of two strands which coil around each other to form a double helix. Each strand is a series of units called "nucleotides". There are four different kinds of nucleotides called adenine, guanine, cytosine and thymine, or simply A, G, C and T. Their sequence ciphers the genetic information in DNA. Each nucleotide is itself made up of three parts – sugar, phosphate and base. The four kinds of nucleotides only differ in their bases. The sugars and

phosphates form the polymer chain of the strand while the bases branch from the sugars and function like a coding alphabet for genes.

DNA lengths vary from a few micrometers to centimeters. A long length of the DNA double helix packs into the small confines of the cell nucleus (or a virus) by wrapping upon itself or around spool-shaped proteins (called 'histones') in an organized manner. This wrapping of the DNA double helix is called "supercoiling" to distinguish it from the helical coiling of two constituent strands. Two kinds of supercoiling in DNA, plectonemic and solenoidal, are illustrated in Figure A 1.2. Solenoidal supercoils achieve higher compaction as described in Lehninger et al. [2].
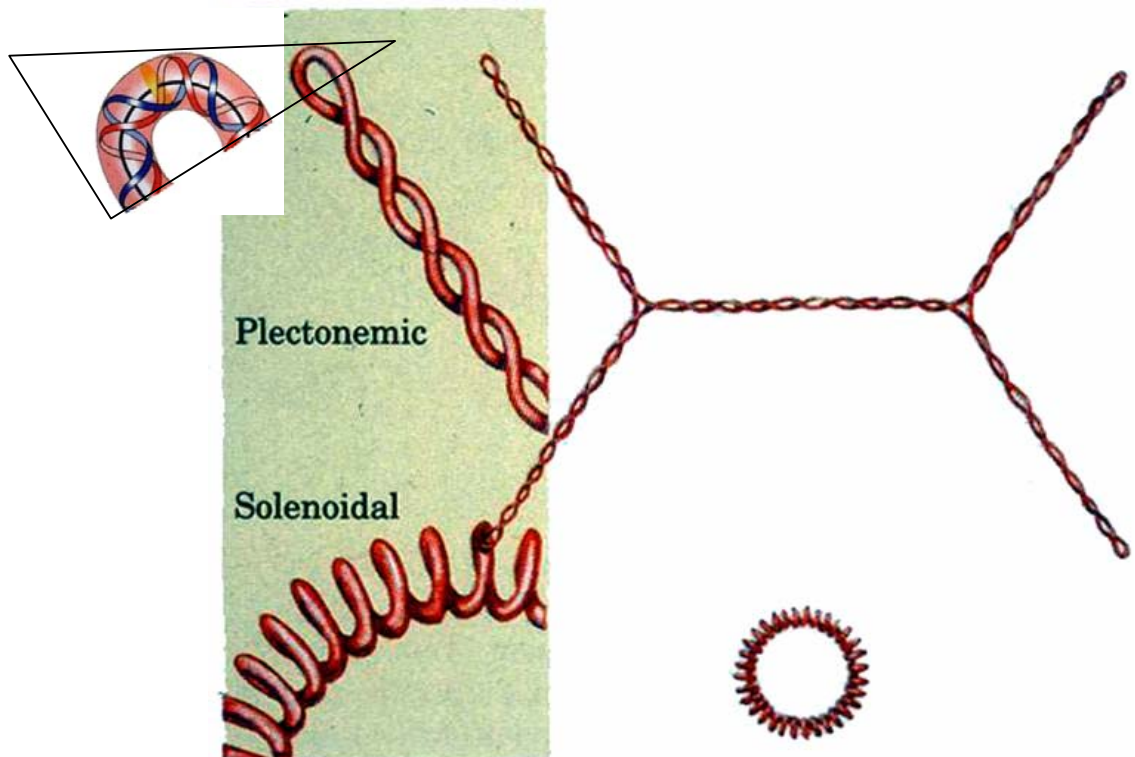
Figure A 1.2 Two types of supercoiling of the same length of DNA, drawn to scale. Though the solenoidal form achieves greater compaction (as needed for packaging it inside a cell nucleus) than does the plectonemic form, it is generally not observed unless stabilized by certain proteins (e.g. histones). For isolated DNA in solution, the plectonemic form is stable and is mostly observed in the laboratory. (Courtesy: Lehninger et al. [2]).

How do genes control behavior of a cell or an organism?

All vital cellular processes result from the functions of various proteins (e.g. enzymes) which themselves are copolymers of twenty different types of units called amino acids (or twenty 'standard' amino acids). Genes encode the amino acid sequence of all proteins. To make a protein from amino acids, cellular machinery has to 'read' the base sequence in DNA through a process called 'transcription' and the successful formation of proteins concludes the process of 'gene expression'. In order to inherit genes in newly formed cells, DNA makes its own copies through a process called 'replication' that again requires 'reading' of the base sequence.

How can base sequences be replicated?

The base-pairing in the two chains is unique as suggested by Watson and Crick [3, 4], i.e. A pairs up with T and G pairs up with C. This unique pairing explains that if a single strand of DNA is left in a solution of nucleotides, it will form its (unique) complimentary strand. Therefore to replicate DNA, one simply needs to separate the two strands and supply free nucleotides.

How is transcription or replication controlled?

Twisting and writhing (or curving) of the DNA double helix are the two fundamental mechanisms that control transcription and replication through the actions of proteins (called 'polymerases') that access the base sequence. Note, however, that DNA exists in an aqueous environment and the bases, which are hydrophobic, remain enclosed within the double helical envelop of the two sugar-phosphate chains, which are hydrophilic. The DNA double helix must then partially 'unravel' in the regions accessed by polymerase proteins to 'expose' the base pairs.
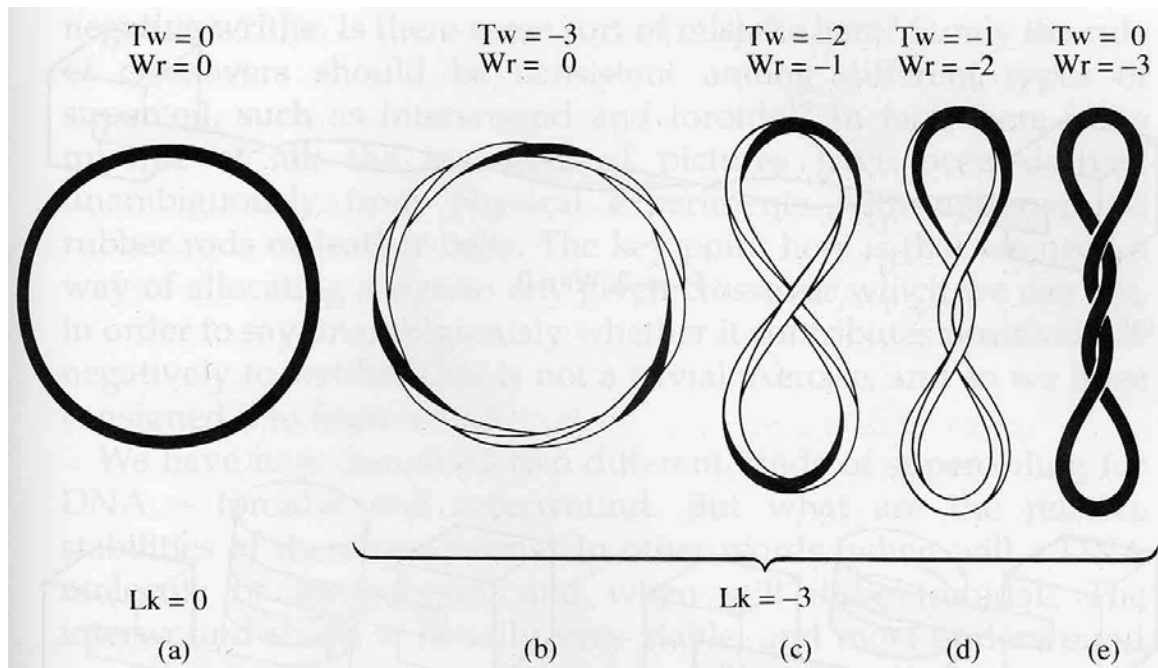
Figure A 1.3 The linking number in the left-most cable loop is 0 and in the next loop it is -3. The twist is converted to successively greater writhe in the remaining loops. (Courtesy: Calladine et al. [5]).

Twist and writhe do not vary independently in any filament whose ends are restrained. For example, the filaments shown in Figure A 1.3 and Figure A 1.4 conserve the sum of twist and writhe as a topological invariant 'linking number' (Calugareanu theorem) [6, 7]. The twist is simply the number of twisted turns in the filament (helical coiling turns in DNA). Writhe is defined by the curving of the filament centerline (or supercoiling in DNA). Specifically, writhe is the number of centerline crossovers averaged over all possible views of the filament. The linking number simply tells how many times one has to unwrap one strand in the DNA duplex around the other strand to completely separate the two strands. All three quantities (twist, writhe and linking number) can be positive or negative depending on whether they are right handed or left handed.

Tw = −2, Wr = 0

(a)

(b) Tw = 0, Wr = −2   (c) Tw = 0, Wr = −2
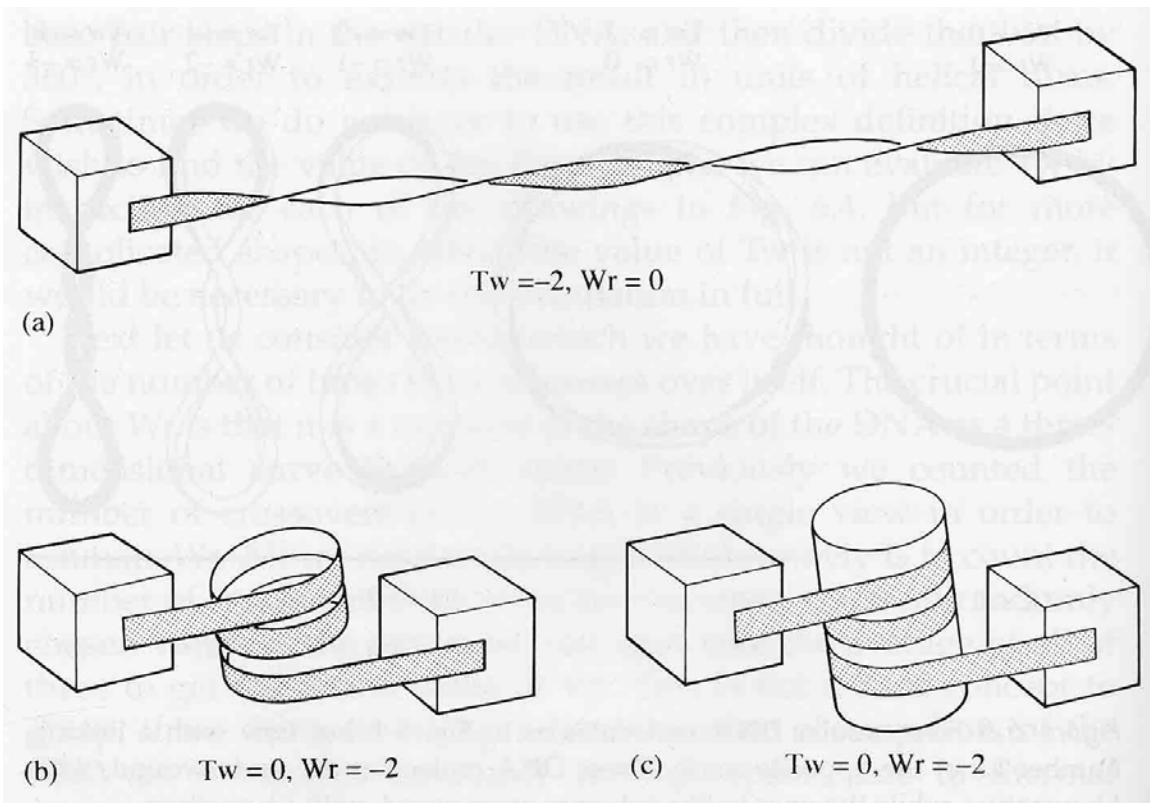
Figure A 1.4 The end blocks do not rotate and only translate towards each other. These end conditions conserve the linking number. Twist in the top strand converts to writhe. (Courtesy: Calladine et al. [5]).

To regulate the biological activity of DNA, there exist proteins that curve/twist DNA (repressors, TBP, zinc fingers, transcription factors) by docking or looping. In addition, there are other proteins ('topoisomerases') that change the linking number by nicking. The detailed structural mechanics involved in these processes is not well understood. However, there is increasing experimental evidence [8-11] that points to structural mechanics as playing a key role in the biological activity of DNA. Therefore structural modeling and simulation techniques for DNA are receiving increased research attention.

138

Appendix 2: Buckling Instability in DNA

A simply supported straight rod (homogeneous and isotropic) of length L_c becomes unstable and buckles into a helical shape under the action of axial torque and tension or compression when the following Greenhill's condition (described in Timoshenko and Gere [12]) is met:

$$M_t^2 - 4AP \geq \frac{4\pi^2 A^2}{L_c^2} \tag{A2.1}$$

Here, A is the bending stiffness and M_t and P are the torsional moment and tension at the boundaries. We can use Greenhill's condition as a rough guideline to estimate general instabilities under torsion/ compression. For example, we can estimate when a straight DNA strand that is 5% untwisted will achieve a torsional stress sufficient enough to render it unstable and initiate supercoiling. Consider the following table (Table A 2.1) that lists order of magnitude estimates of the structural parameters specific to DNA.

Table A 2.1 Estimates of structural parameters of DNA for instability condition (A2.1)

Quantity	Order of Magnitude (SI units)
Persistence lengths (torsional and bending)	10^{-7} m
Boltzmann constant	10^{-23} m^2 kg s^{-2} K^{-1}
Temperature	10^2 K
Stiffness[31] (torsional and bending)	10^{-28} m^3 kg s^{-2}
Intrinsic twist in DNA	10^9 rad/m^{-1}
5% untwist	10^8 rad/m^{-1}
Torsional moment[32] M_t	10^{-20} m^2 kg s^{-2}

---

[31] = Persistence length × Boltzmann constant × Temperature
[32] = Torsional stiffness × untwist

Substituting these into (A2.1) results in the inequality,

$$10^{-40} - 10^{-28} P \geq \frac{10^{-55}}{L_c^2}. \qquad (A2.2)$$

This inequality is satisfied for tensions as large as 10^{-12}N and lengths as small as 10^{-7}m (persistence length). In other words, it would require a tensile force on the order of piconewton to restrain a persistence length of 5% untwisted DNA from collapsing into a supercoiled state. Higher tensile forces would be needed for longer lengths of DNA.

Appendix 3: Physical Interactions Specific to DNA

Hydrodynamic Interactions

In beaded chain models of polymers, hydrodynamic interactions are included using the Rotne-Prager tensor [13]. The Rouse model [14] ignores the effects of hydrodynamic interactions while the Zimm model [15] accounts for them. The interactions through the fluid become strong when two or more segments fluctuate in close proximity. The overall significance of hydrodynamic interactions in DNA has been disputed as illustrated in the simulations of Hsieh et al. [16] and subsequently in the experiments of Shusterman et al. [17]. However, hydrodynamic interactions might also become prominent when there is a large bead attached to the polymer as frequently the case in single-molecule experiments done today. This is because the motion of a large bead strongly disturbs the surrounding fluid.

Thermal Kinetics

The strain energies in DNA are of the order of $K_b T$, where K_b = Boltzmann constant and T = absolute temperature of the aqueous medium. Thus, DNA mechanics are affected by the random bombardment of the surrounding fluid molecules. The thermal (or Langevin) forces exerted on DNA through these bombardments may be modeled (refer to Howard [18]) as random (white noise) external forces whose power spectrum is $4K_b T \xi_n$, where ξ_n = drag (normal) coefficient (Fluctuation-Dissipation Theorem). For proofs and more details refer to Appendix 4.3 in Howard [13].

Electrostatic Interactions

DNA is negatively charged due to phosphate ions in its backbone and hence moves towards an anode in electrophoresis. The ionic medium screens the electrostatic repulsion

as approximated by the nonlinear Poisson-Boltzmann (PB) equation[33] which can be solved for the potential with specified boundary conditions along the (deformed) DNA backbone. The solution of linearized PB equation yields the Debye-Huckel potential, which can be readily implemented in the structural mechanics models of DNA through configuration-dependent repulsive field forces. However the linear approximation might breakdown at very short distances from the charged backbone, especially in low electrolyte concentrations. At even shorter distances, the van der Waals attractive-repulsive potential becomes dominant due to charge fluctuations. The presence of multivalent ions or high concentrations of monovalent ions enhances the attractive potential at short distances. These transitions are captured approximately in DLVO (Derjaguin and Landau [19]; Verwey and Overbeek) theory (refer to Larson [20]) or more accurately in the Modified Poisson-Boltzmann (MPB)equation [21, 22] for DNA. Though the need to model the attractive potential is disputed by Rybenkov et al. [23, 24], its impact on DNA condensation in multivalent solutions has been simulated by Sottas et al. [25], perhaps without sufficient experimental justification so far. We will start with the simple Debye-Huckel screening model and, if needed, we will employ the approximate MPB in the future.

---

[33] Boltzmann distribution is valid in thermal equilibrium at high temperatures. At very low temperatures and at constant chemical potential, the Fermi-Thomas approximation is valid.

Appendix 4: Hydrodynamic Forces

Marine Cables

The hydrodynamics of underwater cables is dominated by fluid inertia (high Reynolds number) and is effectively modeled with standard Morison drag and added mass effects [26] for a cylindrical rod in the far-field flow v_f:

$$F_{drag} = \frac{1}{2}\rho_f D\{C_n |v_r \times a_3| a_3 \times (v_r \times a_3) + \pi C_t (v_r \cdot a_3)|v_r \cdot a_3| a_3\}, \qquad (A4.1)$$

$$F_{added\_mass} = -m_a\left\{\frac{\partial v}{\partial t} + \omega \times v\right\}. \qquad (A4.2)$$

Here $v_r = v_f - v$ is the flow relative to the rod, ρ_f is the fluid density, D is the rod diameter, C_n and C_t are the normal (form) drag and tangential (skin friction) drag coefficients respectively and m_a is the added mass coefficient. The rod's buoyant weight per unit length is

$$F_{buoyant\_weight} = \left(m - \rho_f \frac{\pi D^2}{4}\right)g, \qquad (A4.3)$$

where m is the rod's mass per unit length and the vector g is the acceleration due to gravity. The forces (per unit length) F_{drag}, F_{added_mass} and $F_{buoyant\_weight}$ are included in linear momentum equation (2.6) through the distributed force term F [34].

DNA Strands

The hydrodynamics of DNA is dominated by fluid viscosity (low Reynolds number) due to its small dimensions and can be modeled with the distributed drag forces and moments[35] on slender rods in Stokes flow (as described in Howard [18]):

$$F_{drag} = \left\{ \xi_n a_3 \times (v_r \times a_3) + \xi_t (v_r \cdot a_3) a_3 \right\},$$ (A4.4)

$$Q_{drag} = \left\{ \xi_{bending} a_3 \times (\omega_r \times a_3) + \xi_{torsional} (\omega_r \cdot a_3) a_3 \right\}$$ (A4.5)

where ξ_n and ξ_t are translational drag coefficients in the normal and tangential directions respectively, $\xi_{bending}$ and $\xi_{torsional}$ are rotational drag coefficients in the corresponding directions and ω_r is the fluid angular velocity relative to the rod. The drag coefficients can be determined approximately [27, 28] by Oseen's model of slow flow past a cylinder (refer to Lamb [29]). (But we must note that neglecting fluid inertia doesn't yield any solution to the Navier-Stokes flow past an infinite cylinder (Stokes' paradox). The overall drag for finite length cylinders is given in Howard [18] and includes end effects as suggested by Tirado and Garciadelatorre [27, 28]). But this description can not model the distributed drag. DNA is nearly neutrally buoyant in its aqueous surrounding and the influence of the inertia terms in the Newton-Euler Equations (2.6) and (2.7) is negligibly small.

---

[34] Since m_a is also a coefficient of a time derivative term, it has a contribution in the coefficient matrix M defined in Appendix 6.

[35] In the first approximation, we will ignore the moment. This is a fair approximation for slender rods with fine discretization.

Appendix 5: Constraint Equations

The *compatibility* constraint (2.9) in Chapter 2 follows from the continuity (in space and time) of the transformation L from the inertial frame $\{e_i\}$ to the body fixed frame $\{a_i\}$

$$\{e_i\} = \{a_i\}L .\tag{A5.1}$$

The ith column of L denoted by L_i represents the components of e_i in the body-fixed frame $\{a_i\}$. Now refer to Eq. (2.5) that relates the partial derivatives 'relative to' the two reference frames $\{e_i\}$ and $\{a_i\}$. According to Eq. (2.5), the time-derivative of each unit vector e_i 'relative to' the inertial frame $\{e_i\}$ leads to

$$\left(\frac{\partial}{\partial t}\right)_{\{e_i\}} e_i = \frac{\partial L_i}{\partial t} + \omega \times L_i$$

$$\text{But L.H.S.} = 0 \Rightarrow \frac{\partial L_i}{\partial t} = -\omega \times L_i \tag{A5.2}$$

Upon re-writing $\omega \times L_i = \widetilde{\omega}L_i$ ($\widetilde{\omega}$ is the skew-symmetric form of ω as defined in Appendix 7) for all columns of L, (A5.2) reduces to

$$\frac{\partial L}{\partial t} = -\widetilde{\omega}L .\tag{A5.3}$$

Similarly, differentiation of (A5.1) with respect to s leads to

$$\frac{\partial L}{\partial s} = -\widetilde{\kappa}L .$$

(A5.4)

Since the transformation L is continuous with respect to s and t (refer to Nikravesh [30]), the order of time and space derivatives is interchangeable, i.e.

$$\frac{\partial}{\partial s}\left(\frac{\partial L}{\partial t}\right) = \frac{\partial}{\partial t}\left(\frac{\partial L}{\partial s}\right),$$

(A5.5)

which upon repeated use of (A5.3) and (A5.4) leads to

$$\frac{\partial \widetilde{\omega}}{\partial s}L - \widetilde{\omega}\widetilde{\kappa}L = \frac{\partial \widetilde{\kappa}}{\partial t}L - \widetilde{\kappa}\widetilde{\omega}L .$$

(A5.6)

. Re-adjusting terms and post-multiplying by the transpose L^T leads to

$$\left(\frac{\partial \widetilde{\omega}}{\partial s} + \widetilde{\kappa}\widetilde{\omega} - \widetilde{\omega}\widetilde{\kappa}\right)LL^T = \frac{\partial \widetilde{\kappa}}{\partial t}LL^T .$$

(A5.7)

But L being orthogonal, $LL^T = \mathrm{I}$, where I is the identity matrix. Noting further that $\widetilde{\kappa}\widetilde{\omega} - \widetilde{\omega}\widetilde{\kappa}$ is the skew-symmetric form of $\kappa \times \omega$ leads to the *compatibility* constraint

$$\frac{\partial \omega}{\partial s} + \kappa \times \omega = \frac{\partial \kappa}{\partial t} .$$

(A5.8)

The constraint (2.8) in Chapter 2 follows from first computing the unit tangent vector $\hat{t}$. For an *inextensible* rod, the tangent to the centerline is given by

$$\left(\frac{\partial}{\partial s}\right)_{\{e_i\}} R = \hat{t} .$$

(A5.9)

Where $R(s,t)$ is the position vector. Due to continuity of $R(s,t)$ in s and t the order of time and space derivatives is interchangeable, i.e.

$$\left(\frac{\partial}{\partial t}\right)_{\{e_i\}}\left(\frac{\partial}{\partial s}\right)_{\{e_i\}}R=\left(\frac{\partial}{\partial s}\right)_{\{e_i\}}\left(\frac{\partial}{\partial t}\right)_{\{e_i\}}R. \tag{A5.10}$$

The right hand side (R.H.S.) of the above Eq. (A5.10) is

$$\text{R.H.S. of (A5.10)}=\left(\frac{\partial}{\partial s}\right)_{\{e_i\}}\left(\frac{\partial}{\partial t}\right)_{\{e_i\}}R=\left(\frac{\partial}{\partial s}\right)_{\{e_i\}}v=\frac{\partial v}{\partial s}+\kappa\times v. \tag{A5.11}$$

The left hand side (L.H.S.) of (A5.10) with substitution of (A5.9) becomes

$$\text{L.H.S. of (A5.10)}=\left(\frac{\partial}{\partial t}\right)_{\{e_i\}}\left(\frac{\partial}{\partial s}\right)_{\{e_i\}}R=\left(\frac{\partial}{\partial t}\right)_{\{e_i\}}\hat{t}=\frac{\partial\hat{t}}{\partial t}+\omega\times\hat{t}. \tag{A5.12}$$

Imposing the *unshearability* constraint $\dfrac{\partial\hat{t}}{\partial t}=0$, the L.H.S. of (A5.10) reduces to

$$\text{L.H.S. of (A5.10)}=\omega\times\hat{t}. \tag{A5.13}$$

Finally, equating the 'R.H.S. of (A5.10)' from (A5.11) to the 'L.H.S. of (A5.10)' from (A5.13) leads to the (*inextensibility* and *unshearability*) constraint (2.8)

$$\frac{\partial v}{\partial s}+\kappa\times v=\omega\times\hat{t}. \tag{A5.14}$$

Appendix 6: Coefficient Matrices

The coefficient matrices used in (2.10) in Chapter 2 may vary depending on the functional forms of the constitutive law $q(s,t) = fn(\kappa(s,t) - \kappa_0(s), s, ...)$, distributed force $F(s,t,...)$ and distributed moment $Q(s,t,...)$. We provide here the matrices for the case of linear elastic constitutive law $q(s,t) = B(s)(\kappa(s,t) - \kappa_0(s))$ and no dependence of $F(s,t,...)$ and $Q(s,t,...)$ on $\dfrac{\partial Y}{\partial t}$ or $\dfrac{\partial Y}{\partial s}$. Equation (2.10) consolidates the field equations in the following order: (2.8), (2.9), (2.7) and (2.6). The resulting coefficient matrix K is diagonal

$$K = -\begin{bmatrix} I & \Theta & \Theta & \Theta \\ \Theta & I & \Theta & \Theta \\ \Theta & \Theta & B & \Theta \\ \Theta & \Theta & \Theta & I \end{bmatrix} \text{ and } M = \begin{bmatrix} \Theta & \Theta & \Theta & \Theta \\ \Theta & \Theta & I & \Theta \\ \Theta & I & \Theta & \Theta \\ mI & \Theta & \Theta & \Theta \end{bmatrix}. \tag{A6.1}$$

Here Θ is the null matrix and I is the identity matrix. The matrix $\mathbb{F}$ captures the nonlinear terms and any distributed external forces/moments

$$\mathbb{F} = \left\{ \begin{array}{c} \omega \times \hat{t} - \kappa \times v \\ -\kappa \times \omega \\ -\left(\dfrac{\partial B}{\partial s} \kappa - \dfrac{\partial(B\kappa_0)}{\partial s} \right) + \omega \times I\omega + f \times \hat{t} - \kappa \times B(\kappa - \kappa_0) - Q \\ m(\omega \times v) - \kappa \times f - F \end{array} \right\}. \tag{A6.2}$$

Appendix 7: Skew-symmetric form of a vector

The cross product of two vectors x and y can be written as $x \times y = \tilde{x}y$, where

$$x = \begin{Bmatrix} x_1 \\ x_2 \\ x_3 \end{Bmatrix}, y = \begin{Bmatrix} y_1 \\ y_2 \\ y_3 \end{Bmatrix} \text{ and } \tilde{x} = \begin{bmatrix} 0 & -x_3 & x_2 \\ x_3 & 0 & -x_1 \\ -x_2 & x_1 & 0 \end{bmatrix}. \tag{A7.1}$$

If $|x|$ is the magnitude of x and u is the unit vector along x, then the exponential of the skew-symmetric matrix $\tilde{x}$ can be expressed as

$$\exp(\tilde{x}) = I + \tilde{u}\sin(|x|) + \tilde{u}^2(1 - \cos(|x|)), \tag{A7.2}$$

where I is the identity matrix. Note that this computation employs only a scalar power series and it therefore avoids the numerical difficulties of matrix exponentiation as identified by Moler and Vanloan [31].

Appendix 8: DNA Sequences and Boundary Conditions

(a) Wild-type LacR sequence [32]

```
     Operator O₃ at Location L1                    Operator O₁ at Location L2
       GGCAGTGAGCGCAACGCAATT  -    Wild-type DNA    -  AATTGTGAGCGGATAACAATT

              Fragment of inter-operator DNA modeled as rod (77 bp)
   ATTAATGTGAGTTAGCTCACTCATTAGGCACCCCAGGCTTTACACTTTATGCTTCCGGCTCGTATGTTGTGTGGAAT
```
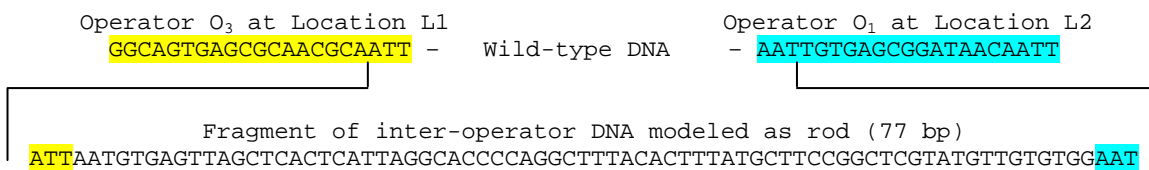
(b) Designed sequences [33] (personal communication with Prof. J. D. Kahn, Department of Chemistry and Biochemistry, University of Maryland)

```
                             Operator O_id
                          AATTGTGAGCGCTCACAATT


              L1                                                              L2
    T - O_id - AGATCTCAATTC - Linker - A tracts - Linker - TAGAATCGAAGCTAGCT - O_id
```

```
                                  11C12
         CTGTACGGATC - CGC(A)₆CGGGC(A)₆CGGC(A)₅{CGGGC(A)₆CGGC(A)₆}₂CGGGC(A)₆C -
                                 CGCTACGCGTCC

                                  9C14
      GTACGGATC - CGG(T)₆{GCCCG(T)₆GCCG(T)₆}₃GCCCG(T)₆G - CGCTGAACGCGTCC

                                  7C16
    ACGGATC - CGG(T)₆GCCCG(T)₆GCCG(T)₆{GCCG(T)₆GCCCG(T)₆}₂G - CGCTGACAACGCGTCC

                                 Control
   CTGTACGGATCCACTGAATCCGGTGAGAATGGCAAAAGCTTATGCATTTCTTTCCAGACTTGTTCAACAGGCCAG
                        CCATTACGCTCGTCATCAAAATCACTACGCGTCC
```

In arriving at the final looped state, the boundary base-pairs are made to align with their corresponding configurations known from the LacR crystal structure given by PDB ID: 1LBG [34,35], <http://www.pdb.org>. This alignment is achieved in our calculations by slowly translating and rotating the boundary base-pairs (rigid body motion) from the initial stress-free configuration to the final protein-bound configuration. As a

consequence, the inter-operator DNA deforms into a loop. Note that our boundary conditions account for the base-pair inclination with respect to the ds-DNA helical axis. We also verified that these boundary conditions are insensitive to the choice of boundary base-pairs within their immediate neighbors. To this end, we used commercial software NX Imageware (UGS, Plano, TX) to estimate the rigid body motion needed for the best alignment of the tri-nucleotide set of atoms around the chosen boundary base-pair (3 base-pairs highlighted in blue and red in Figure 7.1) and found it to be the same (within numerical tolerance) as that needed for the alignment of the chosen boundary base-pair. A sample computation from Imageware is shown in Figure A 8.1.

Input: **Output:**

Source
Point Cloud   **Imageware**   Rotation Tensor =
                                                               Rotate 127° about
                                                               {-0.11, 0.93, 0.36}

Rigid Body
Motion = ?   Translation Vector =
                                                               {-39.2, -54.5, 57.3} Å

Destination   RMS error = 1.41 Å
Point Cloud
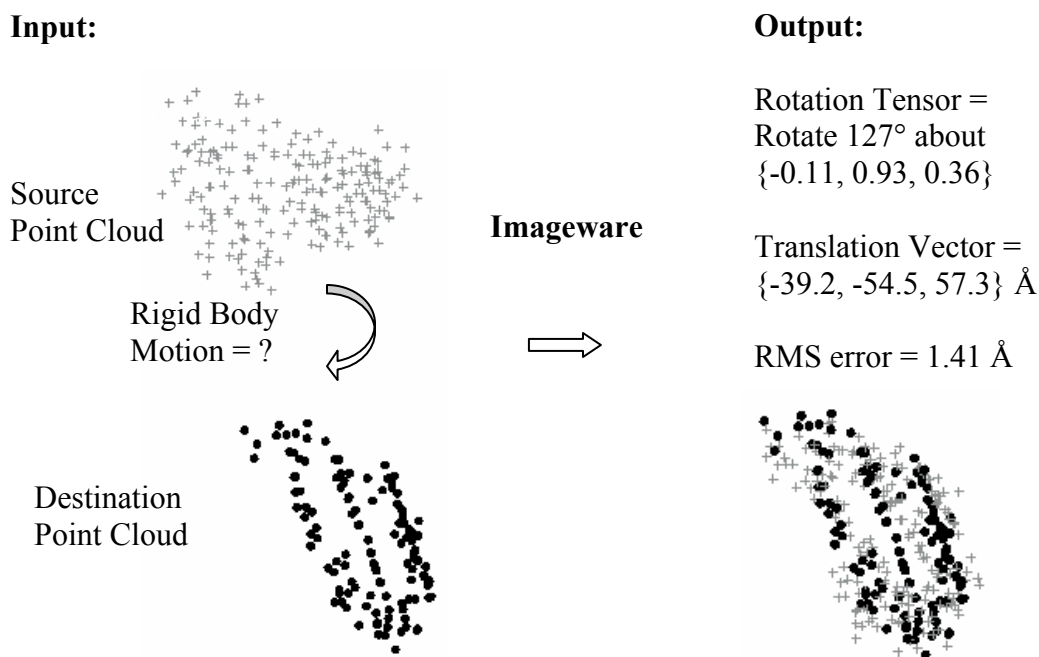
Figure A 8.1 A sample computation of rigid body motion (= translation + rotation) from Imageware. The source point cloud represents the atoms in the 3 base-pairs in stress-free DNA that are moved over to the corresponding atoms (represented by the destination point cloud) in the operator-protein crystal structure 1LBG.

Appendix 9: Modeling Sequence-dependent Intrinsic Curvature
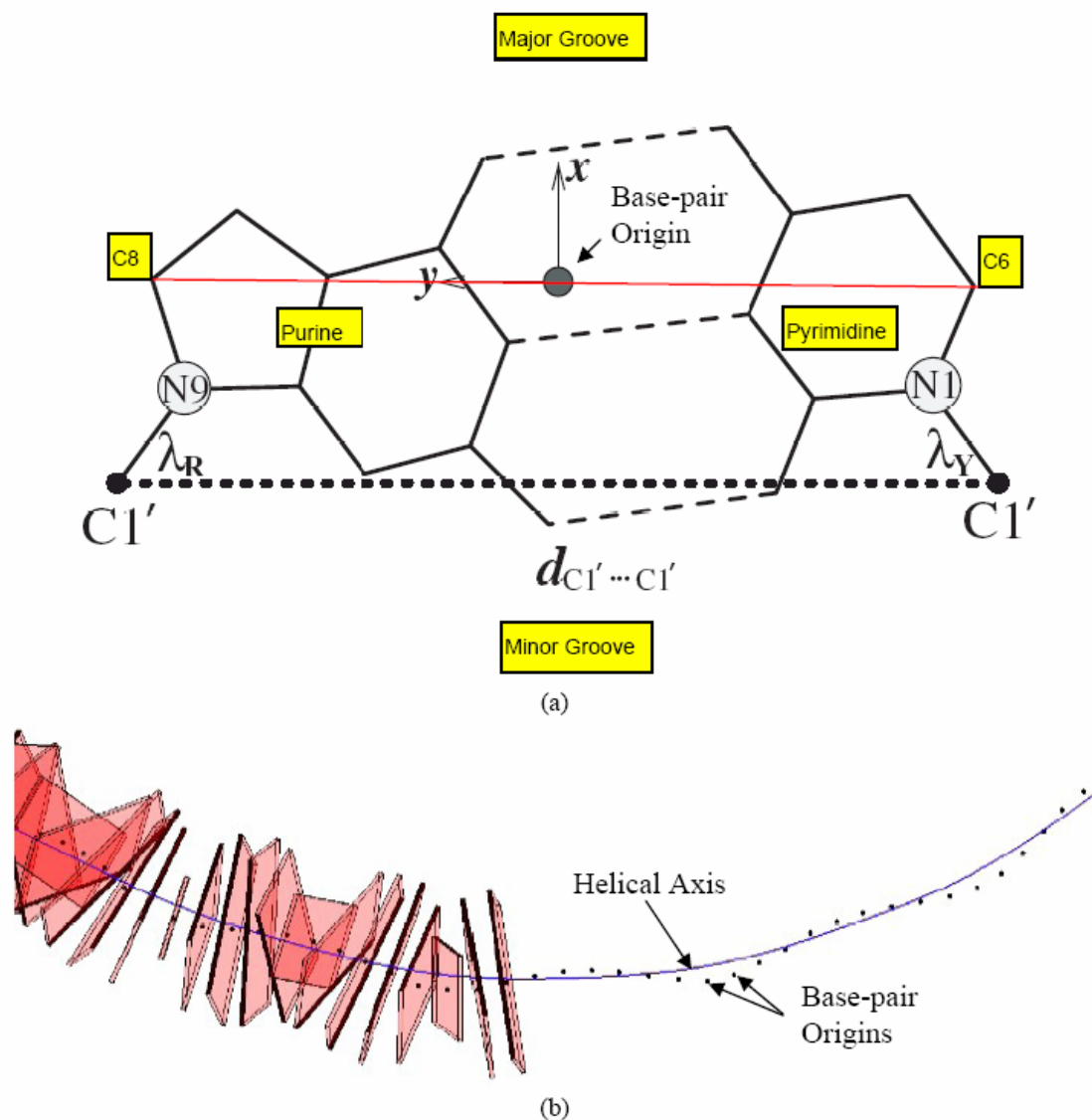
Figure A 9.1 The origin and standard base-pair fixed reference frame described in Olson et. al. [36]. (This figure is a modification of Fig. 1 from [36]). (b) Base-pairs represented as transparent red blocks with the minor-groove face shaded black. Black dots represent the base-pair origins, and the blue line represents the helical axis as computed by the moving average over a helical turn.

The following steps were used to compute the approximate helical axis $R_0(s)$ from the stress-free all-atom representation (PDB file) of the inter-operator DNA at zero temperature (consensus tri-nucleotide model [37]).

1. Following [36], we first compute the origin of each base-pair as the mid-point of the C6 atom of the pyrimidine and the C8 atom of the purine (see Figure A 9.1(a)). A curve interpolated through the base-pair origins forms an approximate helix of radius $r \approx 2.0 \,\text{Å}$ and helical pitch ≈ 10.3 base-pair (see Figure A 9.1(b)). The helical axis of this curve is not straight in general due to the intrinsic (stress-free) curvature of the molecule (see Figure A 9.1(b)).

2. An approximation to the helical axis $\widehat{R}_0(s)$ follows from averaging the positions of the origins of the base-pairs. We begin at one operator and then average the positions of the origins of the first ten base-pairs for the inter-operator DNA (see Figure A 9.1(b)). We then increment by one base-pair and repeat this (moving average) computation and continue to the other operator thereby developing a point-wise approximation to the helical axis $\widehat{R}_0(s)$.

3. A continuous (differentiable at least three times) curve $R_0(s)$ is sought to approximate $\widehat{R}_0(s)$ in order to compute the intrinsic curvature and torsion. We use the MATLAB curve-fitting toolbox (The MathWorks, Natick, MA) to construct a C^∞ continuous curve $R_0(s)$.

We emphasize that our computed results are insensitive to the specific approximations described in Steps 1-3 above. In particular, we have employed alternative curve fitting algorithms for Steps 1 and 3 and alternative moving averaging algorithms for Step 2. The resulting loop elastic energies typically differ by less than 2%.

References:

1.	Branden, C. and J. Tooze, *Introduction to Protein Structure*. 2 ed. 1999, New York: Garland Publishing.

2.	Lehninger, A.L., D.L. Nelson, and M.M. Cox, *Lehninger Principles of Biochenistry*. 4 ed. 2005, New York: W. H. Freeman.

3.	Watson, J.D. and F.H.C. Crick, *Genetical Implications of the Structure of Deoxyribonucleic Acid.* Nature, 1953. **171**(4361): p. 964-967.

4.	Watson, J.D. and F.H.C. Crick, *Molecular Structure of Nucleic Acids - a Structure for Deoxyribose Nucleic Acid.* Nature, 1953. **171**(4356): p. 737-738.

5.	Calladine, C.R., et al., *Understanding DNA, the Molecule and How It Works*. 3 ed. 2004, Amsterdam: Elsevier Academic Press.

6.	Fuller, F.B., *Writhing Number Of A Space Curve.* Proceedings Of The National Academy Of Sciences Of The United States Of America, 1971. **68**(4): p. 815-&.

7.	White, J.H., *Self-Linking And Gauss-Integral In Higher Dimensions.* American Journal Of Mathematics, 1969. **91**(3): p. 693-&.

8.	Finzi, L. and J. Gelles, *Measurement Of Lactose Repressor-Mediated Loop Formation And Breakdown In Single Dna-Molecules.* Science, 1995. **267**(5196): p. 378-380.

9.	Mehta, R.A. and J.D. Kahn, *Designed hyperstable lac repressor center dot DNA loop topologies suggest alternative loop geometries.* Journal Of Molecular Biology, 1999. **294**(1): p. 67-77.

10.	Smith, S.B., Y.J. Cui, and C. Bustamante, *Overstretching B-DNA: The elastic response of individual double-stranded and single-stranded DNA molecules.* Science, 1996. **271**(5250): p. 795-799.

11.	Yin, H., et al., *Transcription Against An Applied Force.* Science, 1995. **270**(5242): p. 1653-1657.

12.	Timoshenko, S.P. and J.M. Gere, *Theory of Elastic Stability*. 2 ed. 1961, New York: McGraw-Hill.

13.	Doi, M. and S.F. Edwards, *The theory of polymer dynamics*. The International series of monographs on physics ; 73. 1988, Oxford [Oxfordshire]

14.	Rouse, P.E., *A Theory Of The Linear Viscoelastic Properties Of Dilute Solutions Of Coiling Polymers.* Journal Of Chemical Physics, 1953. **21**(7): p. 1272-1280.

15.	Zimm, B.H., *Dynamics Of Polymer Molecules In Dilute Solution - Viscoelasticity, Flow Birefringence And Dielectric Loss.* Journal Of Chemical Physics, 1956. **24**(2): p. 269-278.

16.	Hsieh, C.C., L. Li, and R.G. Larson, *Modeling hydrodynamic interaction in Brownian dynamics: simulations of extensional flows of dilute solutions of DNA and polystyrene.* Journal Of Non-Newtonian Fluid Mechanics, 2003. **113**(2-3): p. 147-191.

17.	Shusterman, R., et al., *Monomer dynamics in double- and single-stranded DNA polymers*. Physical Review Letters, 2004. **92**(4).

18.	Howard, J., *Mechanics of Motor Proteins and the Cytoskeleton*. 2001, Sunderland: Sinauer Associates.

19. Derjaguin, B. and L. Landau, *Theory Of Stability Of Highly Charged Liophobic Sols And Adhesion Of Highly Charged Particles In Solutions Of Electrolytes.* Zhurnal Eksperimentalnoi I Teoreticheskoi Fiziki, 1945. **15**(11): p. 663-682.

20. Larson, R.G., *The Structure and Rheology of Complex Fluids.* 1999, New York: Oxford University Press.

21. Bhuiyan, L.B. and C.W. Outhwaite, *The Cylindrical Electric Double-Layer In The Modified Poisson-Boltzmann Theory.* Philosophical Magazine B-Physics Of Condensed Matter Statistical Mechanics Electronic Optical And Magnetic Properties, 1994. **69**(5): p. 1051-1058.

22. Gavryushov, S. and P. Zielenkiewicz, *Electrostatic potential of B-DNA: Effect of interionic correlations.* Biophysical Journal, 1998. **75**(6): p. 2732-2742.

23. Rybenkov, V.V., A.V. Vologodskii, and N.R. Cozzarelli, *The effect of ionic conditions on the conformations of supercoiled DNA .1. Sedimentation analysis.* Journal Of Molecular Biology, 1997. **267**(2): p. 299-311.

24. Rybenkov, V.V., A.V. Vologodskii, and N.R. Cozzarelli, *The effect of ionic conditions on the conformations of supercoiled DNA .2. Equilibrium catenation.* Journal Of Molecular Biology, 1997. **267**(2): p. 312-323.

25. Sottas, P.E., et al., *Brownian dynamics simulation of DNA condensation.* Biophysical Journal, 1999. **77**(4): p. 1858-1870.

26. Morison, J.R., et al., *The Force Exerted By Surface Waves On Piles.* Transactions Of The American Institute Of Mining And Metallurgical Engineers, 1950. **189**: p. 149-154.

27. Tirado, M.M. and J. Garciadelatorre, *Translational Friction Coefficients Of Rigid, Symmetric Top Macromolecules - Application To Circular-Cylinders.* Journal Of Chemical Physics, 1979. **71**(6): p. 2581-2587.

28. Tirado, M.M. and J. Garciadelatorre, *Rotational-Dynamics Of Rigid, Symmetric Top Macromolecules - Application To Circular-Cylinders.* Journal Of Chemical Physics, 1980. **73**(4): p. 1986-1993.

29. Lamb, H., *Hydrodynamics.* 6 ed. 1945, New York: Dover Publications.

30. Nikravesh, P.E., *Computer-aided Analysis of Mechanical Systems.* 1988, Englewood cliffs: Prentice-Hall.

31. Moler, C. and C. Vanloan, *19 Dubious Ways To Compute Exponential Of A Matrix.* Siam Review, 1978. **20**(4): p. 801-836.

32. Dickson, R.C., et al., *Genetic-Regulation - Lac Control Region.* Science, 1975. **187**(4171): p. 27-35.

33. Mehta, R.A. and J.D. Kahn, *Designed hyperstable lac repressor center dot DNA loop topologies suggest alternative loop geometries.* Journal Of Molecular Biology, 1999. **294**(1): p. 67-77.

34. Lewis, M., et al., *Crystal structure of the lactose operon repressor and its complexes with DNA and inducer.* Science, 1996. **271**(5253): p. 1247-1254.

35. Berman, H.M., et al., *The Protein Data Bank.* Nucleic Acids Research, 2000. **28**(1): p. 235-242.

36. Olson, W.K., et al., *A standard reference frame for the description of nucleic acid base-pair geometry.* Journal of Molecular Biology, 2001. **313**(1): p. 229-237.

37.   Gabrielian, A. and S. Pongor, *Correlation of intrinsic DNA curvature with DNA property periodicity.* Febs Letters, 1996. **393**(1): p. 65-68.